Yong Yan

Plasma-assisted synthesis of hydrogenated TiO_2 for energy storage and conversion

Werkstofftechnik Aktuell

Schriftenreihe aus dem Fakultätsübergreifenden Institut für Werkstofftechnik (IWT) an der TU Ilmenau

Herausgegeben von

Univ.-Prof. Dr. rer. nat. Dr. h. c. Peter Schaaf

und Univ.-Prof. Dr.-Ing. Edda Rädlein

Band 14

Die vorliegende Schriftenreihe "Werkstofftechnik Aktuell" berichtet über aktuelle Forschungsergebnisse aus dem Institut für Werkstofftechnik (IWT) der TU Ilmenau. Die ausgewählten Texte spiegeln die breit gefächerten materialwissenschaftlichen und werkstofftechnischen Themen, die am IWT bearbeitet werden, wieder. Für weitere Informationen und Rückfragen können Sie sich gerne an das Institut (www.tu-ilmenau.de/wt) wenden oder das Institut persönlich besuchen. Über Ihre Anregungen, konstruktive Kritik und Ihre Kontaktaufnahme würden wir uns sehr freuen. Das IWT steht wissenschaftlichen Zusammenarbeiten stets aufgeschlossen gegenüber.

Plasma-assisted synthesis of hydrogenated TiO_2 for energy storage and conversion

Yong Yan

Universitätsverlag Ilmenau
2015

Impressum

Bibliografische Information der Deutschen Nationalbibliothek

Die Deutsche Nationalbibliothek verzeichnet diese Publikation in der Deutschen Nationalbibliografie; detaillierte bibliografische Angaben sind im Internet über http://dnb.d-nb.de abrufbar.

Diese Arbeit hat der Fakultät für Elektrotechnik und Informationstechnik der Technischen Universität Ilmenau als Dissertation vorgelegen.

Tag der Einreichung:	9. März 2015
1. Gutachter:	Univ.-Prof. Dr. rer. nat. habil. Dr. h. c. Peter Schaaf (Technische Universität Ilmenau)
2. Gutachter:	Univ.-Prof. Dr. rer. nat. habil. Dr. h. c. Andreas Bund (Technische Universität Ilmenau)
3. Gutachter:	Prof. Dr.-Ing. Ge Chen (Beijing University of Technology)
Tag der Verteidigung:	16. Juli 2015

Technische Universität Ilmenau/Universitätsbibliothek
Universitätsverlag Ilmenau
Postfach 10 05 65
98684 Ilmenau
www.tu-ilmenau.de/universitaetsverlag

Herstellung und Auslieferung
Verlagshaus Monsenstein und Vannerdat OHG
Am Hawerkamp 31
48155 Münster
www.mv-verlag.de

ISSN 1868-6532 (Druckausgabe)
ISBN 978-3-86360-125-6 (Druckausgabe)
URN urn:nbn:de:gbv:ilm1-2015000348

Abstract

Titanium dioxide (TiO_2) has been widely used in energy storage and conversion area. However, the performance of TiO_2 is substantially lower than practically required as a result of its limited solar absorption, charge transfer rate, and electrochemical acitivity. In this study, hydrogenated TiO_2 (H-TiO_2) with distinct physical and chemical properties are controlledly synthesized through a hydrogen (H_2) plasma treatment, which exhibit excellent performance in application for lithium ion batteries, photocatalysis, and photothermal conversion. Moreover, the microstructure of H-TiO_2, and their effect on the application performance of H-TiO_2 are comprehensively investigated. It is believed that this research might provide new insights into synthesis, properties, and applications of H-TiO_2, which is highly favorable for the development of high-performance and versatile TiO_2 materials for energy storage and conversion devices.

Firstly, hydrogenated anatase TiO_2 nanoparticles with significantly improved fast lithlium storage performance are synthesized through a high-temperature H_2 plasma treatment. Systematic electrochemical analysis revealed that the improved rate capability of H-TiO_2 results from the enhanced contribution of pseudocapacitive lithium storage on the particle surface. It is suggested that the disordered surface layers and presence of Ti^{3+} species of H-TiO_2 play an important role in the improvement of pseudocapacitive lithium storage.

Secondly, H-TiO_2 with different hydrogenation degrees are rapidly synthesized through high-power H_2 plasma treatment in several minutes; and their photocatalytic activity is evaluated by methylene blue (MB) degradation and CO_2 reduction in aqueous and gaseous media, respectively. The slightly hydrogenated TiO_2 (s-H-TiO_2) with the original white color exhibit enhanced photoactivity compared with the pristine TiO_2; while the grey or black H-TiO_2 with higher hydrogenation degrees (h-H-TiO_2) display much worse catalytic performances. Further investigations reveal that the higher ratio of trapped holes (O^- centers) and lower recombination rates

induced by the increasing of surface defects might be the critical factors for the high activity of s-H-TiO_2; on the contrary, h-H-TiO_2 possess high concentrations of bulk defects, leading to the significantly decreased amount of O^- centers and enhanced non-radiative recombination, which strongly inhibit their photoactivity.

Thirdly, hydrogenated black TiO_2 with large infrared absorption is explored as photothermal agent for cancer photothermal therapy due to its dramatically enhanced non-radiative recombination. To improve the suspension stability, the H-TiO_2 nanoparticles were coated with polyethylene glycol (PEG). After PEG coating, H-TiO_2-PEG exhibite high photothermal conversion efficiency of 40.8%, and stable size distribution in serum solution. The therapy effect of H-TiO_2-PEG demonstrates that this material is of low toxicity, and can effectively kill MCF07, 4T1 tumor cells (transplantable tumor cells from human breast cancer) under infrared irradiatation.

In addition, Si/N-doped TiO_2 core/shell nanopillar arrays with a nanoporous structure are fabricated through a simple protein-mediated TiO_2 deposition process, which can be considered as the advance reseach for prepration of H-TiO_2 on sensitive templates with ultrafine nanostructure.

Zusammenfassung

Titandioxid (TiO_2) wird bereits häufig in den Bereichen Energiespeicherung und -umwandlung eingesetzt. Aufgrund der begrenzten Solarabsorption, Ladungsübertragungsgeschwindigkeit und elektrochemischer Aktivität ist die Leistung des TiO_2 allerdings wesentlich niedriger als es für die praktische Anwending erforderlich ist. In dieser Studie wird hydriertes TiO_2 (H-TiO_2) mit unterschiedlichen physikalischen und chemischen Eigenschaften durch Wasserstoff (H_2)-Plasmabehandlung kontrolliert hergestellt, welches hervorragende Leistungen in der Anwendung von Lithium-Ionen-Batterien, Fotokatalyse und fotothermischer Umwandlung aufweist. Darüber hinaus werden die Mikrostrukturen des H-TiO_2 und die Abhängigkeit der Anwendungsleistung des H-TiO_2 von den Vorliegenden Mikrostrukturen umfassend untersucht. Diese Studie bietet neue Erkenntnisse über Synthese, Eigenschaften und Anwendungen von H-TiO_2, durch welche die Entwicklung leistungsfähiger und vielseitiger TiO_2-Materialien für die Energiespeicherung und -umwandlung ermöglicht werden kann.

Erstens werden hydrierte Anatas TiO_2-Nanopartikel mit deutlich verbesserter Speicherleistung von Lithium-Ionen durch eine Hochtemperatur (390 °C) H_2-Plasmabehandlung in hergestellt. Die systematische elektrochemische Analyse zeigt, dass sich aus dem verbesserten Beitrag der pseudokapazitiven Lithium-Speicherung auf der Partikeloberfläche eine verbesserte Leistungsdichte von H-TiO_2 ergibt. Es wird gezeigt, dass die ungeordneten Oberflächenschichten und die Vorliegenden Ti^{3+}-Spezies von H-TiO_2 eine wichtige Rolle bei der Verbesserung der pseudokapazitiven Lithiumspeicherung spielen.

Zweitens erfolgt eine schnelle Synthese des H-TiO_2 mit unterschiedlichem Hydrierungsgrad durch Hochleistungs-H_2-Plasmabehandlung. Dessen fotokatalytische Aktivitäten werden mit Hilfe von Methylenblau (MB)-Degradation und CO_2-Reduktion in wässrigen und gasförmigen Medien ausgewertet. Im Vergleich zum ursprünglichen TiO_2 zeigt das leicht

hydrierte TiO_2 (s-H-TiO_2) eine weiße Färbung und eine verbesserte Fotoaktivität, während das graue oder schwarze H-TiO_2 mit höherem Hydrierungsgrad (h-H-TiO_2) eine viel schlechtere katalytische Leistung aufweist. Wie weitere Untersuchungen gezeigt haben, stellen das höhere Verhältnis der gefangenen Löcher (O^--Zentren) und die niedrige Rekombinationsrate, welche durch die Erhöhung der Oberflächendefekte verursacht sind, die kritischen Faktoren für die hohe Aktivität von s-H-TiO_2 dar. Im Gegensatz dazu besitzt das h-H-TiO_2 eine hohe Konzentration an Gitterdefekten, was zu einer signifikant verringerten Menge an O-Zentren und der vergrößerten strahlungslosen Rekombination führt. Dadurch sinkt die Fotokatalyseaktivität deutlich.

Drittens wird das hydrierte schwarze TiO_2 mit großer Infrarotabsorption (aufgrund seiner erheblich vergrößerten, strahlungslosen Rekombination) für die fotothermische Tumortherapie untersucht. Um die Stabilität der Suspension zu verbessern, wurden die H-TiO_2-Nanopartikel (NPs) mit Polyethylenglycol (PEG) beschichtet. Nach PEG-Beschichtung zeigen die H-TiO_2 NPs einen erhöhten fotothermischen Umwandlungswirkungsgrad von 40,8% und eine gute Suspensionsstabilität im Serum. Der Therapieeffekt von H-TiO_2-PEG NPs zeigt, dass dieses Material eine geringe Toxizität besitzt und MCF07- sowie 4T1-Tumorzellen (transplantierbaren Tumorzellen des menschlichen Brustgewebes) unter Infrarotstrahlung effektiv abtöten kann.

Zusätzlich werden Si (*core*) / N-dotiertes TiO_2 (*shell*) *Nanopillar-Arrays* mit einer nanoporösen Struktur durch ein einfaches, proteinvermittelndes TiO_2-Abscheidungsverfahren hergestellt. Dieses Ergebnis kann als ein fortschrittlicher Ansatz für die großtechnische Herstellung der H-TiO_2 basierten Nanokompositen angesehen werden.

Acknowledgements

This work was carried out from September 2012 to June 2015 under the guidance of Prof. Dr. Peter Schaaf at the Institute of Materials Engineering and the Institute of Micro- and Nanotechnologies MarcoNano®, Chair Materials for Electronics, at TU Ilmenau.

First of all, I would like to express my appreciation to Prof. Dr. Peter Schaaf for giving me the opportunity to persue my Ph.D. in his group and for his guidance in my research work. I am also very grateful to Dr. Dong Wang for his support and help in my experiments. Besides, I want to express my highly gratitude to Prof. Dr. Ge Chen from Beijing University of Technology for his great contribution in this work. Thank for the helping from Prof. Aiguo Wu in bioapplications.

Additionally, I am grateful to Dr. Arne Albrecht, Mrs. Birgitt Hartmann, Mrs. Manuela Breiter, Mr. Joachim Döll, Mr. Eric Markweg, Mr. Tobias Remdt, and Mr. Stefan Hanitsch from ZMN for their help with sample preparation, and Dr. Thomas Kups, Mr. Andreas Herz, Mr. Marcus Hopfeld, Mr. Rolf Grieseler, Mr. Jens Schawohl, Dr. Patrick D. Nsimama, and Mrs. Magali Camargo for their help with sample characterization. I also acknowledge Dr. Herbert Tippmann, Mrs. Antje Schencke, Mrs. Elvira Remdt, and Ms. Diana Roßberg for their assistance with my experiments.

Many thanks for the support of doctoral scholarship from the Carl Zeiss Stiftung, and this work was supported by the state of Thuringia (Germany) and by the European Funds for Regional Development (NanoBatt TNA VII-1/2012), National Natural Science Foundation of China (NSFC 11475012).

Also, many thanks to Mr. Ruijia Tang, Mr. Song Du, Mr. Qiong Wu, Mr. Mingqiang Wu, Mrs. Xueyang Yang, Mrs. Yan Mi, and Mr. Liaoyong Wen for their countless help in the past three years. Thanks a lot for your friendship and I really treasure those good memories of being with you.

Finally, I would like to thank my family for their consistent love and support.

Contents

List of Figures

1. Introduction

With the current threat of the exhaustion of fossil fuels and the continuing deterioration of the global environment, the development of high-efficient, low-cost, and environmental friendly energy storage and conversion technologies (such as lithium ion batteries, solar-driven catalysis, and photothermal heating etc.) have attracted much attention [1-3]. In principle, fabrication of high-performance functional materials for these applications is a major challenge [4].

Due to the advantages of low-cost, nontoxic, electrochemical stability, favarable band-edge position, etc., titanium dioxide (TiO_2) and its related composites have been widely used in environmental and energy areas ranging from photocatalysis and solar cells to sensors and batteries [5-7]. However, the performance of TiO_2 is substantially lower than practically required as a result of its limited solar absorption (large bandgap, >3.0 eV), fast electron-hole pair recombination, and poor electrochemical acitivity and electric conductivity [8]. Hence, many efforts has been devoted to overcome these intrinsic limitations of TiO_2: for narrowing the bandgap of TiO_2, doping metal or nonmetal elements, heterojunctions with low bandgap semiconductors, sensitization by organic dyes are considered as effective routes, which could increase its solar absorption coefficient and wavelength range (from UV to visible light) [9-11]; fabrication of specific morphologies and decoration with noble metal nanoparticles are promising pathways to enhance the separation and transportation of electrons and holes in TiO_2 [12, 13]; introducing defects, controlling the exposed facet, and compositing with conductive agents aim to enhance the electrochemical acitivity and electric conductivity of TiO_2 [14-16]. Nevertheless, designing a simple and versatile method to overcome these problems of TiO_2 simultaneously still remains a challenge task.

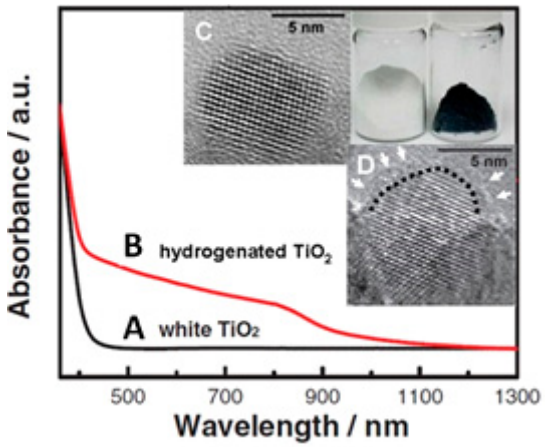

Figure 1-1. UV−vis spectra of pure white (A) and hydrogenated black TiO_2 (B). (Insets) Photo and HRTEM images of common white TiO_2 (C) and hydrogenated black TiO_2 nanocrystals (D) [17]. (Reprinted from Ref [17])

In 2011, Chen and co-workers reported a novel hydrogneation treatment approach to generate hydrogenated TiO_2 nanocrystals (H-TiO_2) with significantly improved optical absorption in the visible and near infrared light region (black color). Moreover, H-TiO_2 possesses a disordered surface layer and increased surface functional groups, and shows superior photocatalytic activity compared with normal white TiO_2 (Figure 1-1) [17]. Since then, many strategies were developed to synthesize H-TiO_2, which included anealing in H_2, aluminium reduction, elelctrochemical reduction, and hydrothermal processes [18-21]. Therefore, black-TiO_2 with distinct physical and chemical properties was obtained through these different methods, and the application of H-TiO_2 were also extended to supercapacitors, lithium ion batteries, fuel cells, field emmision, microwave absorption, etc [19, 20, 22-24].

Despite these achievements, several problems need to be addressed for the further practical application of H-TiO_2 in energy storage and conversion devices: firstly, the hydrogenation processes often require harsh conditions or complex processes, including long reaction times, high-pressures of H_2, rapid cooling, or specially designed precusors, which make it unsuitable for practical production [18-24]; secondly, tuning the microstructure of H-TiO_2 in the synthetic process is not easy to achieve in the current stage; thirdly, the

understanding of the dependence of H-TiO_2 application performance on their sturctural properties is limited.

In this study, H-TiO_2 are controlledly synthesized through hydrogen (H_2) plasma treatment (by varying the power and density of plasma, reaction time, and temperature), which exhibit excellent performance in the application for lithium ion batteries, photocatalysis, and photothermal conversion. Moreover, the sturctural properties of H-TiO_2, and their dependence on the application performance of H-TiO_2 are comprehensively investigated. It is believed that the obtained results might provide new insights into synthesis, properties, and applications of H-TiO_2, which is highly favorable for the development of high-performance TiO_2 materials.

2. Experiments and Methods

2.1 Synthesis of black anatase H-TiO_2 nanoparticles for lithium storage

Materials and synthesis: Anatase TiO_2 nanoparticles with a mean diameter of 15 nm and specific surface area of 178 $m^2 \cdot g^{-1}$ were purchased from Alfa Aesar Co. and used without purification. 0.10 g anatase TiO_2 nanoparticles were dispersed in 50 mL ethanol under an ultrasonic condition and drop-casted onto a 6-inch Si wafer. The drop casting process was repeated several times to achieve a TiO_2 mass loading of 0.5~0.6 mg/cm^2 (TiO_2 mass loading should be less than 1.5 mg/cm^2 to avoid TiO_2 nanoparticles shedding from the surface of Si wafer in hydrogenation process). Then, this whole wafer was transferred into a chamber for plasma-enhanced hydrogenation treatment, and there an instrument of inductively coupled plasma (Plasmalab 100 ICP-CVD, Oxford Instruments) was used. The H_2 plasma treatment was performed at 390 °C for 180 min, the ICP power was 3000 W, the chamber pressure was 26.5~28.3 mTorr, and the H_2 flow rate was 50 sccm. In this process, the surface of anatase TiO_2 nanoparticles was partially reduced. After this treatment, H-TiO_2 was obtained and scratched from Si wafer for further investigations. For comparison, another prepared sample was annealed at 390 °C in H_2 (with the same pressure and flow rate but without plasma) for 180 min in the same chamber.

Electrochemical measurement: The N-methyl pyrrolidinone (NMP) slurry composed by H-TiO_2, carbon black, and polyvinylidene fluoride (with the contents of 70, 15, 15 wt%, respectively) was obtained under ultrasonication. Then, this slurry was dropped onto pure Cu foil with an active material loading of 1.5 ~ 1.7 mg/cm^2, and was dried in vacuum oven for 12 h at 100 °C. Glass fiber (GF/D, Whatman) was used as a separator; pure lithium foil (Aldrich) was used as the counter electrode; and 1 M $LiPF_6$ in a 50 : 50 w/w mixture of ethylene carbonate and diethyl carbonate was used as the electrolyte. The coin cell assembly was finished in argon glove box with the

moisture and oxygen contents below 1 ppm. Galvanostatic electrochemical experiments were carried out with a Neware Battery Tester (Shenzhen, China). Cyclic voltammetry (CV) analysis were measured over a potential range of 3.0 to 1.0 V at various scan rate of 0.1, 0.2, 0.5, 1.0, and 2.0 $mV \cdot s^{-1}$ on a potentiostat (VMP3).

2.2 Synthesis of P25 H-TiO_2 nanoparticles with different hydrogenation degrees for photocatalysis

Materials and synthesis: Degussa P25 were purchased from Sigma-Aldrich Co. and used as precursor without purification. 0.10 g TiO_2 nanoparticles were dispersed and drop-casted onto a Si wafer as mentioned above. The H_2 plasma treatment was performed at 150 °C for 30 s, 1 min, 3 min, 5 min, 20 min for the synthesis of H-TiO_2-30s, H-TiO_2-1min, H-TiO_2-3min, H-TiO_2-5min, and H-TiO_2-20min, respectively. The ICP power was 3000 W, the chamber pressure was 25.8~27.1 mTorr, and the H_2 flow rate was 50 sccm.

Photocatalytic methylene blue (MB) degradation: the photocatalytic activities of the samples in aqueous media were tested by investigating degradation of methylene blue (MB) at room temperature. The each sample containing 10 mg of TiO_2 was suspended in 40 mL MB solution (0.03 mM), and the suspension was placed into a closed container. In each experiment, the container was kept in the dark for 0.5 h to achieve adsorption and desorption equilibra with stirring. About 9.1%, 7.7%, 7.4%, 8.3%, 7.1%, and 5.4% of MB was adsorbed by pristine-TiO_2, H-TiO_2-30s, -1min, -3min, -5min, and -20min, respectively. Subsequently, solution were irradiated using 300 W Xe-lamp (full-spectrum, PLS-SXE300CUV, Perfect light, China), and at given time intervals (every 2 min), 2 mL of the suspension was collected and centrifuged (12000 r/min for 20 min) to obtain the clarify solution of dye. Then, the residual concentration of MB was measured by UV-vis absorption analysis. The peak absorbance of MB (at 666 nm) was used to determine its concentration. In the control experiment without TiO_2 catalyst, less than 5% of MB was degradated under full-spectrum irradiation for 30 min.

Photocatalytic CO_2 reduction: The photocatalytic activities of the samples in gaseous media were tested by investigating CO_2 reduction at room temperature. Each sample (90 mg) was dispersed in water and deposited over three glass substrates (conventional glass slides used for optical microscopy). The total area covered is around 60 cm^2. Evaporated at room temperature overnight, and further dried at 100 °C. Then, the samples were introduced in a stainless steel reactor with an internal volume of around 200 mL, provided with an optical window made of Borofloat 33 glass. The chamber was purged during 1 h with humid CO_2 (CO_2 bubbled though water) at a flux of 200 mL/min. Then, the valves were closed, and it was illuminated during 3h. The radiation source was a 550 W Xe-lamp with a AM 1.5G filter (solar simulator ABET Technologies, SUN2000) with a uniform illuminated area of 10×10 cm^2, providing 100 mW cm^{-2} in the work plane measured with a thermopile detector. After this time, the amount of CO and CH_4 evolved were quantified by a MicroGC, with two consecutives analyses.

2.3 Synthesis of black P25 H-TiO_2 nanoparticles for cancer photothermal therapy

Materials and synthesis: Degussa P25 were treated by the H_2 plasma at 300 °C for 20 min. The ICP power was 3000 W, the chamber pressure was 25.8~27.1 mTorr, and the H_2 flow rate was 50 sccm.

PEG coating and photothermal conversion efficiency of H-TiO_2-PEG NPs: For biomedical applications, the H-TiO_2 should be disperse and stable in serum. In this study, polyethylene glycol (PEG, molecular weight 1500) was used to enwrap the H-TiO_2 NPs to improve their stability. 20 mg of H-TiO_2 powder was dispersed in 75 mL ethanol by an ultrasound treatment of 30 min. The H-TiO_2 contained ethanol was dropped into a 25 mL PEG-ethanol solution (20 mg·mL^{-1} of PEG), and stirred for 24 h. H-TiO_2-PEG NPs were separated by centrifugation, and were washed with ultrapure water. The as-prepared H-TiO_2-PEG NPs were dispersed in the ultrapure water and stored at 4 °C. Micro-morphologies of H-TiO_2 before and after PEG coating were investigated through a transmission electron microscope (FEI Tecnai F20). Size distribution and zeta potential of H-TiO_2

and H-TiO_2-PEG were measured by a particle size-zeta potential analyzer (Nano ZS, Malvern Instruments Ltd, England). The UV-Visible spectra of H-TiO_2 and H-TiO_2-PEG were determined by using an UV-visible spectrophotometer (T10CS, Beijing Purkinje General Instrument, China).

For evaluating the photothermal conversion efficiency of H-TiO_2-PEG, 2 mL aqueous dispersion of H-TiO_2-PEG (100 $\mu g \cdot mL^{-1}$) were moved into a well of 24-well culture plate, and irradiated under an 808 nm NIR laser at a power density of 2 $W \cdot cm^{-2}$ for 600 s. The temperature of the dispersion was measured every 60 s after the start of irradiation. After the laser irradiation was shut off, the temperature was further measured for another 1500 s with the same intervals. Ultrapure water as control group was treated under the same conditions. Photothermal conversion efficiency (η) of H-TiO_2-PEG was then calculated according to the method reported previously [25].

In order to investigate the stability, H-TiO_2-PEG NPs were dispersed in fetal bovine serum solution for 7 days, and size distributions of the nanoparticles were measured every day by the particle size-zeta potential analyzer.

Cell culture and cytotoxicity of H-TiO_2-PEG NPs *in vitro*: MCF-7 cell line of human breast cancer and 4T1 cell line of murine breast cancer were cultured in RPMI1640 medium and supplemented with 10% fetal bovine serum (FBS). The cells were maintained at 37 °C incubator with 5% CO_2.

To evaluate the cytotoxicity of H-TiO_2-PEG, MCF-7 or 4T1 cells were plated in 96-well plates (1×10^4 cells per well) and cultured for 24 h. The cells were incubated with different doses of H-TiO_2-PEG for 24 h. The viability of cells was assayed by the MTT assay. Briefly, 10 μL of MTT (5 $mg \cdot mL^{-1}$ in PBS) was added into every well, and incubated for 4 h. Next, DMSO was used to dissolve the formazan crystals. The absorbance was measured by a Microplate Absorbance Reader (Biorad iMARK™, USA), and the cell viability was calculated.

Intracellular localization of H-TiO_2-PEG NPs: To investigate the distribution of H-TiO_2-PEG in the cancer cells, fluorescent dye alizarin red S (ARS) was used to stain TiO_2 as previously reported [26]. MCF-7 and 4T1 cells (2×10^5 cells) were seeded into 35 mm culture dishes and cultured for 24h, respectively. The culture media was then replaced by fresh medium

contained ARS or ARS-H-TiO_2-PEG. The cells were incubated for 2 hours, then washed with PBS, and fixed with 4% formaldehyde. Then they were incubated with 0.2% Triton X-100 and 1% BSA to block the nonspecific binding sites and stained with FITC- phalloidine and Hoechst 33342. The intracellular localization of H-TiO_2-PEG was observed through confocal microscopy (TCS SP5, Leica Microsystems, Germany).

Photothermal therapy of H-TiO_2-PEG NPs *in vitro*: To quantitatively evaluate the photothermal therapy efficiency of H-TiO_2-PEG on cancer cells, MCF-7 and 4T1 cells were seeded into 96-well plates (1×10^4 cells per well), respectively. The cells were then incubated with fresh DMEM and 100 $\mu g\cdot mL^{-1}$ of H-TiO_2-PEG containing DMEM for 2 h. After 2 h incubation, all of the media were replaced by fresh DMEM. The cells were then irradiated by an 808 nm NIR laser (2 $W\cdot cm^{-2}$) for 0-5 min and were cultured for another 24 h. 10 μL of MTT was added into each well and incubated for 4 h. The MTT solution was removed and 100 μL DMSO was added to dissolve the formazan crystals. Finally, the absorbance was measured and the cell viability was calculated.

In order to further evaluate the photothermal therapy of H-TiO_2-PEG on cancer cells, MCF-7 or 4T1 cells were cultured in 35 mm dishes. The cells were then incubated with fresh DMEM containing 100$\mu g\cdot mL^{-1}$ of H-TiO_2-PEG for 2 h. The culture media were then replaced by fresh DMEM, and the cells were irradiated by 808 nm NIR (2 $W\cdot cm^{-2}$) for 5 min. The cells were stained with both calcein AM (calcein acetoxymethyl ester) and PI (propidium iodide). The live and died cells were observed by confocal microscopy as previously described.

Toxicity and bio-distribution of H-TiO_2-PEG NPs *in vivo*: In the animal experiments, the animal care and handing procedures were in agreement with the guidelines of the Regional Ethics Committee for Animal Experiments. For assessing toxicity of H-TiO_2-PEG *in vivo*, healthy Blab/C mice were intravenously injected with 200 μL of H-TiO_2-PEG (200 $\mu g\cdot mL^{-1}$). Mice injected with saline were used as the control. Mice were observed for behavioral changes over a one month period. After one month, all mice were sacrificed. The main organs including the heart, liver, spleen, kidney and

lung were preserved in a 10% formalin solution and stained with hematoxylin and eosin (H&E) for histological analysis to assess the toxicity of H-TiO_2-PEG. For evaluating the bio-distribution of H-TiO_2-PEG in mouse body, healthy mice were intravenously injected with 100 μL of H-TiO_2-PEG (200 $\mu g \cdot mL^{-1}$). The mice were sacrificed after 24 h, and the concentration of Ti in main organs were measured by ICP-MS (NexION 300, Perkin-Elmer, US) as described previously [25].

Photothermal therapy of H-TiO_2-PEG NPs *in vivo*: To establish a tumor model, 1×10^6 4T1 cells suspended in 100 μL of serum free medium were inoculated subcutaneously in several female Balb/C mice (5 weeks old). A digital caliper was used to measure the size of tumor. Tumor volume= (tumor length) × (tumor width) $^2/2$. The mice were used for the further experiments when the tumor had grown to 3-4 mm in diameter.

To evaluate *in vivo* photothermal therapy of H-TiO_2-PEG, 4T1 tumor-bearing mice were anesthetized by intraperitoneal injection of chloral hydrate solution (8 wt %) and given an intra-tumor injection with 100 μL of H-TiO_2-PEG aqueous dispersion (100 $\mu g \cdot mL^{-1}$). The tumor sites were irradiated with an 808 nm NIR laser at 2 $W \cdot cm^{-2}$ for 5 min. In order to kill the residual tumor cells, the tumor sites were irradiated each of the following 2 days under the same conditions. The tumor sizes were measured by a digital caliper for 14 days and the tumor volume was calculated according to the formula of tumor volume mentioned above. Relative tumor volumes were calculated as V/V_O (V_O was the tumor volume when the treatment was initiated). Body weight and survival of the mice was also recorded.

2.4 Fabrication of N-doped TiO_2 coatings on nanoporous Si nanopillar arrays

Fabrication of nanoporous Si nanopillar arrays: Ordered arrays of nanoporous Si nanopillar with hexagonal symmetry were fabricated from (100) oriented and highly doped p type Si wafer (B-doped, $\rho < 0.005\ \Omega \cdot cm$) by using a combination of substrate conformal imprint lithography (SCIL) [27] and metal-assisted chemical etching (MaCE) [25]. A 20 nm Au film was deposited as catalyst for the MaCE and the fabrication process is well

described in some previous work [28, 29]. The Au film was removed using a solution of KI and I_2 and the samples were dried with N_2 gas.

Materials and synthesis: Protamine sulfate salt from salmon (PA) was purchased from Sigma-Aldrich and used without purification. Titanium(IV) bis(ammonium lactato) dihydroxide (Ti-BALDH) aqueous solution was purchased from Alfa Aesar. 0.10 g protamine sulfate salt was added to 20 ml of pure H_2O and the catalytic molecules solution was obtained. Similarly, 0.98 g Ti-BALDH (50 wt % aqueous solution) was dissolved into 20 ml of H_2O and a transparent titania precursor solution (pH=6.23) was prepared. The biomimetic layer by layer (LBL) titania deposition approach to prepare N-doped TiO_2/Si core/shell nanopillar arrays is schematically illustrated in Scheme 6-1.

Nanoporous Si nanopillar arrays (Size: 1.0 cm × 1.0 cm) were used as templates, and firstly immersed into catalytic molecular solution (PA 5 wt‰) at room temperature for 30 min. Through capillary effects and electrostatic interactions, the positively charged PA was adsorbed on the surface of Si. After that, the Si nanopillar arrays were removed from the PA solution and rinsed with deionized water. Next, the Si nanopillar arrays with adsorbed PA was immersed into titania precursor solution at room temperature also for 30 min, and induced the hydrolysis and condensation of Ti-BALDH to form the negatively charged TiO_2 layer. After being removed from the Ti-BALDH solution and washed with deionized water, PA/TiO_2 coated Si nanopillars were obtained. By repeating the above steps for several cycles, the thickness of the PA/TiO_2 layer was stepwise increased. After calcination of these samples in Ar at 500 °C for 3 h, nitrogen atoms of the protamine is introduced into the TiO_2 structure as doped element, N-doped TiO_2/Si core/shell nanopillar arrays with nanoporous structure were obtained.

2.5 Characterization of TiO_2 samples

The crystalline structure of the nanoparticles was characterized by X-ray diffraction (XRD, SIEMENS D5000) using Cu-Kα radiation. The samples were characterized by using transmission electron microscopy (TEM, Tecnai F20). Scanning electron microscopy (SEM) images were taken with a

Hitachi S-4800 instrument, where also energy-dispersive x-ray spectrometry (EDS) was carried out. The optical absorption in the range from UV to the visible wavelength was measured by a diffuse reflectance accessory of a UV-Vis spectrometer (Cary 5000 UV-Vis-NIR). The X-ray photoelectron spectroscopy (XPS) analysis was performed by a spectrometer (Kratos Axis Ultra XPS) with monochromatized Al-Kα radiation and an energy resolution of 0.48 eV. Raman spectra analysis was performed with a Renishaw In-Via System utilizing a 514.5 nm incident radiation and a 50 × aperture (N.A. = 0.75), resulting in an ~ 2 μm diameter sampling cross-section. Electron paramagnetic resonance (EPR) spectra were recorded at the temperature of 77 K using a Bruker BioSpin CW X-band (9.5 GHz) spectrometer ELEXYS E500. Light irradiation (for light excited EPR) provided by two lasers (50 mW power) operated at 405 nm and 532 nm using an optical transmission resonator (ER 4104OR, Bruker BioSpin). The nanocrystals were charged in quartz glass tubes connected to N_2 gas. The hyperfine structure (hfs) lines (m_I=-3/2, -1/2, 1/2, 3/2) of the $Cu^{2+}(DTC)_2$ complex ("$Cu^{2+}L_2$" in Figure 3-14) in benzene solution have been used for the correct g factors of studied paramagnetic centre determination (low field maximum amplitude of m_I=-1/2 hfs line attributed to g=2.025). In the following text, the different spectra were presented as: "EPR spectra" (spectra recorded without light irradiation), "light-excited EPR spectra" (spectra recorded under irradiation) "light-induced EPR spectra" ("light-excited EPR spectra" - "EPR spectra"). Time resolved photoluminescence (PL) spectroscopy were measured by a universal streak camera (Hamamatsu C10910 using a slow single sweep unit M10913) in combination with a Czerny–Turner spectrograph (Princeton Instruments Acton SP2300, focal length 300 mm) at room temperature. Steady-state PL spectroscopy was performed by a Czerny–Turner spectrograph (Jobin Yvon SPEX 1000M) with a focal length of 1000 mm. The excitation wavelength of 266 nm was generated by a femtosecond laser (Coherent MIRA 900-F) followed by a puls picker (Coherent Pulse Picker) and a 3rd harmonic generator (APE HarmoniXX THG). Zeta potentials of the samples were obtained from a Malvern Zetasizer Nano ZS.

3. Fast lithium storage performance of black anatase H-TiO_2 nanoparticles

3.1 State of the art

The development of lithium ion batteries (LIBs) with higher energy and power densities are essential for their application in electric vehicles and portable electronic devices [1]. In principle, fabrication of electrode materials with high capacity, high rate, and long cycle life is a major challenge [30]. Titanium dioxide (TiO_2) is considered as one of the promising anode materials for its nontoxicity, low cost, and excellent capacity retention. Moreover, it is more safe due to the high operating voltage by which the formation of solid electrolyte interfaces (SEI) layers and electroplating of lithium can be avoided during cycling [6, 7, 31]. However, the poor rate capability of TiO_2 electrodes, caused by the low electrical conductivity and lithium diffusion coefficient, strongly hindered so far its practical application [8, 32].

Different approaches, such as reducing the particle size of TiO_2 [33, 34], compositing with conductive agents [16, 35-37], have been developed to overcome the electronic and ionic transport limitations and improve the rate capability of TiO_2-based anodes. Very recently, hydrogenated TiO_2 (H-TiO_2) has attracted increasing attraction for fast lithium storage due to its disordered surface layer as well as a large amount of oxygen vacancies, that holding great potenials in high power LIBs [17, 19, 22, 38, 39]. Despite some reports about enhanced LIBs performance of H-TiO_2, the mechanism of the improving electrochemical performance still remains unclear, and its structural properties effect on the lithium storage process is not fully understood. It's generally believed that the presence of Ti^{3+} species resulted in the high electric conductivity, thus, leading to the greatly enhanced rate performance [20, 38, 39]; however, Shin et al. proposed that well balanced Li^+/e^- transport is the key factor [19]; and Xia et al. suggested the higher hydrogen mobility and alleviation of structural distortion in the lithium

insertion/extraction process could also be reasons [22]. In the current stage, to deeper understand the mechanism of the enhanced rate performance of H-TiO_2 is highly desirable for its fundamental study and further application.

Herein, hydrogenated anatase TiO_2 nanoparticles (H-TiO_2) are efficiently synthesized through a H_2 plasma treatment of commercially purchased anatase TiO_2 nanoparticles. Transmission electron microscopy (TEM) results show that a disordered surface layer are formed in H-TiO_2 and X-ray photoelectron spectroscopy (XPS) results demonstrate Ti^{3+} species in H-TiO_2. When used as anode material for LIBs, the obtained H-TiO_2 shows a superior long-term, fast lithium storage capability. The capacities of H-TiO_2 are about 154, 141, 124, and 108 $mAh \cdot g^{-1}$ at the rate of 5, 10, 20, and 40 C, respectively, which is superior to pristine TiO_2 nanoparticles (Pristine-TiO_2, about 126, 109, 91, and 70 $mAh \cdot g^{-1}$ at the corresponding rates). Futhermore, H-TiO_2 remains a capacity of 101 $mAh \cdot g^{-1}$ at 40 C (about $6.7A \cdot g^{-1}$) after 5000 cycles, which is almost 1.7 times of that of the pristine-TiO_2 (61 $mAh \cdot g^{-1}$ after 5000 cycles at 40 C). The scan-rate dependence of the cyclic voltammetry (CV) reveals that the improved rate capabilities of H-TiO_2 can be attributed to the enhanced contribution of pseudocapacitive lithium storage on its surface. Combined with the structural properties of H-TiO_2, it is suggested the disordered surface layer and Ti^{3+} species of H-TiO_2 play important roles for the enhanced pseudocapacitive lithium storage. These results help in understanding the improved LIBs performance of the H-TiO_2, and might be informative for further studies of hydrogenated metal oxide electrodes for high power LIBs.

3.2 Results and Discussions

3.2.1 Optical and microstructure properties of black anatase H-TiO_2 nanoparticles

H-TiO_2 (S_{BET} = 169 $m^2 \cdot g^{-1}$) was obtained in a H_2 plasma treatment of purchased anatase TiO_2 nanoparticles (S_{BET} = 178 $m^2 \cdot g^{-1}$) at 390 °C for 3 h (the detailed parameters and raw materials are given in Experiments and Methods 2.1). Figure 3-1 and 3-2 show the photographs and UV-Vis

absorption spectra of the TiO_2 before and after the plasma-enhanced hydrogenation, respectively; the highly enhanced absorption in the region of visible light clarifies the color change from white to black after the H_2 plasma treatment. If treated without plasma, the obtained TiO_2 powder kept the original white color (Figure 3-1b), indicating the H_2 plasma treatment is more effective than common thermal annealing process for TiO_2 hydrogenation.

Figure 3-3 shows the XRD patterns of pristine- and H-TiO_2. The purchased pristine-TiO_2 nanoparticles demonstrated a major anatase phase (JCPDS card no. 21−1272), and a trace amount of rutile was also observed (JCPDS card no. 21−1272). Almost the same XRD pattern was obtained after the H_2 plasma treatment, indicating that no phase transformation occur in this process. The calculated average crystallite size (using Scherrer equation [40]) of H- and pristine-TiO_2 in the [101] direction is 12.4 nm and 11.9 nm, respectively.

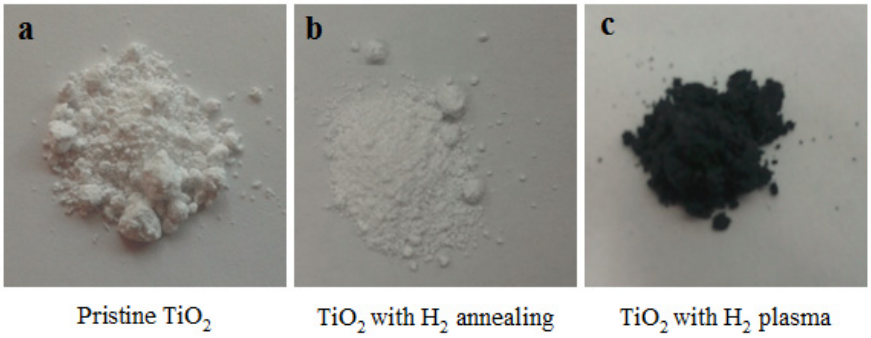

Figure 3-1. The photographs of TiO_2 before and after hydrogenation: (a) Pristine TiO_2. (b) TiO_2 after thermal annealing under H_2 atmosphere without plasma. (c) TiO_2 after H_2 plasma treatment.

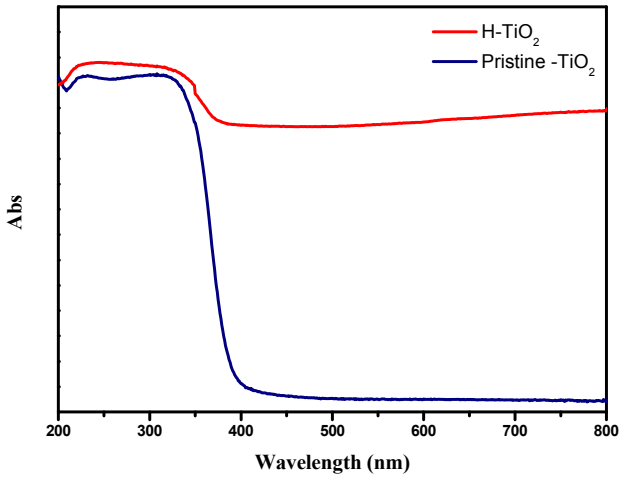

Figure 3-2. UV-vis absorption spectra of pristine- and H-TiO_2.

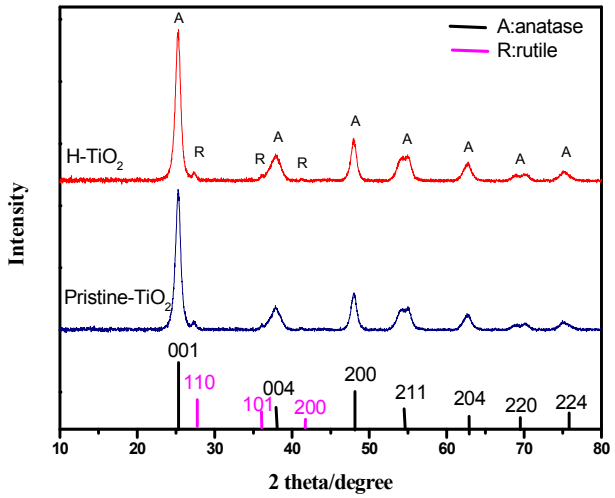

Figure 3-3. XRD pattern of pristine- and H-TiO_2. A represented as diffraction peaks of anatase phase (JCPDS card no. 21−1272, black line); R represented as diffraction peaks of rutile phase (JCPDS card no. 21−1276, pink line).

Figure 3-4 shows the TEM images of pristine- and H-TiO_2. The irregular-shaped particles comprised of numerous tiny nanocrystallites were observed on both samples, and the HR-TEM image of H-TiO_2 demonstrates an obvious disordered surface layer with a thickness of 1.3~1.6 nm, which was not observed for the pristine-TiO_2 surface. XPS analysis was used to investigate the changes of surface chemical bondings of the TiO_2 nanoparticles induced by hydrogenation. The Ti 2*p* core level spectrum of

pristine-TiO_2 shows two peaks at 458.5 and 464.3 eV, corresponding to the Ti $2p_{1/2}$ and Ti $2p_{3/2}$ peaks of Ti^{4+} species [17, 23]; for H-TiO_2, these peaks shift to lower values of 458.2 and 464.1 eV, indicating a different bonding evironment (upper panel in Figure 3-5). Subtracting the Ti 2*p* spectrum of pristine-TiO_2 from that of H-TiO_2, two extra peaks were observed at 457.5 and 463.2 eV, which can be attributed to the Ti $2p_{1/2}$ and Ti $2p_{3/2}$ peaks of Ti^{3+} species (lower panel in Figure 3-5), indicating the presence of Ti^{3+} species in the H-TiO_2 sample [23, 41]. Figure 3-6 shows the O 1*s* spectra of the two samples. Three oxygen features were obtained by peak-fitting of this spectrum: the intense peak located at 529.8 eV is the characteristic peak of Ti-O in anatase TiO_2 [42]; the broad peak centered at round 531.3 eV can be assigned to Ti-O-H [42]; and the small peak at 532.3 eV derived from the H_2O or CO_2 contaminants during sample handling [20]. The content of Ti-O-H signal in O 1*s* spectra was 13.0% and 15.2% for pristine- and H-TiO_2, respectively, implying that H-TiO_2 possesses a higher density of hydroxyl groups, which could modify the electrochemical activity of TiO_2 [23]. Figure 3-7 shows the valance band spectra of the two samples. Pristine-TiO_2 displays the band edge at ~2.4 eV, which is consistent with other reports about anatase TiO_2 [20]. For H-TiO_2, the main absorption onset was also located at ~2.4 eV, while the maximum energy associated with the band tail blue-shifted towards the vacuum level at ~2.0 eV. This change might be induced by the presence of oxygen vacancies (Ti^{3+} species) in H-TiO_2 [43].

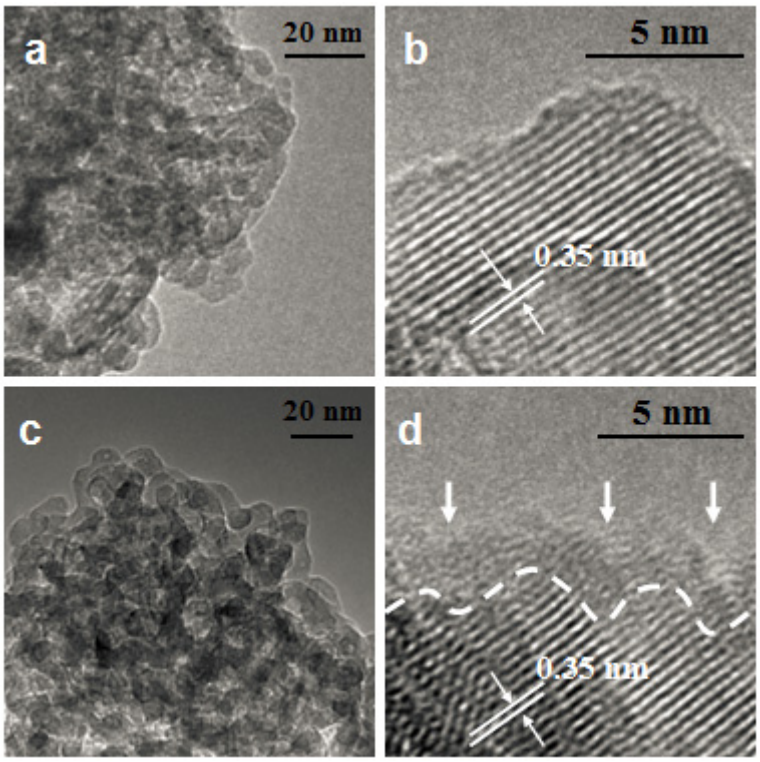

Figure 3-4. TEM and HR-TEM images of the two samples: (a, b) pristine-TiO_2; (c, d) H-TiO_2. A disordered surface layer for the H-TiO_2 with a thickness of 1.3~1.6 nm is indicated by the arrows and margined by the dash line in Figure 3-4d; 0.35 nm is the lattice fringe of the anatase [101] face in Figure 3-4b and 3-4d.

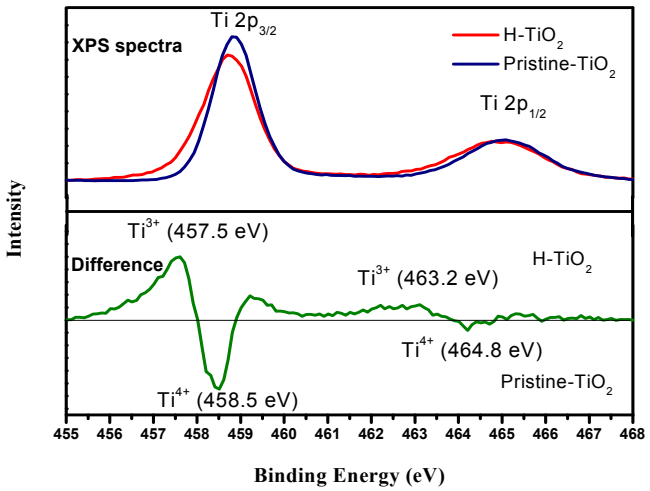

Figure 3-5. XPS Ti 2p core level spectrum of pristine- and H-TiO_2 (upper panel), and the difference spectrum obtained by subtracting the spectrum of the pristine-TiO_2 from that of the H-TiO_2 (lower panel).

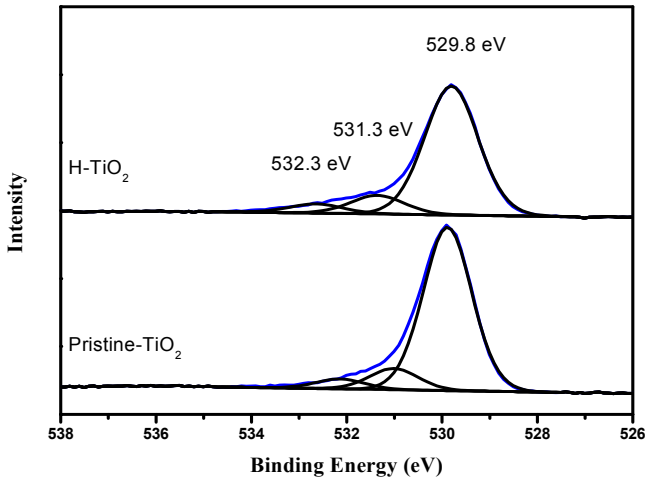

Figure 3-6. XPS O 1*s* core level spectrum of pristine- and H-TiO_2. (The blue lines are the measured spectra; The black lines are the fitting spectra)

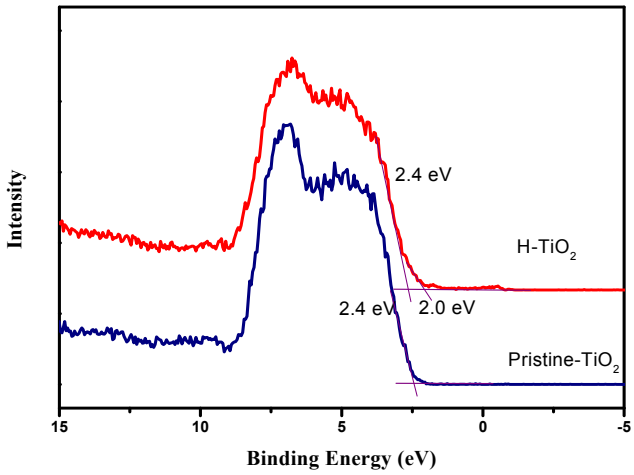

Figure 3-7. XPS valence band spectra of pristine- and H-TiO_2.

3.2.2 Lithium storage performance of black anatase H-TiO_2 nanoparticles

The lithium-storage performance of pristine- and H-TiO_2 was evaluated. Figure 3-8a shows the initial galvanostatic charging/discharging curves of pristine- and H-TiO_2 at the rate of 0.2 C in the potential window of 1.0-3.0 V (1 C=168 mAh·g^{-1}). For H-TiO_2, an initial discharge capacity of 269.8 mAh·g^{-1} and a charge capacity of 208.5 mAh·g^{-1} were obtained; and the pristine-TiO_2 demonstrated a slightly higher initial discharge capacity of

280.3 mAh·g^{-1} and a charge capacity of 213.7 mAh·g^{-1}. The much higher initial charge capacities of both pristine and H-TiO_2 than theoretical capacity of TiO_2 were mainly caused by their surface reactions with the electrolyte and interfacial lithium storage [44]. The discharge curve for an anatase electrode can be divided into three different voltage regions [34, 44-46]. In the first region, the voltage rapidly dropped from 3.0 to about 1.7 V (vs. Li^+/Li), corresponding to the formation of a solid solution domain ($x < 0.2$ in Li_xTiO_2); in the second region, a typical plateau is observed at a potential of 1.7 V, where Li-rich phase ($0.2 < x < 0.5$ in Li_xTiO_2) are expected to coexist with anatase TiO_2; in the third region, the voltage decreased slowly from 1.7 to 1.0 V, signifying the further lithium storage occurred at particle surfaces ($x > 0.5$ in Li_xTiO_2). Compared with pristine-TiO_2, H-TiO_2 shows an increase of lithium storage in the first (0.16 Li^+ Vs 0.10 Li^+) and third region (0.29 Li^+ Vs 0.26 Li^+), but a decrease of lithium storage in the second region (0.27 Li^+ Vs 0.30 Li^+), which might be attributed to the existence of the disordered surface layer. It was suggested that the lithium storage in the third region results from the pseudocapacitance effect which is the charge storage of lithium ions from faradaic reactions occurring at the surface of the materials (also called interfacial lithium storage); interestingly, such lithium storage is irreversible at low rates, and reversible storage of lithium is able to occur in this voltage region only at high rates [44, 47].

Figure 3-8b displays the rate performance of pristine- and H-TiO_2 at charging/discharging rate between 0.2 and 40 C. The capacities of H-TiO_2 are about 187, 163, 151, 132, 118, 97, and 72 mAh·g^{-1} at the rates of 0.2, 1, 2, 5, 10, 20, and 40 C, respectively; while pristine-TiO_2 maintains 190, 159, 142, 114, 89, 60, and 31 mAh·g^{-1} at the corresponding rates. It is worth noting that the capacities of H-TiO_2 are close to those of pristine-TiO_2 at low rates (0.2-2 C), but clearly higher than those of pristine-TiO_2 at high rates (5-40 C). To further investigate its fast lithium storage performance, higher starting charging/discharging rates (1 and 5 C) were applied, and the H-TiO_2 demonstrated higher capacities at every step than pristine-TiO_2 (Figure 3-8c and 3-8d). Interestingly, both pristine- and H-TiO_2 shows significantly higher capacities and less degradation than those obtained from step-wise cycling starting from the rate of 0.2 C (Figure 3-8b, 3-8c, and 3-8d). Especially for

the starting rate of 5 C, H-TiO_2 displays an excellent rate performance with 154, 141, 124 and 108 mAh·g^{-1} at 5, 10, 20 and 40 C, which is much higher than that starting from 0.2 C. And pristine-TiO_2 exhibits 126, 109, 90 and 70 mAh·g^{-1} at the corresponding rates, which is also higher than that starting from 0.2 C. Similar phenomena were also observed for hierarchical porous TiO_2 nanoparticles [44].

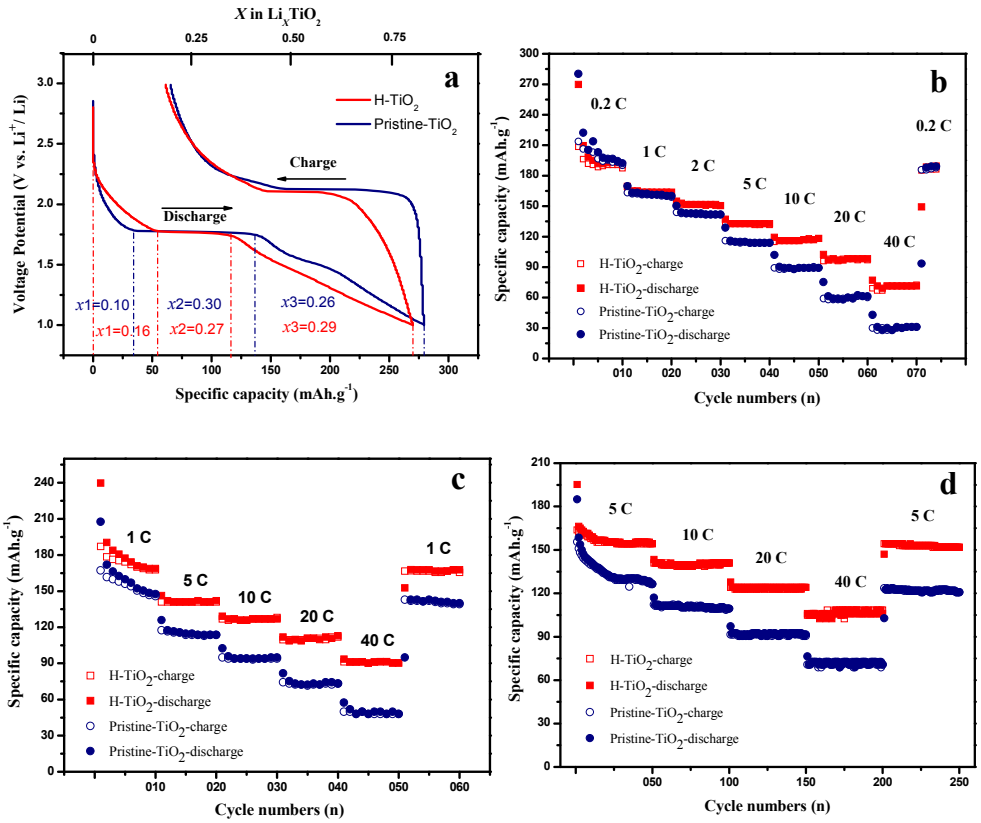

Figure 3-8. (a) The initial galvanostatic charging/discharging profiles for pristine- and H-TiO_2 electrodes. (b) The rate performance of pristine- and H-TiO_2 electrodes between 0.2 C and 40 C. (c) The rate performance of pristine- and H-TiO_2 electrodes between 1 C and 40 C. (d) The rate performance of pristine- and H-TiO_2 electrodes between 5 C and 40 C.

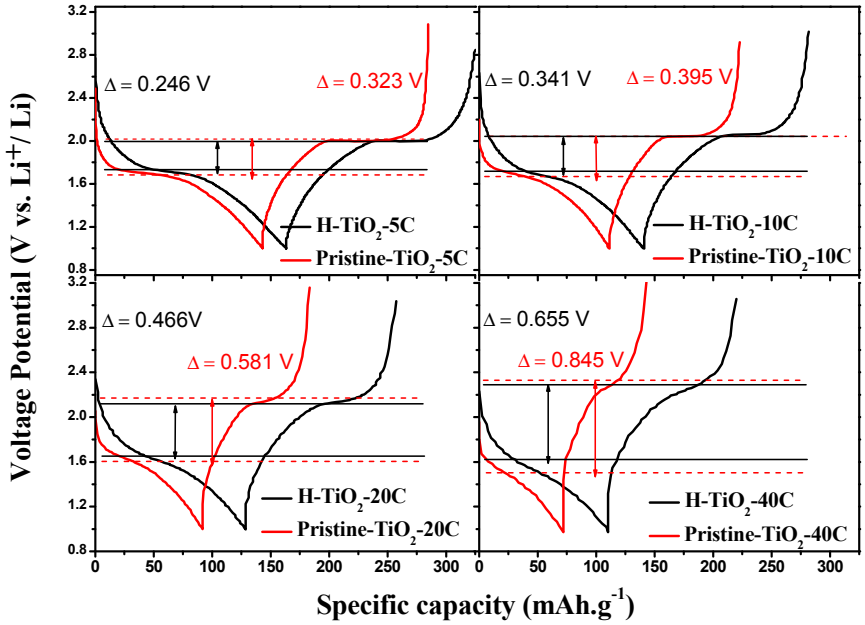

Figure 3-9. Polarization of ΔE versus rate of pristine- and H-TiO2 electrodes. (Details are given in Figure)

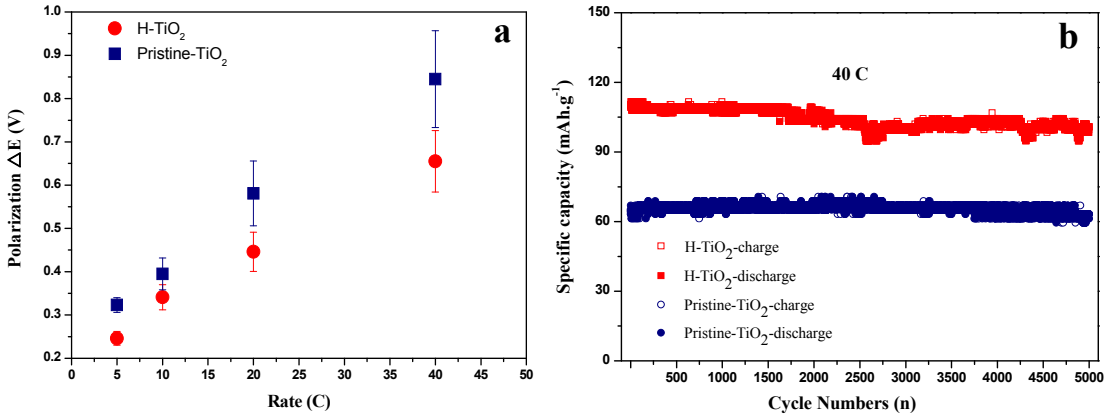

Figure 3-10. (a) Polarization of ΔE versus rate plots of pristine- and H-TiO2 electrodes. (b) Cycling performance of pristine- and H-TiO2 electrodes at high current rate of 40 C.

3.2.3 The mechanism analysis for the fast lithium storage performance of black anatase H-TiO2 nanoparticles

An explanation for this might be the irreversible lithium insertion occurring in the third region at initial low rate (0.2 C), leading to the lower capacities in the subsequent cycles at higher rates. When the material was initially

measured at a high rate (5 C), the lithium storage in the third region was believed to be reversible, thus, resulting in higher capacities in the following cycles at higher rates. In order to understand the remarkable rate performance of H-TiO_2 compared with pristine-TiO_2, the charging/discharging curves at 5, 10, 20 and 40 C were analyzed for both pristine- and H-TiO_2 (Figure 3-9). It was observed that the polarization of ΔE (defined as the differences between the potentials of charge plateaus and discharge plateaus) of H-TiO_2 is 0.246, 0.341, 0.446, and 0.655 V at 5, 10, 20, and 40 C, respectively, which is obviously smaller than those of pristine-TiO_2 (ΔE is 0.323, 0.395, 0.581, and 0.845 V at 5, 10, 20, and 40 C, respectively in Figure 3-10a). The smaller polarization of H-TiO_2 might be attributed to its low ohmic resistance of electrode resulting from the existence of Ti^{3+} species, thus, leading to the enhanced rate performance in LIBs. Even at a high rate of 40 C, a capacity of 101 $mAh \cdot g^{-1}$ can still be delivered after 5000 cycles for H-TiO_2, wheras the remained capacity of pristine-TiO_2 is only 61 $mAh \cdot g^{-1}$ under the similar condition (Figure 3-10b).

For deeper understanding of the pseudocapacitance effect on rate peformance of H-TiO_2, cyclic voltammetry (CV) analysis was performed. Figure 3-11a shows cyclic voltammetry (CV) curves of pristine- and H-TiO_2 electrodes measured at the scan rate of 0.1 $mV \cdot s^{-1}$. The CV curves of H-TiO_2 show a pair of cathodic/anodic peaks at 1.72 and 2.01 V, respectively, which corresponds to the characteristic lithium ion insertion/extraction potentials for the anatase TiO_2, and also agrees well with the charging/discharging potential plateaus of galvanostatic curves (Figure 3-8a). Furthermore, a shoulder peak was observed at 1.40~1.50 V for both pristine- and H-TiO_2, which might be attributed to the further lithium storage occurring at nanoparticle surfaces/interfaces. It is worth to note that the shoulder peak of H-TiO_2 is bigger than that of pristine-TiO_2. The densities of cathodic and anodic current increased significantly at higher scan rates over the entire potential window for both pristine- and H-TiO_2, and the increase of the cathodic/anodic and shoulder peaks current densities for H-TiO_2 is more than those of pristine-TiO_2 (Figure 3-11b and 3-11c). Figure 3-12a shows the dependence of the discharge peak current density I_p on the scan rate v for H-TiO_2; and the similar scan rate dependence is also observed for the charge

peak current. The best fit of the data to an apparent power-law dependence yields $I_p \propto v^{0.70}$. The apparent exponent value is mainly depending on the lithium storage mechanism [44, 47-49]. For bulk lithium insertion dominated processes, the apparent exponent value is close to 0.5 ($I_p \propto v^{0.5}$); while the apparent exponent value is close to 1 ($I_p \propto v$) in surface pseudocapacitive lithium storage. Therefore, the apparent exponent value of 0.70 for H-TiO_2 could presumably be attributed to a mixed process involving both the lithium insertion in the bulk of TiO_2 lattice and the pseudocapacitive lithium storage associated with particle surfaces [47, 49]. For comparison, the apparent exponent value is 0.55 for pristine-TiO_2, suggesting that the bulk lithium insertion is the predominant contribution (Figure 3-12b). The mixed lithium storage process can be presented by the following equation [47]:

$$I_p = I_c + I_d = C_1 v + C_2 v^{1/2} \qquad (1)$$

where I_p is peak discharge current density; v is the scan rate; $C_1 v$ and $C_2 v^{1/2}$ correspond to the current contributions from the surface pseudocapacitive effect (I_c) and bulk lithium insertion process (I_d), respectively. Thus, by determining C_1 and C_2, the current contributions from two processes can be quantified.

For analytical purposes, Eq. (1) is rewritten as

$$I_p / v^{1/2} = C_1 v^{1/2} + C_2 \qquad (2)$$

In Eq. (2), C_1 and C_2 correspond to the slope and the y-axis intercept point of the peak current straight line, respectively. For H-TiO_2, the best fit of the data to Eq. (2) yields C_1=(0.663 ± 0.005) ($Ag^{-1}V^{-1}s$) and C_2=(0.028 ± 0.002) ($Ag^{-1}V^{-1/2}s^{1/2}$), (as indicated in Figure 3-13a). From these parameters, the respective values of I_c and I_d at various scan rates can be determined, allowing for the evaluation of the relative contribution of bulk and surface lithium storages for H-TiO_2. Figure 3-14a shows the calculated surface pseudocapacitive current and bulk intercalative current density as a function of the scan rate for H-TiO_2. At a low scan rate (0.1 $mV \cdot s^{-1}$), I_c is much smaller than I_d, indicating that the bulk lithium insertion is dominated lithium storage. With the increasing of the scan rates, both I_d and I_c increased; but the value of I_c grows much faster than I_d, and became larger than I_d as the

scan rate higher than 2 $mV \cdot s^{-1}$, suggesting that the surface pseudocapacitive storage dominates the total storage capacity at high scan rates. On the other hand, C_1=(0.158 ± 0.002) ($Ag^{-1}V^{-1}s$) and C_2 =(0.032 ± 0.001) ($Ag^{-1}V^{-1/2}s^{1/2}$) were obtained by the same analysis for prisitine-TiO_2 (as indicated in Figure 3-13b). Figure 3-14b displays the calculated I_d and I_c for pristine-TiO_2 varying with the scan rate; however, the I_d is still much larger than I_c even at high scan rates, indicating the bulk lithium insertion is the dominated storage process. These results suggest the H-TiO_2 possesses a higher surface pseudocapacitve lithium storage than prisitine-TiO_2 at high scan rates, which could effectively enhance the rate performance [47, 49, 50]. The explanation might be that the disordered surface layer in H-TiO_2 may provide more active sites for faradiac reactions than the crystalline surface in pristine-TiO_2, and induce more surface pseudocapacitive lithium storage which has much faster kinetics than those of a bulk insertion at high rates [47-50]; besides, the introduction of Ti^{3+} species (oxygen vacancies) improve the electric conductivity of H-TiO_2 [20, 23, 38]. As a consequence, fast lithium storage process can stably occur in H-TiO_2.

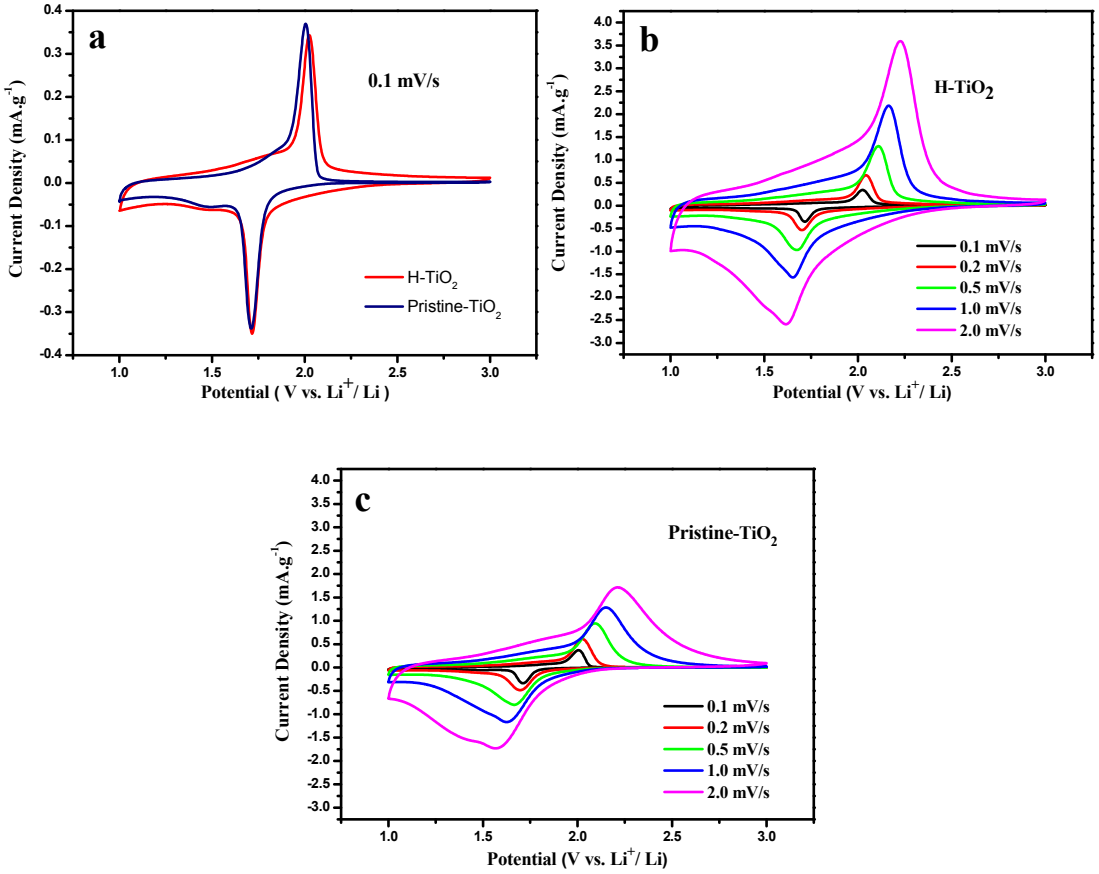

Figure 3-11. (a) Cyclic voltammograms of pristine- and H-TiO_2 electrodes at a scan rate of 0.1 mV·s^{-1}. (b) Cyclic voltammograms of H-TiO_2 electrodes at various scan rates. (c) Cyclic voltammograms of pristine-TiO_2 electrodes at various scan rates.

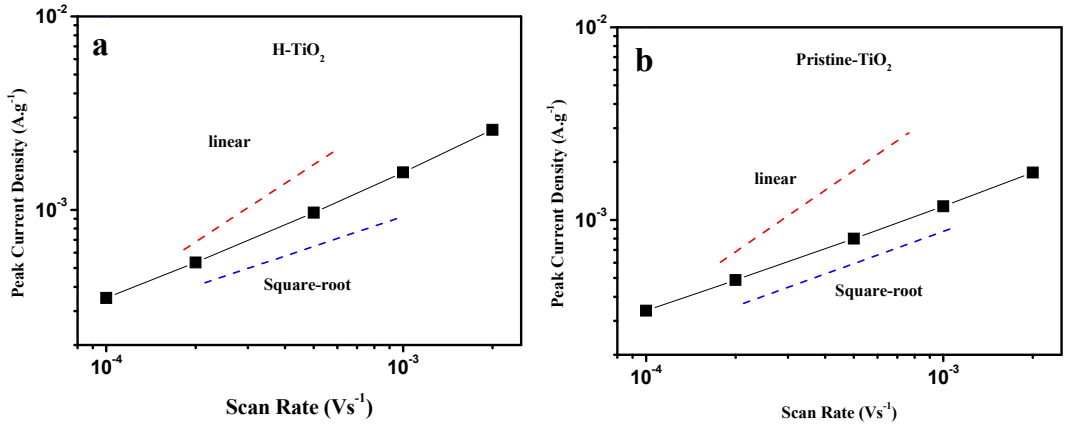

Figure 3-12. The peak discharge current of pristine- and H-TiO2 electrodes measured at various scan rates. (a) H-TiO2 electrode. (b) Pristine-TiO2 electrode. Linear (red dashed line) represented as $I_p \propto v$ in surface pseudocapacitive lithium storage process; Square-root (blue dashed line) represented as $I_p \propto v^{0.5}$ in bulk lithium insertion process.

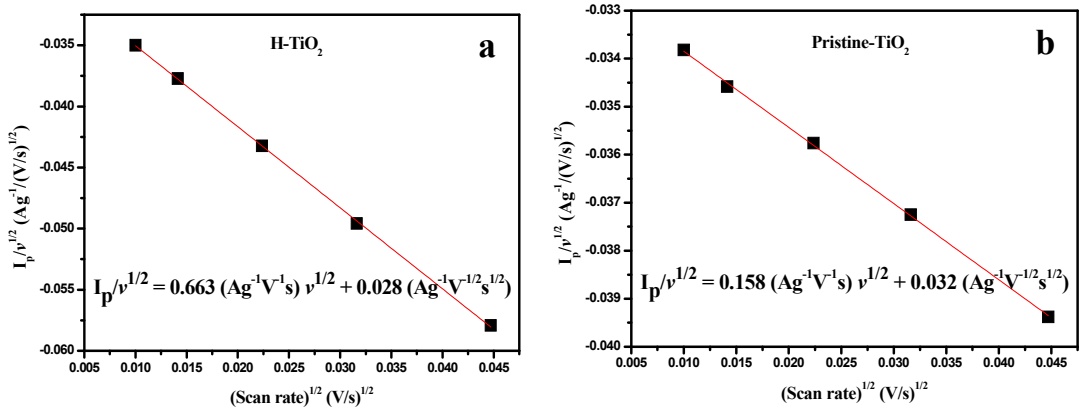

Figure 3-13. The calculated C_1 and C_2 for two samples using Eq. (2) that correspond to the slope and the y-axis intercept point, respectively. (a) H-TiO2. (b) Pristine-TiO2. (The red line is fitting curve)

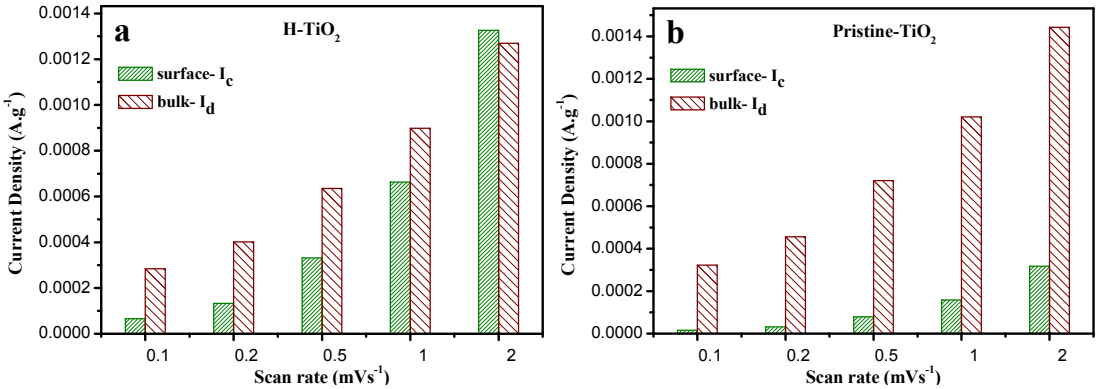

Figure 3-14. (a) Calculated surface pseudocapacitive and bulk insertion discharge currents of H-TiO_2 electrodes. (b) Calculated surface pseudocapacitive and bulk intercalative discharge currents of pristine-TiO_2 electrodes.

3.3 Conclusion

In summary, hydrogenated anatase TiO_2 nanoparticles (H-TiO_2) with disordered surface layer and Ti^{3+} species were efficiently prepared by a H_2 plasma treatment, which showed improved fast lithium storage capability compared to those of pristine TiO_2 nanoparticles. The electrochemical measurements demonstrated that the improved rate capability of H-TiO_2 can be attributed to the enhanced contribution of pseudocapacitive lithium storage on its surface; and it is suggested that the presence of Ti^{3+} species and the disordered surface layer might be the key factors for the enhanced pseudocapacitance effect.

4. Slightly hydrogenated TiO_2 with enhanced photocatalytic performance

4.1 State of the art

Solar-driven catalytic process has attracted much attention, since it provide a promising "green chemistry" approach for treating a wide variety of emerging pollutants, H_2 production from water, or direct conversion of CO_2 to value-added fuels (CO, CH_4, CH_3OH, etc.) [2, 51, 52]. In principle, fabrication of high active photocatalysts which can efficiently utilizing solar energy is a major challenge [53]. Titania (TiO_2) is regarded as a suitable photocatalyst due to its favorable band-edge positions, high chemical inertness, low cost, and long-term stability [20]. However, the efficiency of TiO_2 is limited due to its large band-gap and fast electron-hole recombination [54]. Hence, many studies have been devoted to overcome such problems through different approaches, which include doping with metal or nonmetal elements [9, 12], controlling the structure and facets [15, 55], and introducing defects into nanocrystals [14].

Recently, hydrogenation treatment of TiO_2 has triggered intense research interests. In this process, hydrogenerated TiO_2 (H-TiO_2) with a highly disordered surface layer and a large amount of oxygen vacancies is obtained, which leads to a substantially improved optical absorption in the visible light and near-infrared region [17, 18, 43, 56-58]. Therefore, H-TiO_2 usually shows a grey or black color, and exhibits superior activity for the photocatalytic degradation of organic contaminants and water splitting [17, 57-63]. Photo-electrochemical analysis reveals that the enhanced photoactivity of H-TiO_2 is mainly due to the improved incident photon to current conversion efficiency (IPCE) in the UV region [21, 57]. It is believed that the formation of Ti-H and Ti-O-H bonds on the surface of H-TiO_2 nanoparticles improve the separation of photo-generated electrons and holes [13, 17, 59, 64]; and the presence of Ti^{3+} species or oxygen vacancies increase the donor density of H-TiO_2, thus, facilitate the charge transportation in these nanoparticles [21, 57, 65]. On the other hand, a

significantly worse photoactivity of H-TiO_2 has also been reported, and it is proposed that the poor photocatalytic performances might be ascribed to the formation of bulk defects with high temperature hydrogenation treatment [66]. In addition, the concentration of defects, and their distribution between the surface and bulk of nanocrystals is found to play an important role in enhancing the photoactivity of H-TiO_2 [67].

Despited these achievements, several problems need to be addressed for the further understanding the enhanced photoactivity of H-TiO_2: First, the properties of photo-generated electrons and holes in H-TiO_2 have not been investigated, which have distinct dependence on its photocatalytic performance. Second, it still remains unclear whether the large solar absorption (grey or black color) of H-TiO_2 induced by disordered surface layer or high concentration of defects is really the critical factor for its excellent photocatalytic performance. Third, with the different hydrogenation methods, the structure of the obtained H-TiO_2 usually have many differences, hence, a clear assessment of the key factors in the enhanced photoactivity of H-TiO_2 by comparing these samples is not easy to achieve.

In this work, H-TiO_2 with different hydrogenation degrees are rapidly synthesized through H_2 plasma treatment at 150 °C; and their photocatalytic activity are evaluated by methylene blue (MB) degradation and CO_2 reduction in aqueous and gaseous media, respectively. The slightly hydrogenated TiO_2 with the original white color (s-H-TiO_2) have the increased UV absorption and surface defects, and exhibit enhanced photoactivity compared to pristine TiO_2 (pristine-TiO_2) especially in CO_2 reduction. In contrast, the grey or black H-TiO_2 with higher hydrogenation degrees (h-H-TiO_2) have the highly improved visible light absorption, disordered surface layer, and a large amount of bulk defects, display much worse catalytic performances. Further investigations reveal that the increased surface defects of s-H-TiO_2 lead to the higher ratio of trapped holes (O^- centers) and lower recombination rate, which might be the critical factors for its improved photoactivity; while the high concentration of bulk defects in h-H-TiO_2 act as charge annihilation centers, most of photo-generated holes are consumed through significantly enhanced non-radiative recombination, which strongly inhibit the activity of h-H-TiO_2. These results might provide

new insights into the photoactivity of H-TiO_2, and pave the way for further studies of other hydrogenated metal oxides for photocatalytic applications.

4.2 Results and Discussions

4.2.1 Optical and microstructure properties of H-TiO_2 nanoparticles with different hydrogenation degrees

Hydrogenated TiO_2 (H-TiO_2) were obtained in a high-power density H_2 plasma treatment of purchased TiO_2 nanoparticles (Degussa P25) at 150 °C with different reaction times (the detailed parameters are given in Experiments and Methods 2.2). The TiO_2 powder kept the original white color after 30 s (H-TiO_2-30s); then, TiO_2 with slightly yellow color was observed after 1 min (H-TiO_2-1min); and the color changed into grey after 3 ~ 5 min (H-TiO_2-3min and H-TiO_2-5min); with 20 min H_2 plasma treatment, black TiO_2 was obtained (H-TiO_2-20min). Figure 4-1 shows the UV-Vis absorption spectra of pristine- and H-TiO_2. The absorption of H-TiO_2 in the region of visible light gradually increased into a high level with the extending of hydrogenation time, which clarifies the color change process from white to black. More interestingly, the slightly hydrogenated TiO_2 prepared by 30 s ~ 1 min H_2 plasma treatment (s-H-TiO_2) demonstrated an obviously improved absorption in UV region, and this improvement almost disappeared in the grey or black H-TiO_2 with higher hydrogenation degrees (h-H-TiO_2, 3 min ~ 20 min H_2 plasma treatment). It is suggested that the enhanced UV absorption might be induced by the formation of surface defects in s-H-TiO_2, the similar results has also been observed in the other materials, however, the mechanism of this phenomenon still remained unclear [68, 69].

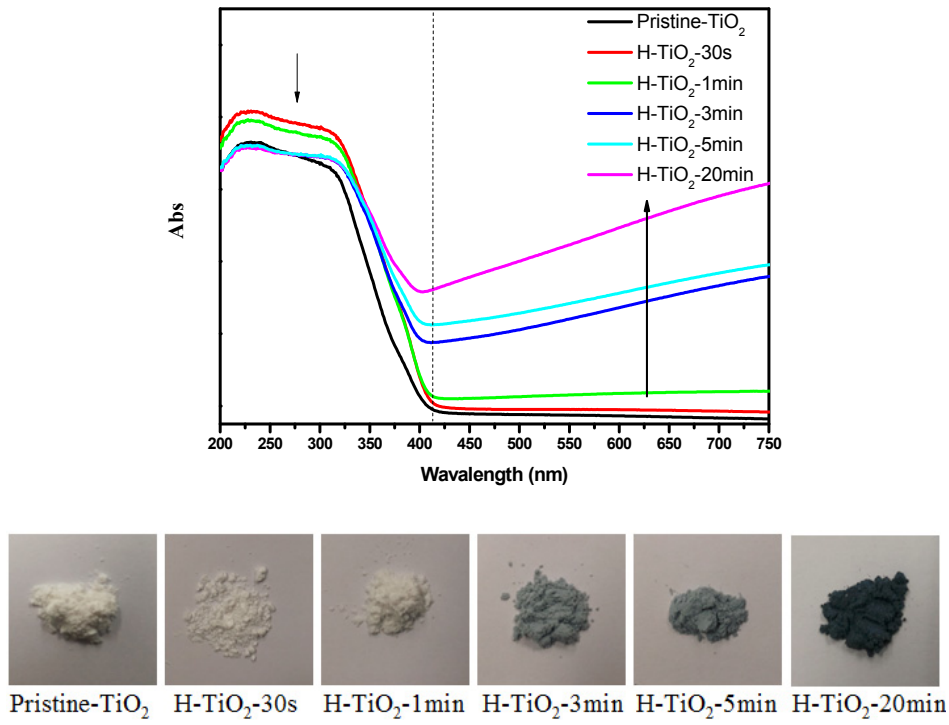

Figure 4-1. UV-vis absorption spectra and related photographs of the pristine-TiO_2 and H-TiO_2 prepared by H_2 plasma treatment after different times of 30 s, 1 min, 3 min, 5 min, and 20 min. (Pristine-TiO_2 represented as pristine TiO_2; H-TiO_2-30s, H-TiO_2-1min, H-TiO_2-3min, H-TiO_2-5min, and H-TiO_2-20min represented as hydrogenated TiO_2 with 30 s, 1 min, 3 min, 5 min, and 20 min H_2 plasma treatment, respectively.)

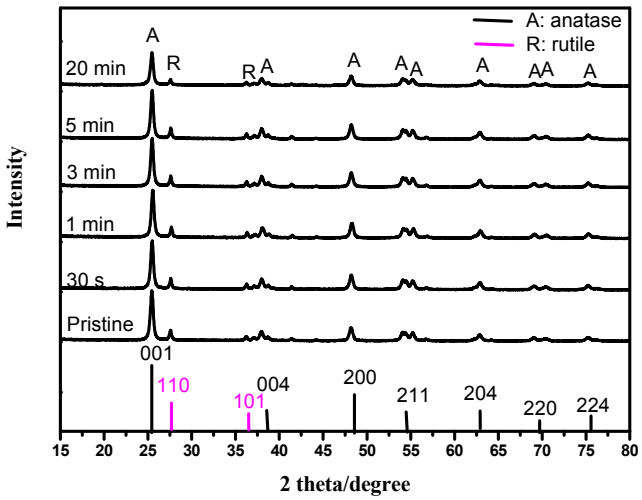

Figure 4-2. XRD patterns of the pristine-TiO_2 and H-TiO_2 prepared by H_2 plasma treatment after different times of 30 s, 1 min, 3 min, 5 min, and 20 min. A represented as diffraction peaks of anatase phase; R represented as diffraction peaks of rutile phase.

Figure 4-2 shows the XRD patterns of the pristine-TiO_2 and H-TiO_2 with different times of hydrogenation. The purchased pristine-TiO_2 nanoparticles demonstrated a major anatase phase (JCPDS card no. 21−1272) coexisting with small amount of rutile (JCPDS card no. 21−1276). After H_2 plasma treatment with 30 s to 5 min, the obtained H-TiO_2 displayed almost the same XRD patterns, indicating that no phase transformation occurred in the process. However, the peak intensity of TiO_2 significantly decreased after 20 min, and the calculated average crystallite size (using Scherrer equation [40]) of this sample in the [101] direction is 17.6 nm, which is smaller than that of pristine-TiO_2 (19.3 nm). This change might be induced by the high concentration of defects in TiO_2 nanoparticles [57].

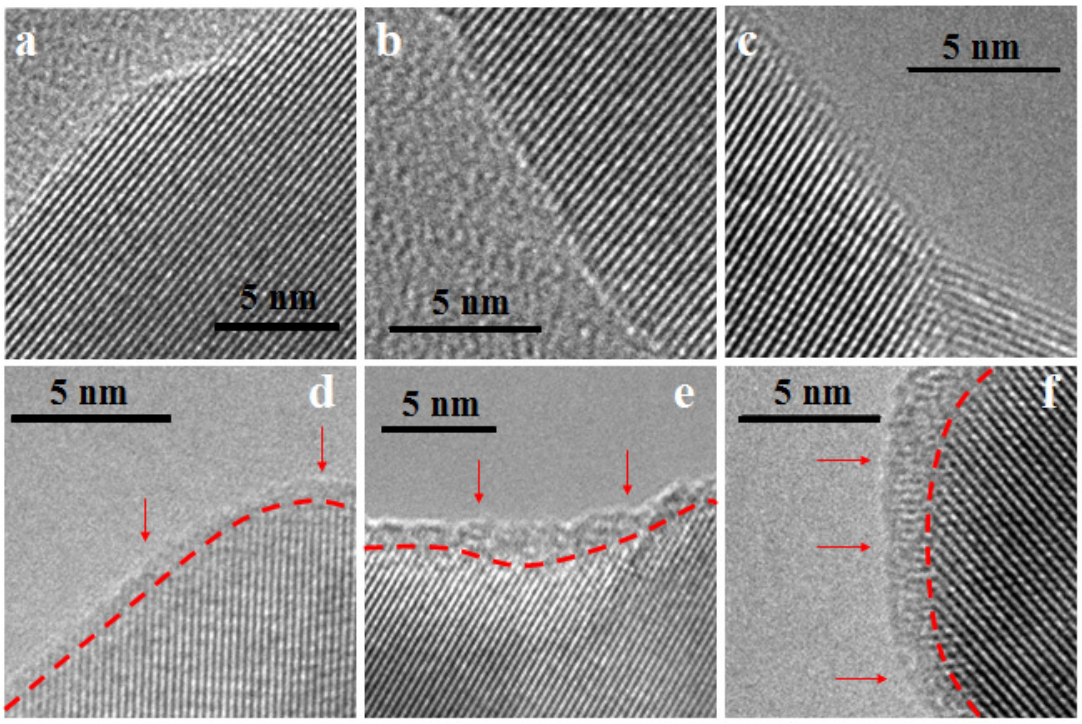

Figure 4-3. HR-TEM images of the pristine-TiO_2 and H-TiO_2 prepared by H_2 plasma treatment after different times: (a) Pristine-TiO_2; (b) H-TiO_2-30s; (c) H-TiO_2-1min; (d) H-TiO_2-3min; (e) H-TiO_2-5min; (f) H-TiO_2-20min.

Figure 4-3 shows the HR-TEM images of pristine-TiO_2 and H-TiO_2 with different times of hydrogenation. The pristine-TiO_2 and s-H-TiO_2 were highly crystallized, as seen from the well-resolved lattice features shown in Figure 4-3a-c. After 3 min, a disordered layer (0.5 ~ 0.9 nm) was formed on the surface of TiO_2 nanoparticles (Figure 4-3d). Further prolonging the reaction time, the thickness of disordered layer increased into 1.0 ~ 1.6 and 1.5 ~ 2.2 nm after 5 and 20 min, respectively. As Raman spectra are more sensitive to disordered phase, this method was used to further investigate the structural changes of TiO_2 after different times of hydrogenation. Pristine-TiO_2 demonstrated typical anatase Raman bands at 149 cm^{-1} (E_g), 195 cm^{-1} (E_g), 397 cm^{-1} (B_{1g}), 516 cm^{-1} (A_{1g} + B_{1g}), and 638 cm^{-1} (E_g) [20]. s-H-TiO_2 showed the similar patterns as pristine-TiO_2; and the peak intensity of H-TiO_2 obviously decreased upon hydrogenation time up to 3 min; after 20 min, H-TiO_2 had only a broad peak at 149 cm^{-1} with the disappearance of the other peaks, which were the characteristics of the existence of disordered

phase (Figure 4-4) [70, 71]. These results are consistent with the observation in HR-TEM images.

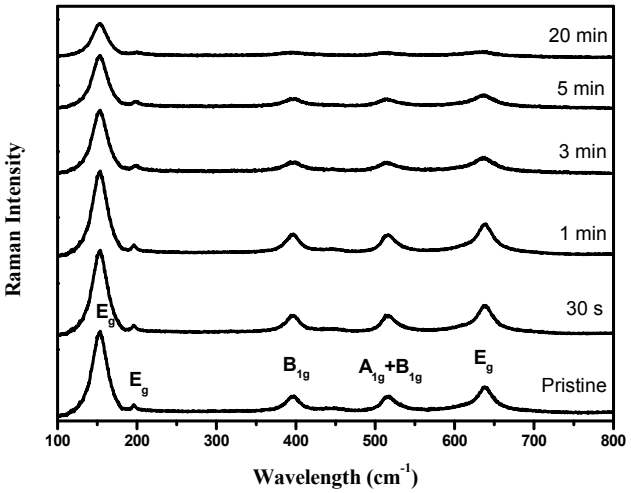

Figure 4-4. Raman spectra of the pristine-TiO_2 and H-TiO_2 prepared by H_2 plasma treatment after different times of 30 s, 1 min, 3 min, 5 min, and 20 min.

XPS analysis was used to investigate the changes of surface chemical bondings of the TiO_2 nanoparticles induced by hydrogenation. The Ti 2*p* core level spectrum of pristine-TiO_2 showed two peaks at ~ 458.6 and ~ 464.7 eV, corresponding to the Ti $2p_{1/2}$ and Ti $2p_{3/2}$ peaks of Ti^{4+} species [17, 23]; for H-TiO_2-30s, these peaks negative shifted to ~ 458.3 and ~ 464.5 eV, indicating a different bonding environment (upper panel in Figure 4-5a). Subtracting the Ti 2*p* spectrum of pristine-TiO_2 from that of H-TiO_2-30s, two extra peaks were observed at ~ 457.9 and ~ 463.6 eV, which can be attributed to the Ti $2p_{1/2}$ and Ti $2p_{3/2}$ peaks of Ti^{3+} species (lower panel in Figure 4-5a), indicating the presence of Ti^{3+} species on the surface of TiO_2 nanoparticles after 30 s of H_2 plasma treatment [23, 41]. Surprisingly, the Ti 2*p* peaks of H-TiO_2 re-shifted to higher values with the extending of hydrogenation time, and even closed to pristine-TiO_2 after 20 min (Figure 4-5b). By subtracting the Ti 2*p* spectrum of these H-TiO_2 with pristine-TiO_2, all obtained difference spectrums showed the Ti $2p_{1/2}$ and Ti $2p_{3/2}$ peaks of Ti^{3+} species, but the intensity of these peaks significantly decreased with increasing of hydrogenation time (Figure 4-5c). It is suggested that oxygen vacancies (Ti^{3+} sites) initially formed on the surface of TiO_2 nanoparticles under H_2 plasma treatment, and preferentially diffused into the bulk with further

hydrogenation [67, 72]. The O 1*s* spectra are almost identical for the pristine-TiO_2 and all H-TiO_2 (Figure 4-6). Two oxygen features were obtained by peak-fitting of this spectrum: the intense peak located at 529.7 eV is the characteristic peak of Ti-O in anatase TiO_2; the broad peak centered at around 531.3 eV can be assigned to Ti-O-H [42]. The content of Ti-O-H signal in O 1*s* spectra remained at ~ 10.0% before and after different times of H_2 plasma treatment, implying that hydrogenation process has a negligible effect on the density of hydroxyl groups of the TiO_2 surface. The valence band (VB) maxima were estimated by linear extrapolation of the peaks to the baselines, the pristine-TiO_2 and all H-TiO_2 displayed the band edge at ~ 2.4 eV (Figure 4-7). This result have also been observed in the other studies [20, 57], which demonstrated that oxygen vacancies (or Ti^{3+} species) created by hydrogenation process could induce the formation of additional electronic states below the conduction band (CB) of TiO_2 [43, 57, 59-61, 73]. In this case, the gray or black color of H-TiO_2 with the substantially enhancement of visible light absorption might be attributed to the transitions from the TiO_2 VB to these additional electronic states or from these additional electronic states to the TiO_2 CB [57].

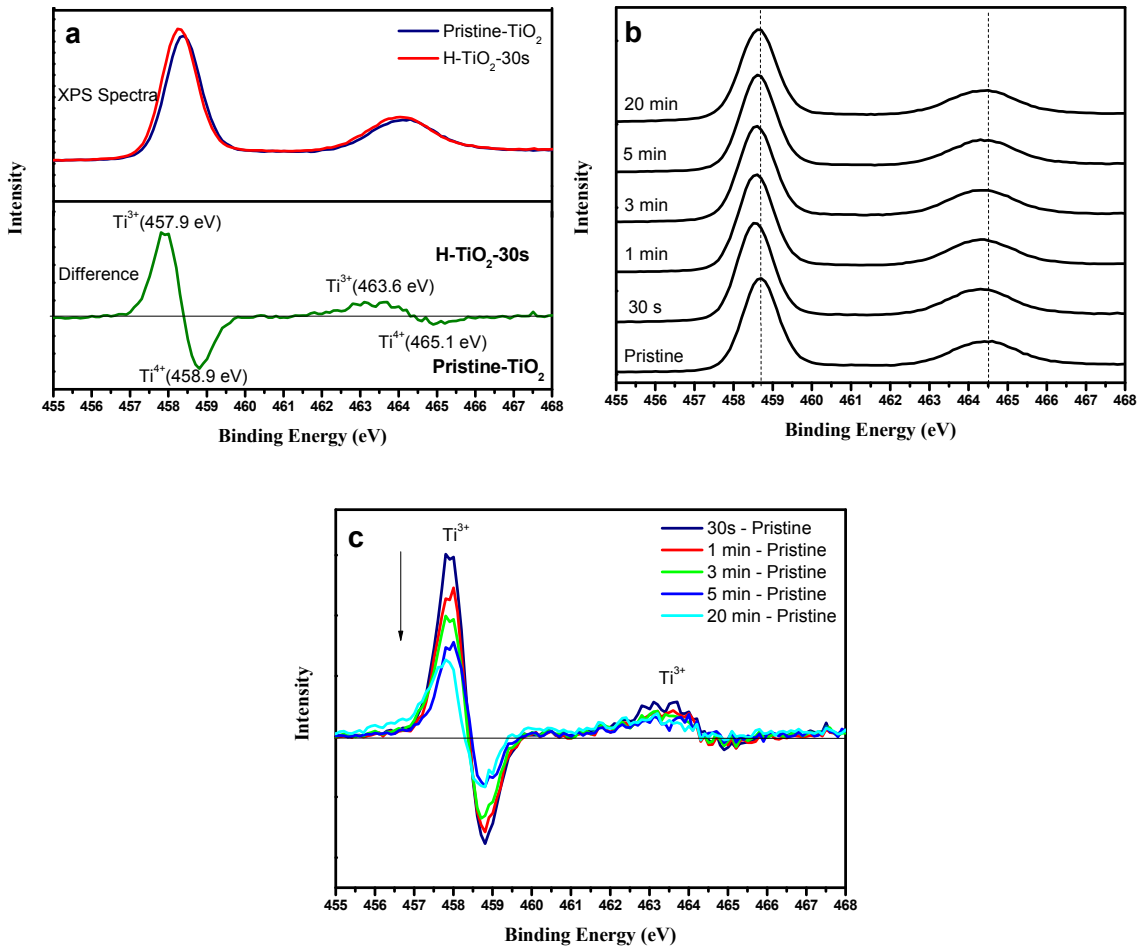

Figure 4-5. (a) XPS Ti 2*p* core level spectrum of the pristine-TiO_2 and H-TiO_2-30s (upper panel), and the difference spectrum obtained by subtracting the spectrum of the pristine-TiO_2 from that of the H-TiO_2-30s (lower panel). (b) XPS Ti 2*p* core level spectrum of the pristine-TiO_2 and H-TiO_2 prepared by H_2 plasma treatment after different times of 30 s, 1 min, 3 min, 5 min, and 20 min. (c) The difference spectrum obtained by subtracting the spectrum of the pristine-TiO_2 from that of H-TiO_2-30s, H-TiO_2-1min, H-TiO_2-3min, H-TiO_2-5min, and H-TiO_2-20min.

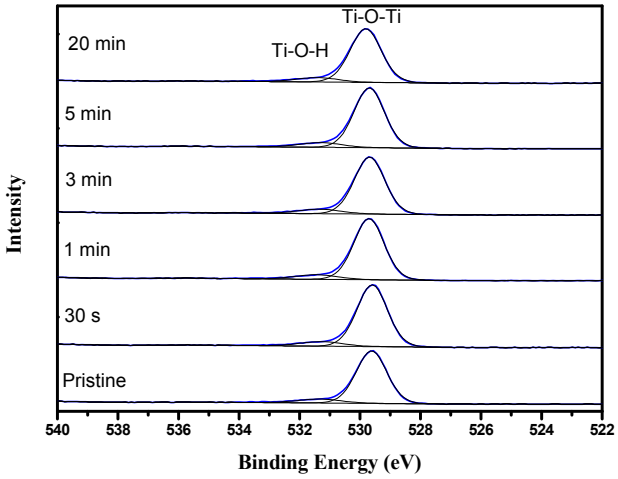

Figure 4-6. XPS O 1*s* core level spectrum of the pristine-TiO_2 and H-TiO_2 prepared by H_2 plasma treatment after different times of 30 s, 1 min, 3 min, 5 min, and 20 min. (The blue lines are the measured spectra; The black lines are the fitting spectra)

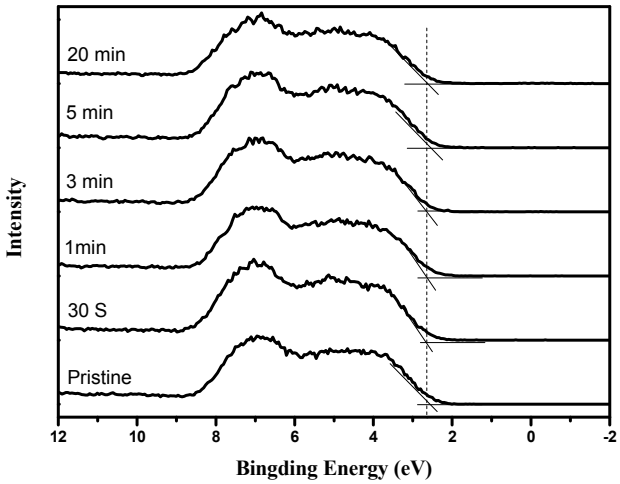

Figure 4-7. XPS valence band spectra of the pristine-TiO_2 and H-TiO_2 prepared by H_2 plasma treatment after different times of 30 s, 1 min, 3 min, 5 min, and 20 min.

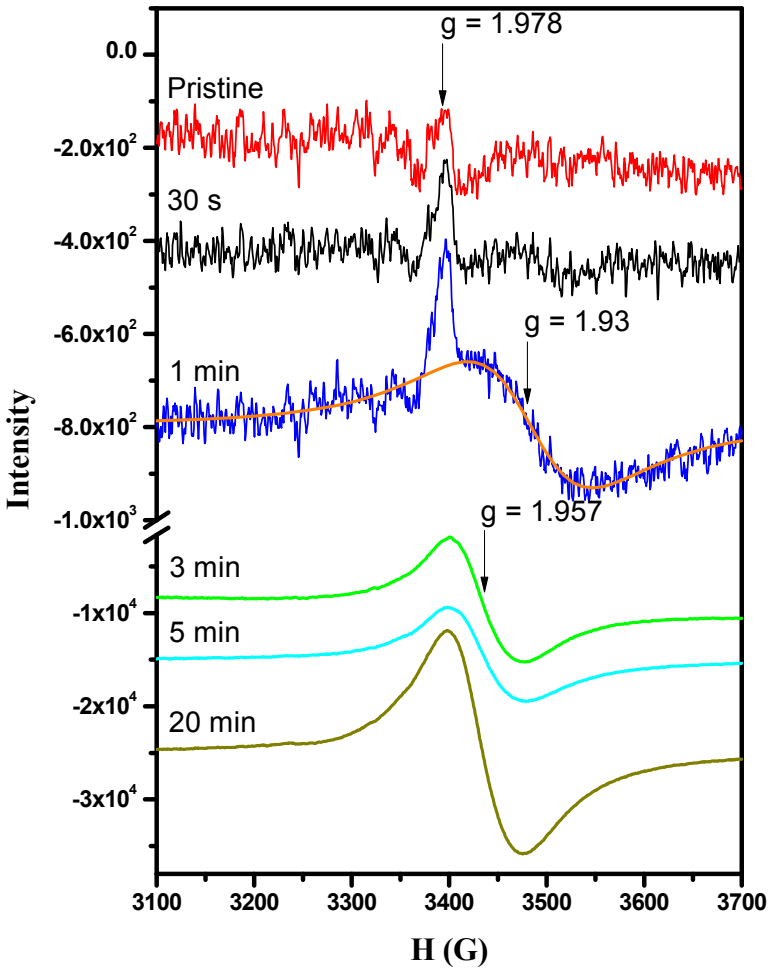

Figure 4-8. EPR spectra of the pristine-TiO_2 and H-TiO_2 prepared by H_2 plasma treatment after different times of 30 s, 1 min, 3 min, 5 min, and 20 min recorded at 77 K without light irradiation. (orange line presented as the simulated signal at an average g-value of 1.93)

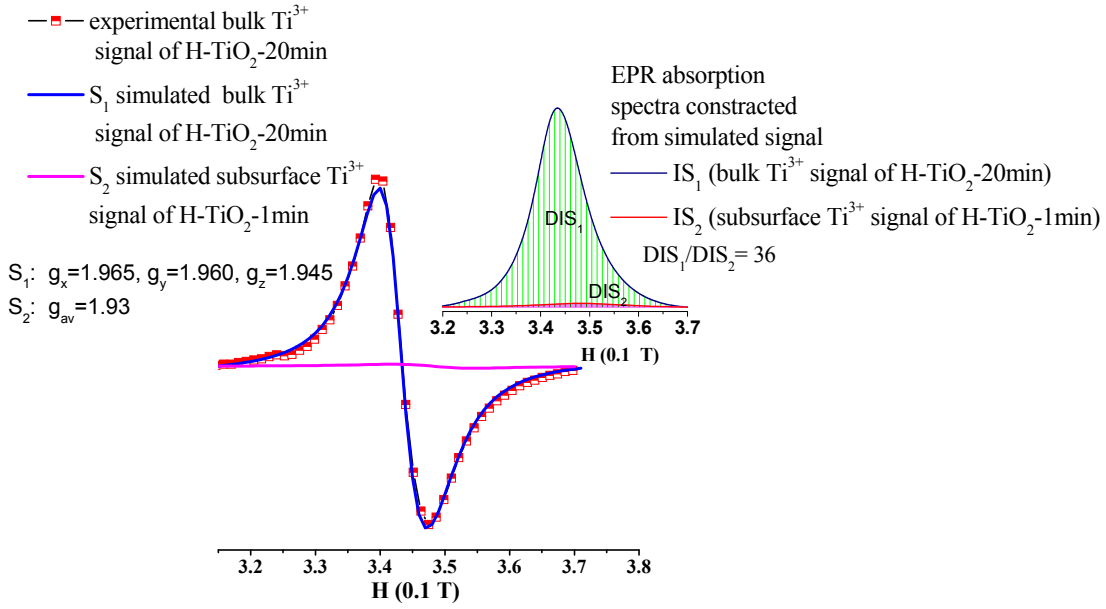

Figure 4-9. The experimental and simulated bulk Ti^{3+} signal of H-TiO_2-20min, and the simulated subsurface Ti^{3+} signal of H-TiO_2-1min without light irradiation, the relative amount of Ti^{3+} was appraised through the double integration of the resonance lines: S_1 and S_2 represented as signal 1 and 2, respectively; IS_1 and IS_2 represented as the integration of the signal 1 and 2, respectively (EPR absorption spectra); DIS_1 and DIS_2 represented as the double integration of the signal 1 and 2, respectively (green and red area in EPR absorption spectra).

Electron paramagnetic resonance (EPR) were measured to further investigate the concentration and distribution of defects in H-TiO_2, because it is highly sensitive to detect paramagnetic species containing unpaired electrons, and has been widely used to characterize the existence of Ti^{3+} species and oxygen vacancies. As indicated in Figure 4-8, pristine-TiO_2 presented a weak response at a g-value of ~ 1.978, which might be ascribed to the original surface or interstitial defects in TiO_2 (Ti^{3+} species) [74, 75]. After 30 s of H_2 plasma treatment, the H-TiO_2 exhibited a stronger peak with the same g-value, which indicated an increase of surface defects. After 1 min, the intensity of the surface defects signal further increased; and a broad signal at an average g-value of ~ 1.93 was also observed, which might result from the Ti^{3+} species existed in the subsurface of TiO_2 [76, 77]. After 3 min, the H-TiO_2 sample showed a much stronger signal at an average g-value of ~ 1.957 (g_x=1.965, g_y=1.960, g_z=1.945), the intensity of this signal is about 2

orders of magnitude higher than the surface Ti^{3+} species in s-H-TiO_2 (30 s ~ 1 min), implying the presence of a large amount of Ti^{3+} species in the bulk [43, 78, 79]; Prolonging the hydrogenation time to 20 min, the signal at an average g-value of ~ 1.957 with higher intensity was observed, revealing that the amount of Ti^{3+} species in the bulk further increased (~ 40 times of H-TiO_2-1min, Figure 4-9). These results demonstrated that the H_2 plasma treatment induced the formation of Ti^{3+} species on the surface of TiO_2 at early stage (30 s ~ 1 min), and a large amount of bulk Ti^{3+} species were formed with longer times of hydrogenation (3 ~ 20 min).

4.2.2 Photocatalytic performance of H-TiO_2 nanoparticles with different hydrogenation degrees

The photocatalytic activities of H-TiO_2 were evaluated by methylene blue (MB) degradation and CO_2 reduction in aqueous and gaseous media, respectively. For MB degradation, s-H-TiO_2 exhibited better photocatalytic activities than pristine-TiO_2 (Figure 4-10): H-TiO_2-30s completed the decomposition of MB in 12 min; and H-TiO_2-1min needed 14 min; while the pristine-TiO_2 took 16 min. In contrast, h-H-TiO_2 showed much worse performance. About 8%, 13%, and 21% of MB remained after 16 min for H-TiO_2-3min, -5min, and -20min, respectively. The kinetics of the degradation reaction were fitted to a pseudo first-order reaction: $\ln(C_0/C)=kt$, where k is the rate constant. The average value of k for pristine-TiO_2, H-TiO_2-30s, -1min, -3min, -5min, and -20min was 0.217, 0.291, 0.255, 0.167, 0.136, and 0.101 min^{-1}, respectively (Figure 4-11). For CO_2 reduction, CH_4 and CO were found to be the two main products, and the similar trend as MB degradation, that the photoactivity of H-TiO_2 decreased with the increasing of hydrogenation degree, was also observed. As shown in Figure 4-12, s-H-TiO_2 demonstrated the enhanced conversion efficiency: the production rate of CH_4 and CO for H-TiO_2-30s was 14.65 and 19.44 $nmol \cdot h^{-1}$, respectively, which was about 2 times of pristine-TiO_2 in the total productivity (7.37 $nmol \cdot h^{-1}$ CO and 11.59 $nmol \cdot h^{-1}$ CH_4); for H-TiO_2-1min, the rate of CH_4 slightly decreased to 14.03 $nmol \cdot h^{-1}$, but the rate of CO increased to 21.67 $nmol \cdot h^{-1}$. The explanation might be that CO_2 is favourably bonded on the surface of H-TiO_2-30s due to its higher density of surface Ti^{3+}

sites (Figure 4-5c), which enhance the immobilization of CO_2 at the surface of the catalyst, allowing a later hydrogenation to form CH_4 instead of CO [80]. For H-TiO_2-3min, the production rate of CH_4 and CO significantly decreased to 9.29 and 13.39 $nmol \cdot h^{-1}$, respectively. Nevertheless, these rates are still slightly higher than that of pristine-TiO_2, which is different with the worse performance of H-TiO_2-3min in MB degradation. This change might be induced by the different charge transfer rate in aqueous/ and gaseous/TiO_2 interface, and reaction kinetics of MB degradation and CO_2 reduction [54]. The catalytic performance of H-TiO_2 further decreased with the extending of hydrogenation time. Especially in CH_4 production, the rate is only 4.37 $nmol \cdot h^{-1}$ for H-TiO_2-5min; and almost no CH_4 signal was observed for H-TiO_2-20min. The mechanism of CO_2 photoreduction with H_2O to form CH_4 and CO can be simply described as following three steps of reaction [80, 81]:

Table 4-1. The mechanism of CO_2 photoreduction with H_2O to form CH_4 and CO

Step 1 { Photogeneration of charges: $TiO_2 \xrightarrow{h\nu} e^- + h^+$

↓

Step 2 { Water photooxidation : $2H_2O + 4h^+ \rightarrow O_2 + 4H^+$

↓

Step 3 { CO_2 photoreduction to CH_4 : $CO_2 + 8H^+ + 8e^- \rightarrow CH_4 + 2H_2O$

CO_2 photoreduction to CO : $CO_2 + 2H^+ + 2e^- \rightarrow CO + 2H_2O$

According to the above mentioned results, it is suggested that the formation of high concentration of bulk Ti^{3+} is counterproductive to the photocatalytic activity of H-TiO_2. As it will be further discussed later, bulk Ti^{3+} species strongly weakened the photooxidative efficacy of h-H-TiO_2 (step 2), which reduced both the productivity as well as the selectivity CH_4/CO ratio [80].

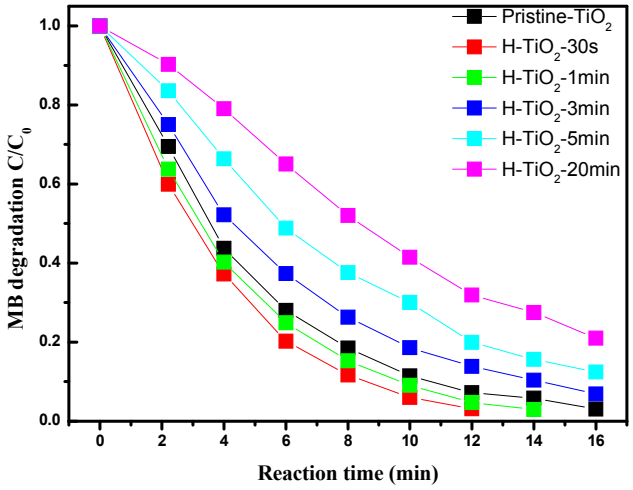

Figure 4-10. Degradation of methylene blue (MB) over pristine-TiO_2 and H-TiO_2 prepared by H_2 plasma treatment after different times of 30 s, 1 min, 3 min, 5 min, and 20 min.

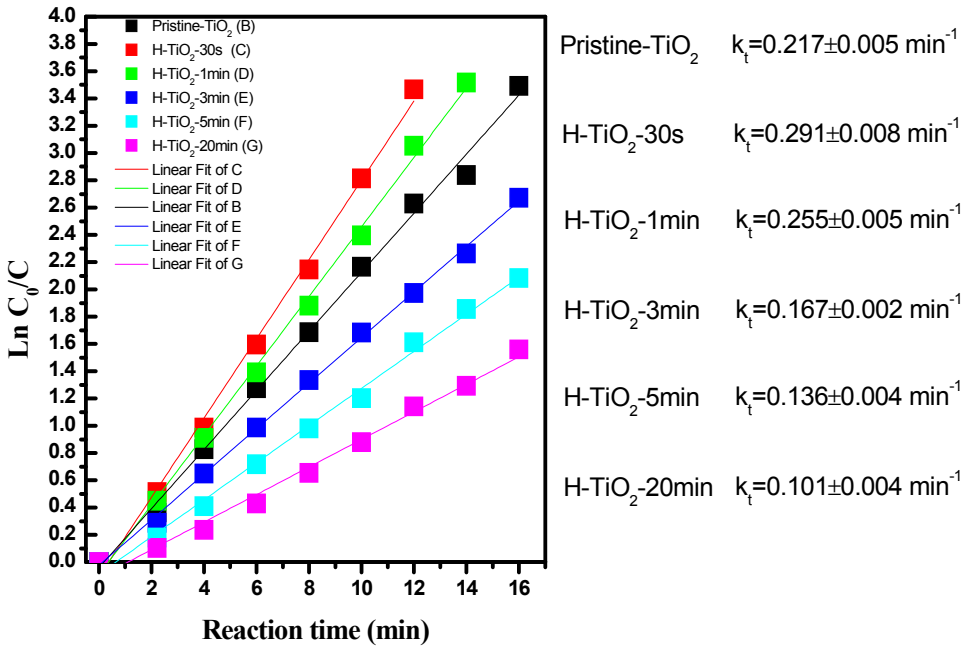

Figure 4-11. Photocatalytic degradation of methylene blue ($\ln C_0/C$ versus irradiation time) over pristine-TiO_2 and H-TiO_2 prepared by H_2 plasma treatment after different times of 30 s, 1 min, 3 min, 5 min, and 20 min and their calculated reaction rates (k_t).

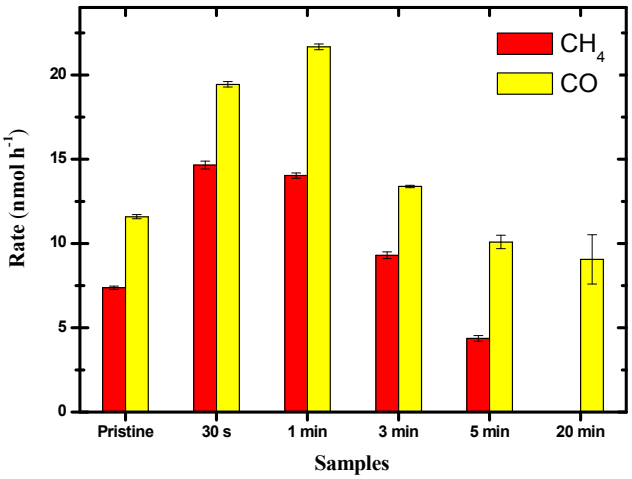

Figure 4-12. The formation rates of CH_4 and CO in the photocatalytic reduction of CO_2 with H_2O over pristine-TiO_2 and H-TiO_2 prepared by H_2 plasma treatment after different times of 30 s, 1 min, 3 min, 5 min, and 20 min.

4.2.3 Photogenerated charge properties of H-TiO_2 with different hydrogenation degrees

In order to study the hydrogenation process affects the charge-trapping centers of TiO_2 formed upon solar light irradiation, in turn, to understand the photoactivity of H-TiO_2. Light-induced EPR measurements were performed under 405 or 532 nm light irradiation (Figure 4-13). For comparison, these spectrums of pristine-TiO_2 and H-TiO_2 have been subtracted by that of the spectrums without light irradiation (Figure 4-14). As shown in UV-vis spectra (Figure 4-1), the pristine-TiO_2 and s-H-TiO_2 display a steep increase in absorption at wavelengths of ~ 420 nm, hence, the irradiation with the wavelength of 405 nm can be used as excitation light source as UV light; on the other hand, the irradiation with the wavelength of 532 nm were used as visible light source. Under 405 nm light irradiation, the pristine-TiO_2 and s-H-TiO_2 showed two well-separated sets of resonance lines. The higher field small peaks with an average g value of ~ 1.960 (g_x=1.970, g_y=1.965, g_z=1.947) can be assigned to electrons trapped on Ti^{3+} centers [74, 82]; the lower field sharp features with an average g value of ~2.013 (g_x=2.022, g_y=2.015, g_z=2.003), corresponding to the holes trapped on O^- sites [74, 82], and their intensity is greater than that of Ti^{3+} peaks. Both O^- and Ti^{3+} signals in s-H-TiO_2 showed lower intensity compared with pristine-TiO_2, indicating

small part of photo-generated charges trapped by the increased surface defects [83]. After 3 ~ 5 min of H_2 plasma treatment, the intensity of O^- signals significantly decreased; and an inverted broad resonances was observed at an average g value of ~ 1.957, implying the deceasing of the amount of Ti^{3+} species in H-TiO_2, which might derive from the combination of the photo-generated holes and the localized bulk Ti^{3+} species (induced by hydrogenation). After 20 min, the O^- signals was almost disappeared, and the intensity of the inverted broad resonances further increased. This result suggested that bulk Ti^{3+} species tend to act as charge carrier traps where most of photo-generated holes were consumed through recombination with electrons [21, 66, 75]. According to the literature, the trapped holes (O^-) and electrons (Ti^{3+}) were considered as the major oxidative and reductive sites in catalytic reactions, respectively [82]; therefore, the ratio of O^-/Ti^{3+} might have an important impact on the competition between photo-oxidation and -reduction process, and thus strongly affect the efficiency of photocatalysis [81, 82]. It is observed that the ratio of O^-/Ti^{3+} is 1.71 for pristine-TiO_2 (the relative amount of Ti^{3+} and O^- can be appraised through the double integration of the resonance lines as shown in Figure 4-15); and this ratio increased to 2.02 and 1.84 for s-H-TiO_2 with 30 s and 1 min H_2 plasma treatment, respectively; in contrast, the ratio of O^-/Ti^{3+} dramatically decreased to less than 0.1 for h-H-TiO_2. These results indicated that s-H-TiO_2 with higher ratio of O^- centers might have enhanced photooxidative efficacy, leading to the improved photocatalytic performance; on the other hand, the worse photoactivity of h-H-TiO_2 might be attributed to the significant reduction of O^- centers, due to the formation of a large amount of bulk Ti^{3+} species with relatively long time hydrogenation. Under 532 nm light irradiation, no O^- signals were observed for the pristine- and H-TiO_2, and these samples also showed very poor visible-light photocatalytic performance in degradation of MB, revealing that the contribution of the dramatically improved visible-light absorbance of H-TiO_2 on its photoactivity is limited. This result is similar as previous reports [21, 57].

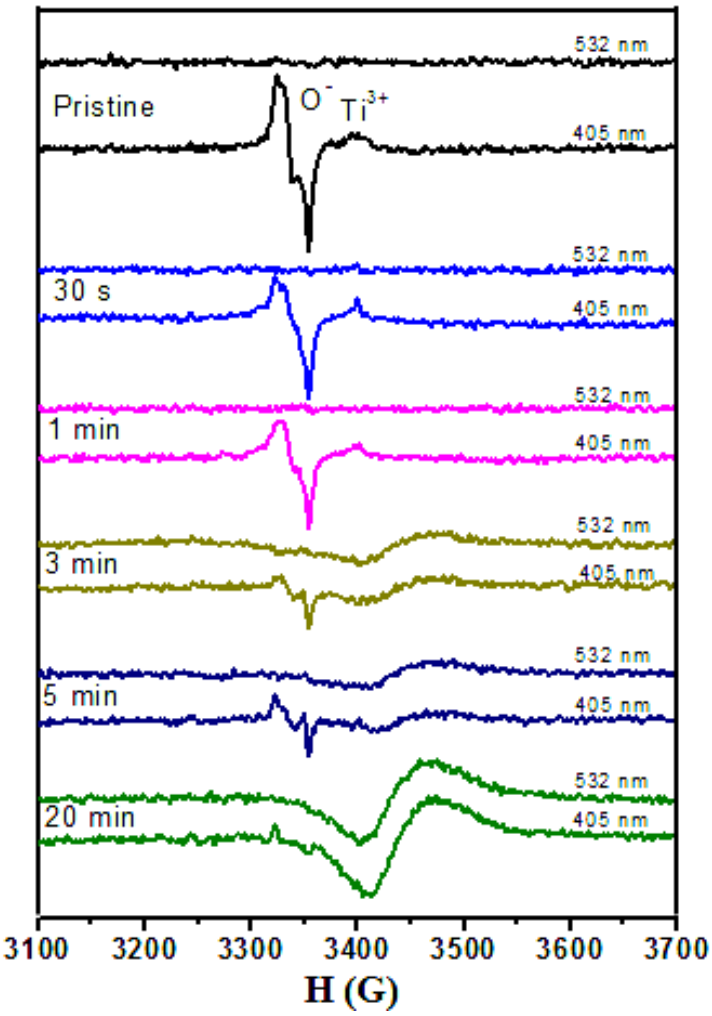

Figure 4-13. Light-induced EPR spectra of the pristine-TiO_2 and H-TiO_2 prepared by H_2 plasma treatment after different times of 30 s, 1 min, 3 min, 5 min, and 20 min recorded at 77 K under 405 or 532 nm light irradiation

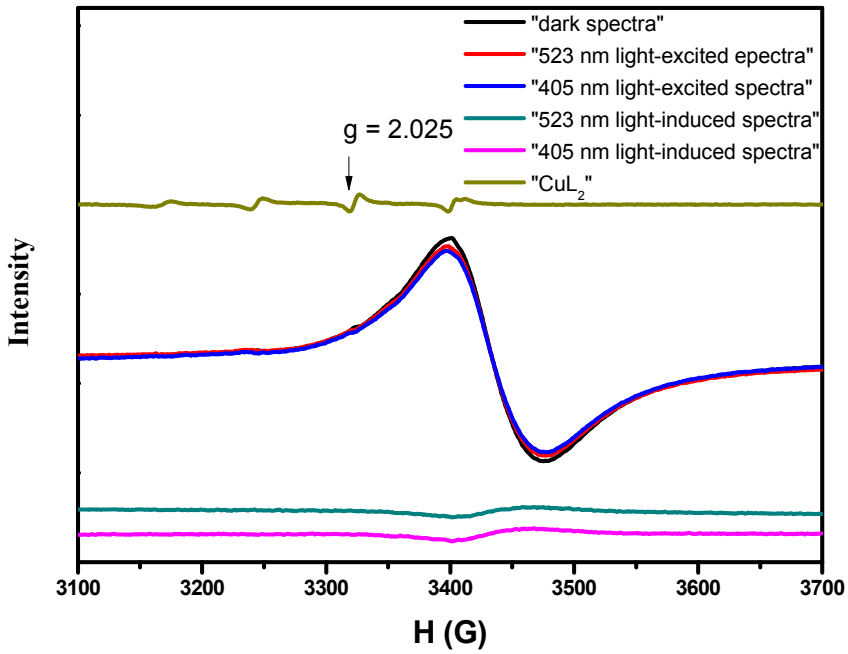

Figure 4-14. EPR analysis of H-TiO_2-20min: “dark spectra” represented as the spectra recorded without light irradiation; “523 nm light-excited spectra” represented as the spectra recorded under 523 nm irradiation; “405 nm light-excited spectra” represented as the spectra recorded under 405 nm irradiation; “523 nm light-induced EPR spectra” represented as the spectra recorded under 523 nm irradiation subtracted by that of the spectra without light irradiation (“523 nm light-excited spectra” - “dark spectra”); “405 nm light-induced EPR spectra” represented as the spectra recorded under 405 nm irradiation subtracted by that of the spectra without light irradiation (“405 nm light-excited spectra” - “dark spectra”). “CuL_2” represented as the hyperfine structure lines of the $Cu^{2+}(DTC)_2$ complex in benzene solution, which has been used as the correct g factors of studied paramagnetic centre determination (low field maximum amplitude of m_I=-1/2 hfs line attributed to g=2.025).

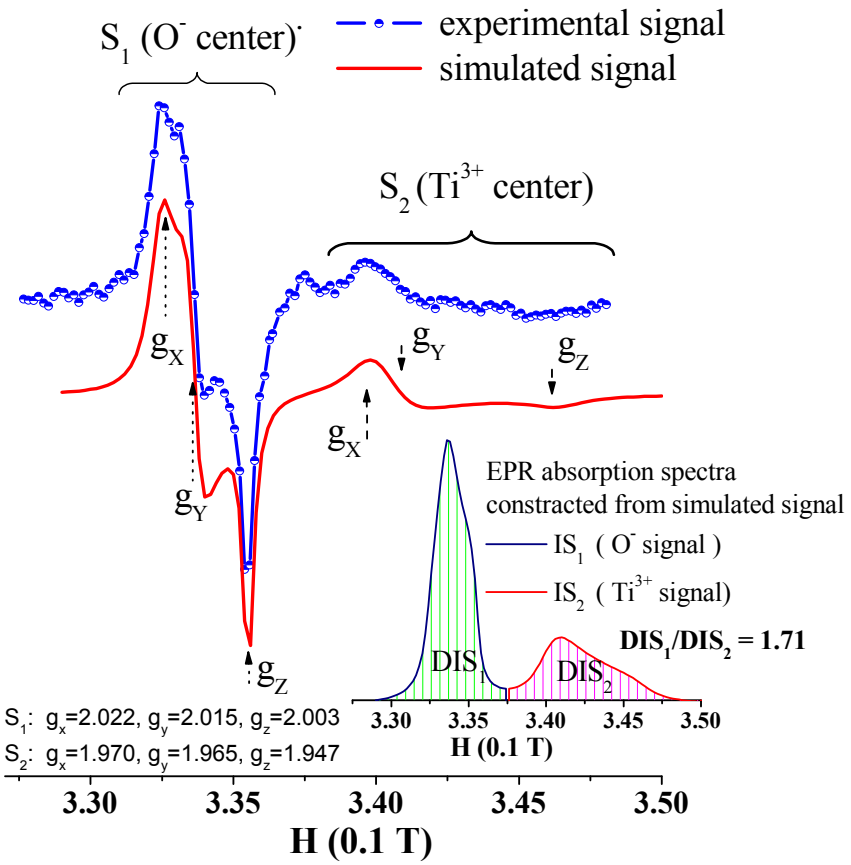

Figure 4-15. The experimental and simulated light-induced EPR spectra of prisine-TiO_2 under 405 nm light irradiation, the relative amount of Ti^{3+} and O^- were appraised through the double integration of the resonance lines: S_1 and S_2 represented as signal 1 and 2, respectively; IS_1 and IS_2 represented as the integration of the signal 1 and 2, respectively (EPR absorption spectra); DIS_1 and DIS_2 represented as the double integration of the signal 1 and 2, respectively (green and red area in EPR absorption spectra).

The photoluminescence (PL) spectra of pristine- and H-TiO_2 in the wavelength range of 420 − 680 nm with excitation at 266 nm are shown in Figure 4-16b. All samples exhibited a broad signal centered around 505 nm, which resulted from radiative transitions involving mobile electrons recombining with hole-trapped states (located 0.7−1.4 eV above the valence band edge), associated with oxygen vacancies in anatase TiO_2 [84, 85]. H-TiO_2-30s showed a more intense and broad signal compared with pristine-TiO_2, due to its higher density of surface Ti^{3+} centers [86]. For H-TiO_2-1min, the intense of signal decreased to close to that of pristine-TiO_2,

which might be induced by the existence of subsurface Ti^{3+} species. For h-H-TiO_2 (3 ~ 20 min), the signal intense significantly decreased with the increasing of hydrogenation time. This trend is consistent with the other reports, and has been considered as lower recombination rate of electrons and holes in H-TiO_2 that favors its high photocatalytic activity [58, 59, 61, 62]. Actually, in addition to radiative recombination releasing photons (detected by PL spectra), non-radiative recombination releasing phonons is a major pathway for the photo-generated charges annihilation in TiO_2 (as indirect band-gap semiconductor). In this process, the energy is exchanged in the form of lattice vibration, and the thermal energy in materials is increased [87, 88]. Hence, the temperature changes of the pristine- and H-TiO_2 suspensions (25 mg TiO_2 in 50 mL water) were measured after 90 min of full-spectrum irradiation (Figure 4-16a). For pristine-TiO_2, the temperature rising was (4.5 ± 0.8) °C, which was obviously higher than that of s-H-TiO_2 ((1.2 ± 0.2) and (1.3 ± 0.2) °C for H-TiO_2-30s and H-TiO_2-1min, respectively). While the temperature rising increased to (5.7 ± 0.9), (5.9 ± 1.0), and (10.3 ± 2.2) °C for H-TiO_2 with 3, 5, and 20 min H_2 plasma treatment, respectively. These results demonstrated that s-H-TiO_2 might have lower non-radiative recombination rate compared with pristine-TiO_2 due to their limited thermal effect, but gray or black h-H-TiO_2 can more efficiently convert light energy into thermal energy, corresponding to their significantly enhanced non-radiative recombination. PL signal decay curves were used to compare the lifetime of photo-generated charges in pristine- and H-TiO_2. As shown in Figure 4-16c, the lifetime of electrons and holes in H-TiO_2 generally decreased with increasing of hydrogenation time. H-TiO_2-30s displayed a slightly longer lifetime than that of pristine-TiO_2, and the lifetime of H-TiO_2-1min was almost the same as pristine-TiO_2. With further hydrogenation (3 ~ 20 min), the lifetime of grey or black H-TiO_2 was shortened compared with pristine-TiO_2. Combined with light-induced EPR analysis, it is demonstrated that the surface defects in s-H-TiO_2 improve the holes trapping, and thus facilitate the separation of photo-generated charge pairs, which results in the lower recombination rate and longer lifetime of them; on the contrary, high concentration of bulk defects in h-H-TiO_2 act as

charge annihilation centers, leading to the enhanced non-radiative recombination and shorter lifetime of electrons and holes.

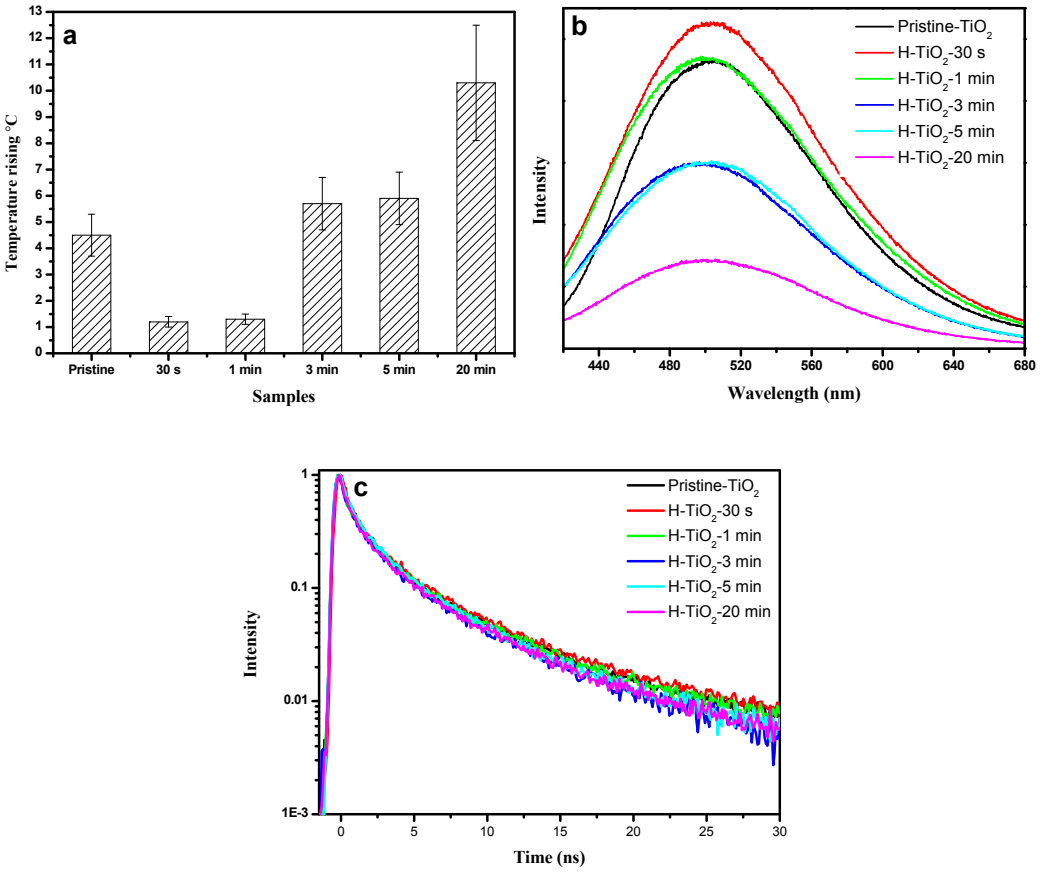

Figure 4-16. (a) Temperature rising of the pristine-TiO_2, H-TiO_2-30s, H-TiO_2-1min, H-TiO_2-3min, H-TiO_2-5min, and H-TiO_2-20min suspensions (25 mg TiO_2 in 50 mL water) after 90 min of full-spectrum irradiation. (b) PL spectra of the pristine-TiO_2 and H-TiO_2 prepared by H_2 plasma treatment after different times of 30 s, 1 min, 3 min, 5 min, and 20 min. (c) PL decay measured for the pristine-TiO_2 and H-TiO_2 prepared by H_2 plasma treatment after different times of 30 s, 1 min, 3 min, 5 min, and 20 min.

4.3 Conclusion

Hydrogenated TiO_2 (H-TiO_2) with different hydrogenation degrees are efficiently synthesized through H_2 plasma treatment in several minutes. The slightly hydrogenated TiO_2 with the original white color (s-H-TiO_2) exhibit enhanced photoactivity compared to pristine TiO_2 (pristine-TiO_2) especially in CO_2 reduction. In contrast, the grey or black H-TiO_2 with higher

hydrogenation degrees (h-H-TiO_2) displays much worse catalytic performances. Further investigations toward the structure and photo-generated charges of H-TiO_2 demonstrate that the improved photocatalytic performance of s-H-TiO_2 can be attributed to the higher ratio of trapped holes (O^- centers) and lower recombination rate induced by the increasing of surface defects; while the high concentration of bulk defects in h-H-TiO_2 act as charge annihilation centers, most of photo-generated holes are consumed through significantly enhanced non-radiative recombination, which strongly inhibit the photocatalytic activity of h-H-TiO_2.

5. Hydrogenatd black TiO_2 nanoparticles as agent for cancer photothermal therapy

5.1 State of the art

TiO_2 has been widely used in many fields such as energy, environment, cosmetics, and food [5, 89]. Its low toxicity, good biocompatibility, stable structure, and unique photocatalytic properties, enalbe TiO_2 nanoparticles being widely applied in biomedicine, especially as an inorganic photosensitizer for photodynamic therapy (PDT) of cancer [90-99]. The principle of PDT is based on the accumulation of a photosensitizer in a tumor; light of a specified wavelength is applied resulting in the generation of reactive oxygen species (ROS) and subsequent killing of tumor cells. The band gap of TiO_2 is 3.23 eV for anatase, which is equal to the energy of UV light at 385 nm. Therefore, upon irradiating light with energies higher than 385 nm (i.e. lower wavelengths), the photo-induced pairs of electrons and holes can induce ROS including O^{2-} and OH^- radicals leading to the killing of cancer cells [91, 92]. Based on the theory of UV light-triggered radical production, cancer PDT of TiO_2 has attracted much attention over the last two decades [90-99]. In 2003, Woloschak's group reported their work in Nature Materials, demonstrating that TiO_2 could be used as an UV light-inducible nucleic acid endonuclease and serve as a new tool for gene therapy [13]. However, due to very shallow penetration and toxicity of UV light, cancer PDT with TiO_2 met obstacles that impeded further clinical applications. Many researchers attempted to change the exciting light from UV to visible light through doping or surface modification [94, 95], but these advances were slowly incremental. Visible light activation does circumvent the mutagenic problems of UV excitation, but it still does not provide optimal penetration through biological tissue.

H-TiO_2 has attracted wide research attention in applications of sustainable energy sources and cleaning of the environment [17, 43, 59, 62, 101, 102]. It has been demonstrated that the enhanced visible and NIR light absorption of H-TiO_2 was mainly due to the formation of oxygen vacancies in the H-TiO_2.

But interestingly, it was argued that the remarkable improved visible and NIR light absorption of H-TiO_2 was not the main reason for the enhanced photocatalytic activity [21]. It was found that incident-photon-to-current-conversion efficiency (IPCE) of H-TiO_2 was higher in the UV region than that of the pristine TiO_2, and this was regarded as the main reason for the enhanced photocatalytic activity of H-TiO_2 [21]. Although the detailed mechanism for the enhanced photocatalytic performance of H-TiO_2 is still unknown and under debate [18, 103, 104], it is accepted that H-TiO_2 possesses high NIR absorption, which is a desired attribute of any agent for cancer photothermal therapy (PTT). As an effective treatment for cancer, the principle of PTT is based on accumulation of photothermal agent in tumor which absorbs and converts NIR light into heat to kill the cancer cells. Compared with traditional therapeutic ways of cancer, such as chemotherapy, radiotherapy and surgery, PTT is targeted, non-invasive, and consequently is high effective, but it does not involve the side effects of traditional therapies. The type of photothermal agent is a key factor for PTT and has attracted research attention [105, 106]. Recently, a variety of inorganic and organic nanomaterials with high photothermal performance have been explored as effective photothermal agents for cancer therapy [107-117]. However, considering the dramatic NIR absorption of H-TiO_2, there is much promise to develop a new NIR triggered photothermal agent based on H-TiO_2 materials.

5.2 Results and Discussions

5.2.1 Optical absorption, defects, and photothermal principle of black H-TiO_2

H-TiO_2 was obtained by a high-power density H_2 plasma treatment based on our previous studies [103, 104]. Figure 5-1a shows the UV-Vis-NIR absorption spectra of pristine- and H-TiO_2. The highly increased absorption of H-TiO_2 in the region of visible and NIR light clarified its color change from white to black (as seen in the inserted pictures in Figure 5-1a), which might be correlated with a large amount of deep level defects (Ti^{3+} species) after H_2 plasma treatment [73]. In addition, electron paramagnetic resonance

(EPR) was measured to investigate the concentration of defects in H-TiO_2. As indicated in Figure 5-1b, no obvious signal was observed for pristine-TiO_2 sample, indicating its limited amount of defects; while the H-TiO_2 sample showed a much stronger signal at an average g-value of ~ 1.957, implying the presence of a large amount of Ti^{3+} species in the bulk of the NPs [78, 79]. It has been demonstrated that Ti^{3+} species created by hydrogenation process could induce the formation of additional electronic states below the conduction band of TiO_2. In this case, H-TiO_2 with the substantial enhancement of visible and near infrared light absorption might be attributed to the transitions from the TiO_2 valence band to these additional electronic states or from these additional electronic states to the TiO_2 conduction band [57, 59, 61].

To understand the photothermal effect of H-TiO_2 through studying the properties of photogenerated charges of H-TiO_2, light-induced EPR measurements were performed under 405 nm light irradiation (Figure 5-1c). For comparison, these spectra of pristine-TiO_2 and H-TiO_2 have been subtracted by that of the spectra without light irradiation. The pristine-TiO_2 showed two well-separated sets of resonance lines. The high-field small peaks with an average g value of ~ 1.960 can be assigned to electrons trapped on Ti^{3+} centers; the low-field sharp features with an average g value of ~2.013, correspond to the holes trapped on O^- sites [74, 82]. These results indicate that the separation of photogenerated electrons and holes was more efficient in pristine-TiO_2 than in H-TiO_2. On the other hand, the intensity of O^- signals was significantly decreased for H-TiO_2, and an inverted broad resonance was observed at an average g value of ~ 1.957. This implies that decreasing the amount of Ti^{3+} species in the light-irradiated H-TiO_2 may derive from the combination of the photo-generated holes and the localized bulk Ti^{3+} species. These results suggest that bulk Ti^{3+} species tend to act as charge carrier traps where most of photo-generated holes were consumed through recombination with electrons [21, 66, 79]. According to the literature, non-radiative recombination releasing phonons is a major pathway for the annihilation of photo-generated charges in the semiconductor with high concentration of deep level defects, and the energy is exchanged in the form of lattice vibration and the thermal energy in materials is increased in this

process [88]. Hence, the photothermal effect of H-TiO_2 can be attributed to its dramatically enhanced non-radiative recombination by deep level defects (Ti^{3+} species) which have also been observed in our previous work [63].

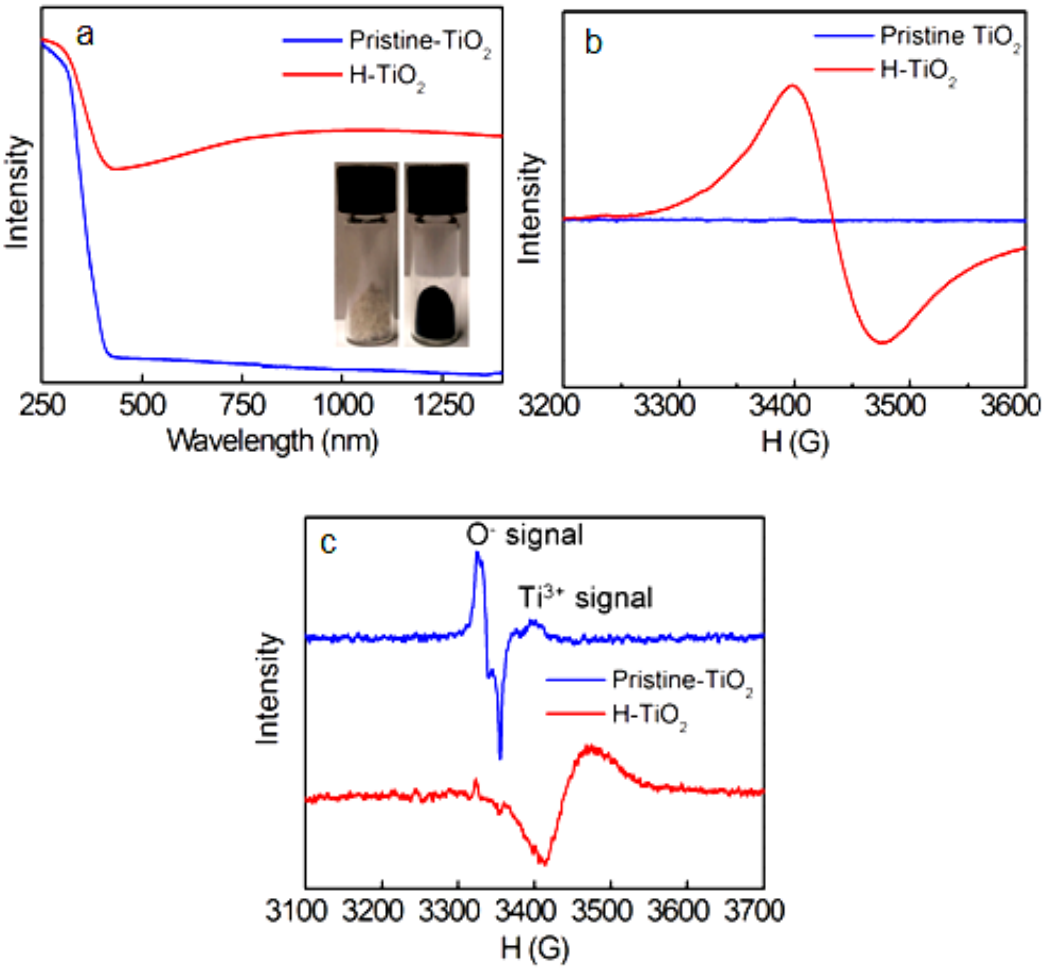

Figure 5-1. (a) UV-Vis-NIR absorption spectra, (b) EPR spectra and (c) light-induced EPR spectra of the pristine- and H-TiO_2 NPs. The inserted pictures show the pristine- and H-TiO_2 NPs samples.

5.2.2 Photothermal conversion efficiency of black H-TiO_2

Based on the dramatic absorption of NIR and clarified principle of photothermal effect, H-TiO_2 was used as photothermal agent in the following research. To enhance the stability of H-TiO_2 in aqueous solutions, the nanoparticles were coated by PEG to form H-TiO_2-PEG. As shown in Figure 5-2 and 5-3, dispersion of H-TiO_2 in water was increased after PEG coating.

Zeta potentials of H-TiO_2 and H-TiO_2-PEG were (-13.4±3.88) and (-15±4.46) mV respectively (Figure 5-4) and were not significantly different. Those results demonstrated PEG coating could enhance the stability of H-TiO_2 in aqueous solutions. For further evaluation of the stability of H-TiO_2-PEG, the nanoparticles were dispersed in serum solution for 7 days. As shown in Figure 5-5, the size distribution of the nanoparticles did not show dramatic change during the period, which suggests H-TiO_2-PEG NPs are stable in serum solution, and can be used as a potential PTT agent for further study. As shown in Figure 5-6, the absorbance of H-TiO_2-PEG was 0.49 at 808 nm.

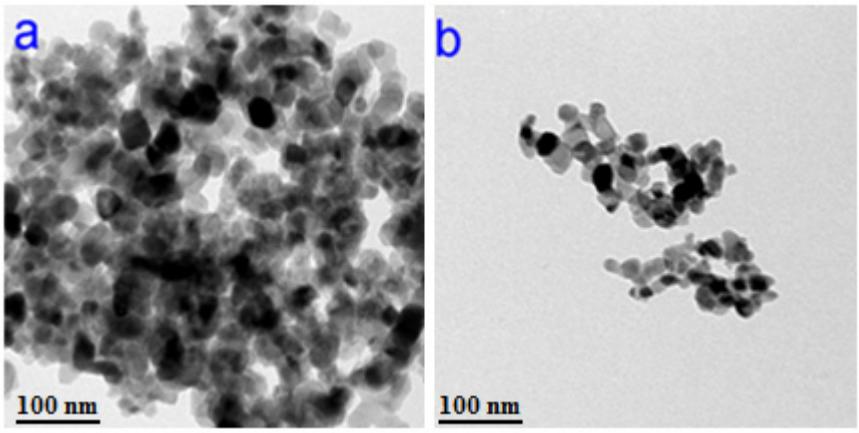

Figure 5-2. TEM of (a) H-TiO_2 and (b) H-TiO_2-PEG.

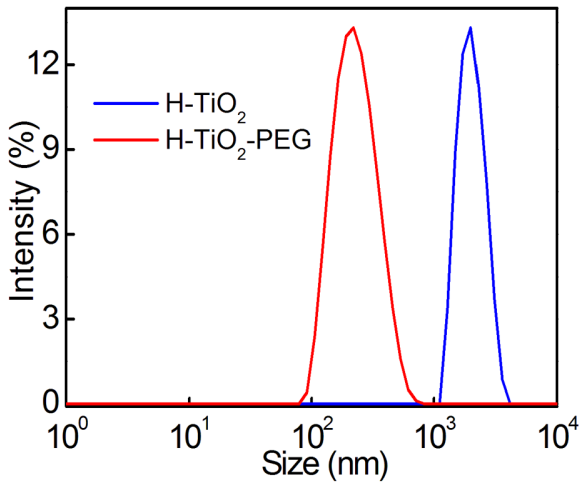

Figure 5-3. Size distribution of H-TiO_2 and H-TiO_2-PEG (100 μg·mL^{-1})

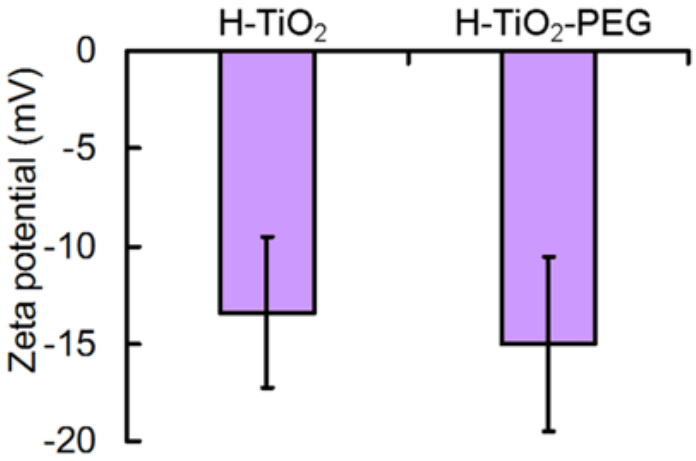

Figure 5-4. Zeta potential of H-TiO_2 and H-TiO_2-PEG.

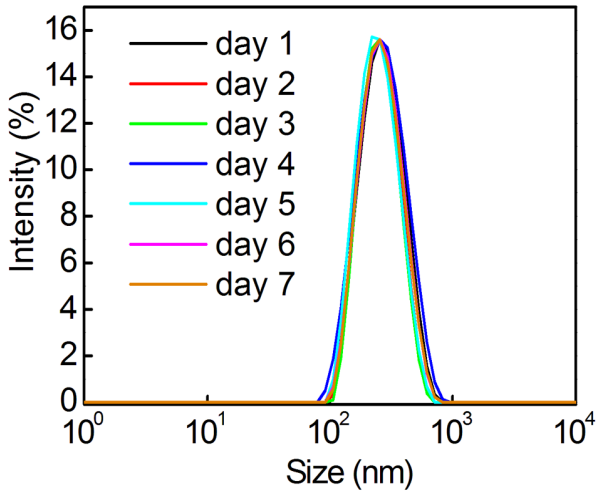

Figure 5-5. Size distribution of H-TiO_2-PEG NPs (100 μg·mL^{-1}) in serum solution.

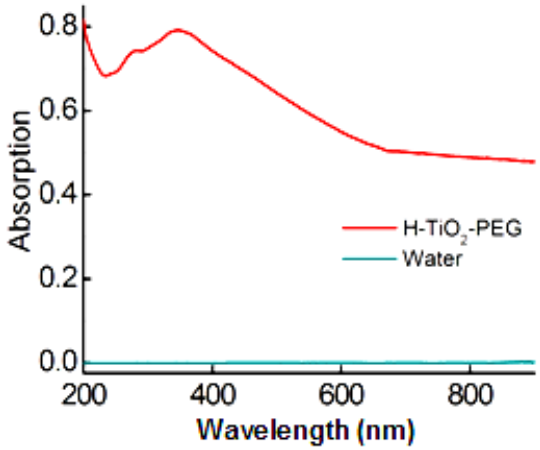

Figure 5-6. UV-Visble spectrua of H-TiO_2-PEG dispersed (100 μg·mL^{-1}) in water.

As a photothermal agent in PTT, photothermal conversion is a very important attribute. Consequently, the photothermal conversion performance of H-TiO_2-PEG NPs was evaluated. H-TiO_2-PEG was dispersed in water, and then irradiated with an 808 nm NIR laser at 2W·cm^{-2}. Pure water was used as a negative control. As shown in Figure 5-7a, the temperature of H-TiO_2-PEG increased rapidly with the NIR irradiation. After irradiation for 600 s, the temperature of H-TiO_2-PEG aqueous dispersions was 66 °C and there was a temperature increase of 44 °C. By comparison, the temperature of pure water was 28.5 °C and the increase was only 4.5 °C. It has been demonstrated that the cancer cells can be easily killed by exposure to temperatures over 50 °C for few minutes [106], and therefore H-TiO_2-PEG may be considered as a viable agent for photothermal therapy of cancer. After 600 s of irradiation, the NIR laser was shut off, and the decreased temperature was recorded for another 1140 s. The temperature change (ΔT) response to the NIR laser over a period of 1740 s is shown in Figure 5-7b. Linear time data versus -ln(θ) obtained from the cooling period of the NIR laser is shown in Figure 5-7c. The photothermal conversion efficiency (η) of H-TiO_2-PEG can be calculated according to the following equation [25, 118]:

$$\eta=\frac{hA(\Delta T_{max,mix}-\Delta T_{max,H_2O})}{I(1-10^{-A_\lambda})} \qquad (3)$$

where h is the heat transfer coefficient, A is the surface area of the container, where $\Delta T_{max,mix}$ and $\Delta T_{max,H_2O}$ are the temperature change of the H-TiO_2-PEG NPs dispersion and solvent (water) at the maximum steady-state temperature respectively, I is the laser power, A_λ is the absorbance of H-TiO_2-PEG NPs at 808 nm. According to the equation, η value of H-TiO_2-PEG was calculated to be about 40.8%, which was much higher than other reported PTT agents such as gold nanorods with 22% [25].

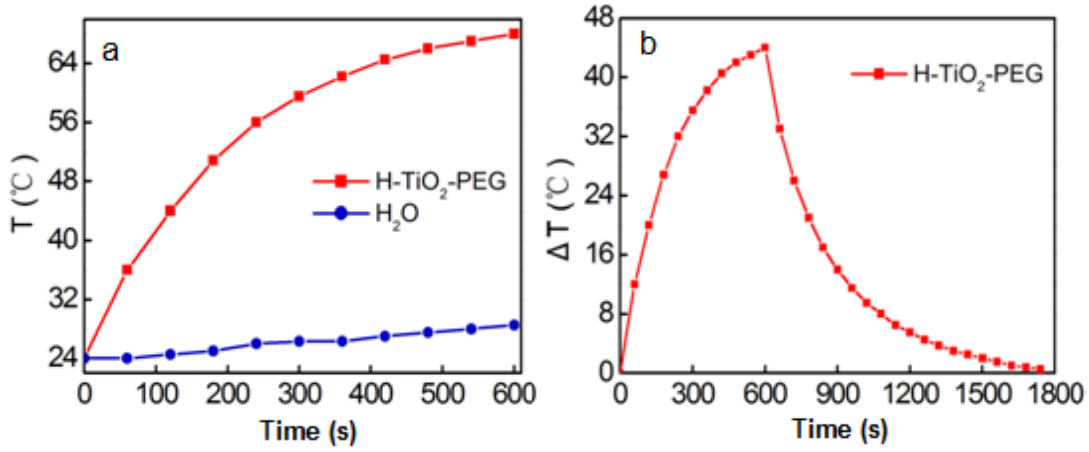

Figure 5-7. (a) Temperature evaluation of H-TiO_2-PEG NPs (100 μg·mL^{-1}) and pure water with 808 nm laser irradiation at 2 W·cm^{-2} for different times. (b) The temperature change (*ΔT*) responsed to NIR laser on and off in period of 2100 s.

5.2.3 Cytotoxicity and intracellular localization of black H-TiO_2 nanoparticles

It has been demonstrated that bare, white TiO_2 nanoparticles are environmentally friendly and exhibit low toxicity [89], however, there is still no report about the toxicity of H-TiO_2. Thus, cytotoxicity of H-TiO_2-PEG on both human and murine breast cancer cells was carried out through the MTT method. As shown in Figure 5-8a, MCF-7 or 4T1 cells were incubated with 50-300μg·mL^{-1} of H-TiO_2-PEG NPs 24h. The relative viability of the cancer cell was not decreased significantly, which suggests H-TiO_2-PEG NPs are also relatively nontoxic *in vitro*.

To investigate the uptake and distribution of H-TiO_2-PEG in cancer cells, fluorescent dye (alizarin red S, ARS) stained H-TiO_2-PEG were incubated with both MCF-7 and 4T1 cells for 2h. Free ARS incubated cells were used as negative control. FITC-phalloidine and Hoechst 33342 were used to label cell membrane (green fluorescence) and nucleus (blue fluorescence), respectively. As shown in Figure 5-8b, no red fluorescence was observed in free ARS incubated cells, which suggested free ARS could not be used to stain the cells. However, red fluorescence was observed in cytoplasm of cells treated by ARS stained H-TiO_2-PEG, which indicated that H-TiO_2-PEG could be uptaken by both MCF-7 and 4T1 cells. These results further

demonstrated that H-TiO_2-PEG NPs uptaken by cancer cells are relatively nontoxic *in vitro*.

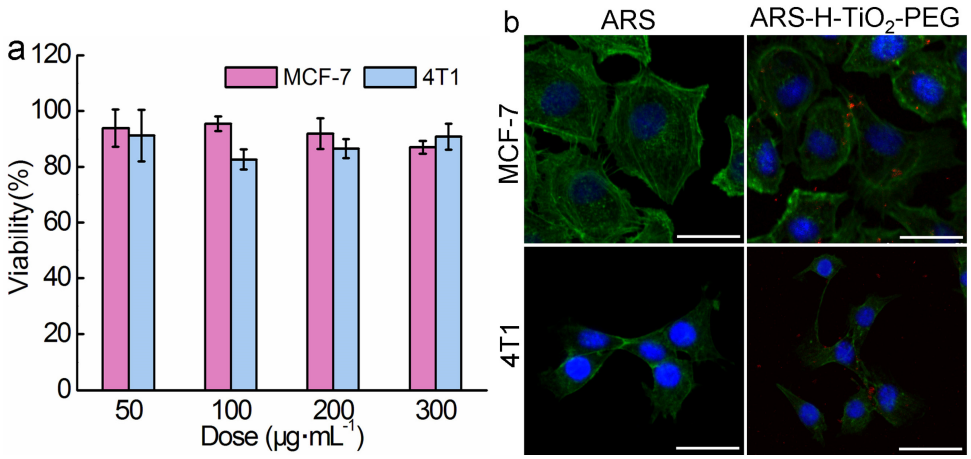

Figure 5-8. (a) Cell viability of MCF-7 and 4T1 cells after incubation with increased dose of H-TiO_2-PEG NPs for 24 h. (b) Intracellular localization of ARS stained 100 $\mu g \cdot mL^{-1}$ of H-TiO_2-PEG NPs (red fluorescence) in MCF-7 and 4T1 cells after 2 h incubation. FITC-phalloidine (green fluorescence) and Hoechst 33342 (blue fluorescence) are used to stain cell membrane and nuclei respectively. (Scale bar = 50 μm)

5.2.4 Photothermal therapeutic efficacy of H-TiO_2-PEG on cancer cells *in vitro*

Based on the high photothermal conversion efficiency, stability in serum solution, and low toxicity, the photothermal therapeutic efficacy of H-TiO_2-PEG was evaluated on cancer cells *in vitro*. MCF-7 and 4T1 cells were incubated with 100 $\mu g \cdot mL^{-1}$ of H-TiO_2-PEG for 2 h. The nanoparticles were then replaced by fresh DMEM, and the cells were irradiated with an 808 nm NIR laser at $2W \cdot cm^{-2}$ for various irradiation times, from 0-5 min. Cells incubated without H-TiO_2-PEG NPs were also irradiated by laser as a negative control. As shown in Figure 5-9a and 5-9b, neither control group of MCF-7 or 4T1 cells receiving only laser treatment (without using H-TiO_2-PEG), experienced any significant loss in viability after 5 min of irradiation. However, the viability of the cells incubated with H-TiO_2-PEG NPs decreased significantly with increasing irradiation time, and greater than 80% of both MCF-7 and 4T1 cells were killed upon 5 min of irradiation.

These results demonstrated H-TiO_2-PEG NPs is an effective PTT agent for cancer therapy *in vitro*.

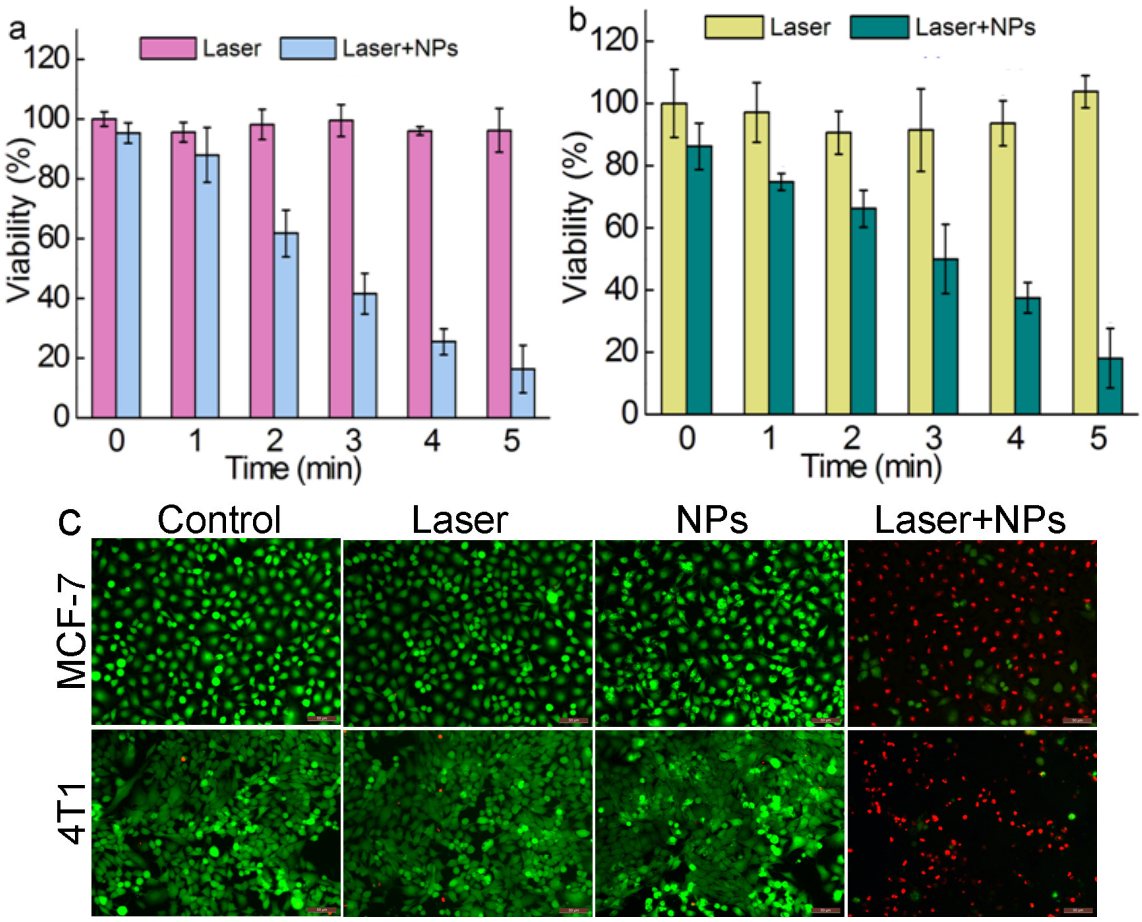

Figure 5-9. Viability of MCF-7 (a) and 4T1 (b) cells treated with or without 100 μg·mL^{-1} H-TiO_2-PEG NPs and 808 nm laser irradiation at 2W·cm^{-2} for ~5 min. (c) Microscope images of calceim AM (green, live cells) and propidium iodide (red, dead cells) co-stained MCF-7 or 4T1 cells treated with or without 100 μg·mL^{-1} H-TiO_2-PEG NPs and laser irradiation for 5 min. (Scale bar =5 0μm)

In addition, to further verify the PTT performance of H-TiO_2-PEG *in vitro*, the cells were stained with calcein AM and PI solutions, which can discern live or died cells through emitted green or red fluorescence respectively. MCF-7 and 4T1 cells were incubated with H-TiO_2-PEG for 2h; the nanoparticles were then replaced with fresh DMEM, and the cells were then irradiated with an 808 nm laser at 2 W·cm^{-2} for 5 min. Cells with normal culture (control), with nanoparticle incubation only (NPs only), and with laser irradiation only (laser only) were used as negative controls. As shown

in Figure 5-9c, the majority of control MCF-7 and 4T1 cells were alive (green). However, the majority cells in the NPs plus laser group were died (red), supporting the application of H-TiO_2-PEG as an effective *in vitro* PTT agent that may potentially be used for *in vivo* applications as well.

5.2.5 Toxicity and bio-distribution of H-TiO_2-PEG *in vivo*

As a potential *in vivo* PTT agent, the toxicity of H-TiO_2-PEG must be evaluated. In this study, histological analyses were used to evaluate the toxicity of the nanoparticles *in vivo*. Healthy Blab/c mice were injected with H-TiO_2-PEG, and saline injected mice were used as the control. Over one month period, mice behaviors such as eating, drinking, excretion, activity and neurological status were observed. There were notable differences in the above behaviors between control and H-TiO_2-PEG-injected groups. After one month, the mice were sacrificed, and the main organs including the heart, liver, spleen, kidney and lung were evaluated by histological analyses. As shown in Figure 5-10, there was no detectable tissue damage or other lesions such as necrosis, inflammatory, or pulmonary fibrosis when comparing the control with the H-TiO_2-PEG NP group. The results suggested that H-TiO_2-PEG was nontoxic to mice at the injected dose. However, more effort is still required to systematically evaluate the potential short- and long-term toxicity of H-TiO_2-PEG NPs at various doses *in vivo*.

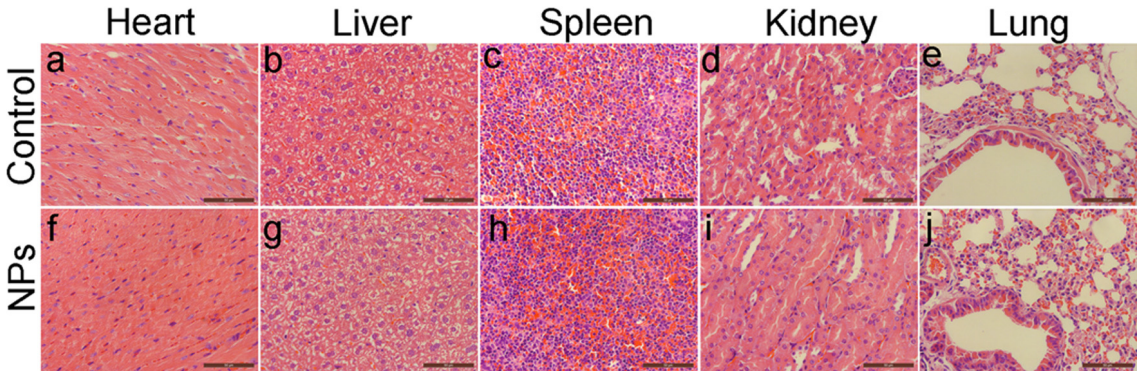

Figure 5-10. Histological analysis of main organs from the mice intravenously injected with 200 μL of H-TiO_2-PEG (200 μg·mL^{-1}). Mice injected with the same volume of saline are used as the control.

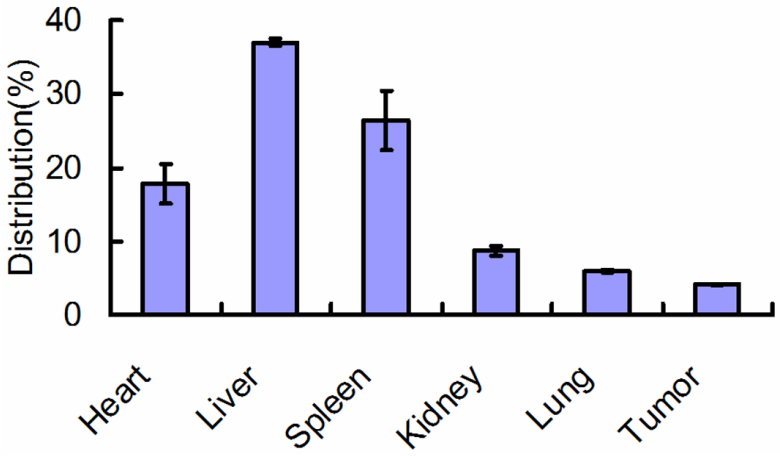

Figure 5-11. Distribution of H-TiO_2-PEG in major organs of mice after injected with 200 μL of H-TiO_2-PEG (200 μg·mL^{-1}) for 24 h.

To investigate the bio-distribution of H-TiO_2-PEG, healthy mice were intravenously injected with H-TiO_2-PEG. The mice were sacrificed after 24 h, and the content of Ti in main organs were measured by ICP-MS. As shown in Supplementary Figure 5-11, nearly 63.4% of the total H-TiO_2-PEG injected was distributed in liver and spleen, which were in accordance with other reported nanomaterials [112].

5.2.6 Photothermal therapy *in vivo* by using of H-TiO_2-PEG agent

The *in vivo* photothermal therapy of H-TiO_2-PEG was carried out on 4T1 tumor bearing Blab/c mice. When the tumors grew to 3 - 4mm in diameter, the mice were divided into 4 groups. Mice were intra-tumorally injected with 100 μL of H-TiO_2-PEG aqueous dispersion (100 μg·mL^{-1}) and irradiated with an 808 nm laser (Laser+NPs). The mice receiving only laser irradiation (Laser only), only H-TiO_2-PEG injection (NPs only), or neither H-TiO_2-PEG injection nor laser irradiation (Control) were used as negative controls. As shown in Figure 5-12a and 3-12d, the tumors grew consistently in all control groups. The relative tumor volume (V/V_O) on day 14 reached (12.3±2.4) in the double negative control group, (13.7±2.8) in the NPs only group, and (14.2±3.6) in the laser only group. These results demonstrated that laser irradiation alone or H-TiO_2-PEG NPs injection alone didn't affect tumor development. However, upon irradiation of the NPs + laser group with 808

nm laser, edemas appeared on the tumors within three days due to thermal damage. By the fifth day, the tumors shrank, and black scars were left on the tumor site. By the 14th day, the tumors disappeared, leaving only left smooth scars on the original tumor sites. These results suggest that H-TiO_2-PEG NPs are an effective PTT agent for *in vivo* cancer therapy.

Change of body weight is an important parameter to measure for the evaluation toxicity or cellular damage during treatment. Consequently, the body weight of mice was recorded during the therapy period. As shown in Figure 5-12b, in the first 3 days, body weight of mice decreased slightly in the NPs only group, laser only group, and NPs + laser group, but increased slightly in control group. This is likely due to the fact that the mice were anesthetized during this period of time, which negatively affected the amount of food consumed and decreased body weight slightly. However, mice in the double negative control group weren't anesthetized so their body weight increased. From 4th to 14th day, body weight of all mice was increased, which demonstrated that the PTT agent and treatment used in this study were nontoxic and safe. However, body weight in NPs + laser group was significantly less than other 3 groups after the 4th day, due to tumor shrinkage as measured by reduction in tumor volume.

To further evaluate the PTT performance of H-TiO_2-PEG, survival of the mice after treatment was also recorded. As shown in Figure 5-12c, mice in NPs + laser group lived healthily for more than 50 days. However, some mice in the other 3 groups died from days 25-34, and all of the mice in these groups died after day 47. These results demonstrated that H-TiO_2-PEG NPs are high-performance PTT agents and are promising for further biomedical application.

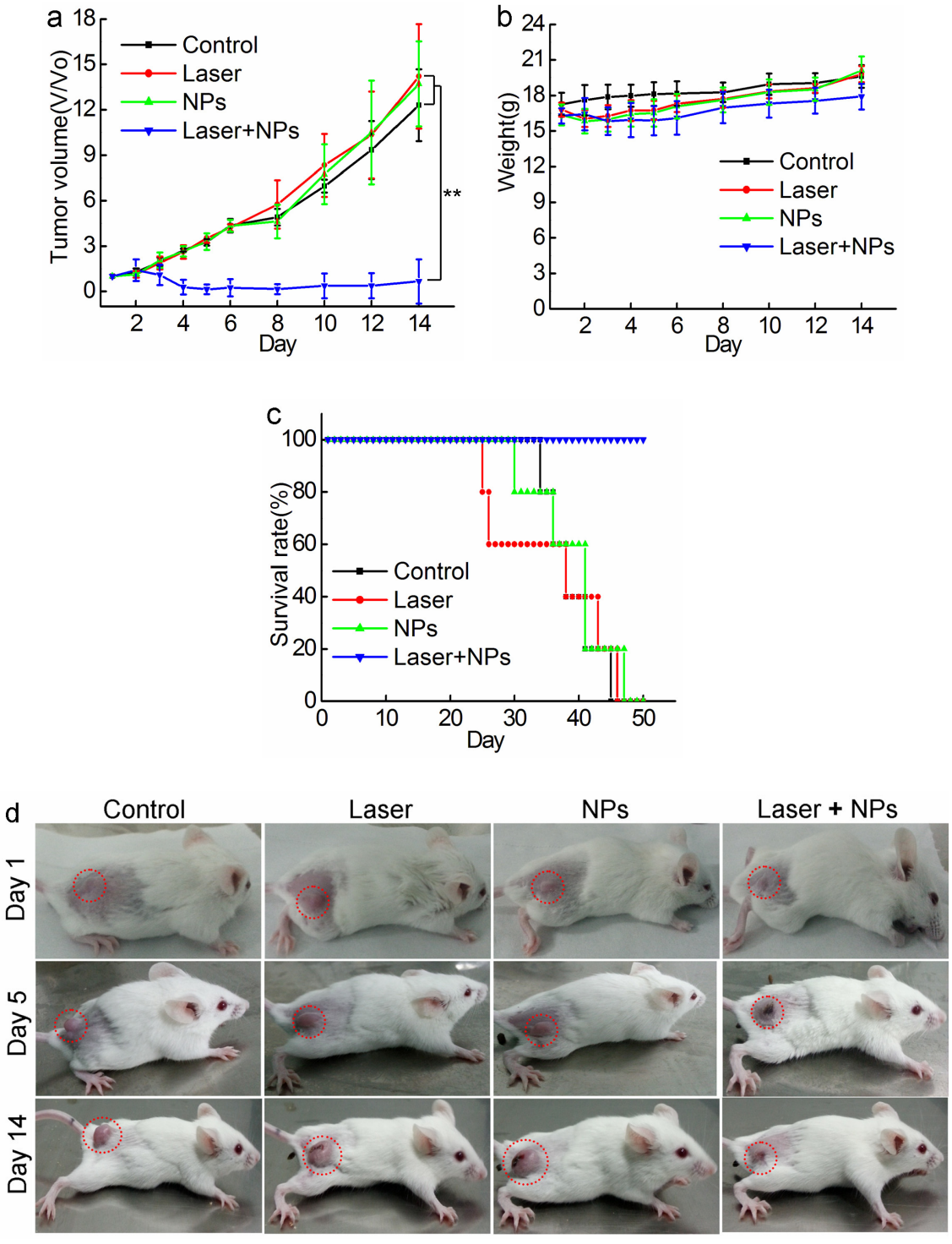

Figure 5-12. (a) The relative tumor volume, (b) body weight and (c) survival rate of the 4T1 tumor-bearing mice after given an intra-tumor injection with or without 100 μL of H-TiO_2-PEG aqueous dispersion (100 μg·mL^{-1}), then irradiated with or without an 808 nm NIR laser at 2 W·cm^{-2} for 5 min. (d) Photos of 4T1 tumor-bearing mice at day 1, 5 and 14 after different treatments described above.

5.3 Conclusion

H-TiO_2 nanoparticles were explored as a new NIR triggered photothermal agent. We have demonstrated the photothermal effect of H-TiO_2 can be attributed to its dramatically enhanced non-radiative recombination, which led to the thermal energy increasing in H-TiO_2. Our results suggest that H-TiO_2 coated by PEG possess several features: (1) high NIR photothermal effect, (2) low toxicity and good biocompatibility, (3) low cost and facile synthetic method. More importantly, H-TiO_2-PEG was successfully used as photothermal agent for NIR triggered cancer therapy both *in vitro* and *in vivo*. This work also provides an experimental basis for the promising application of H-TiO_2-PEG as a highly effective photothermal agent for cancer therapy that exhibits low toxicity. It is demonstrated that NIR triggered cancer photothermal therapy of H-TiO_2 can advance applications of TiO_2 in biomedicine in future

6. Fabrication of N-doped TiO_2 coatings on nanoporous Si nanopillar arrays through biomimetic mineralization

6.1 State of the art

TiO_2 has attracted much attention due to its unique properties and many promising applications in environmental and energy areas [5]. However, the limited solar absorption and electrochemical activity caused by its poor electric conductivity and large bandgap is substantially lower than practically required [23, 103]. For improving the electric conductivity of TiO_2, its combination with conducting agents, such as metals, metal oxides, and carbonaceous materials has proven to be a common strategy to enhance electron transport [16]; on the other hand, fabrication of TiO_2 with a specific morphology (e.g. high-aspect-ratio or nanoporous structure) is a promising pathway to modify the separation and transportation of charge carriers in TiO_2 [13]. For improving the solar absorption of TiO_2, N-doping and sensitization with low bandgap semiconductors are considered as effective routes, which could improve the photocatalytic activity of TiO_2 by increasing its optical absorption coefficient and wavelength range [10, 120, 121].

As a low bandgap semiconductor, silicon (Si, E_g=1.12 eV) can absorb sunlight efficiently, and furthermore, highly doped Si has excellent conductivity ($\rho < 0.005\ \Omega\cdot cm$). However, it is difficult to simply use Si in photo- or electrochemical application due to its high valence band maximum energy and poor chemical stability in electrolytes [122]. Therefore, a composite structure, Si coated with a stable semiconductor (e.g. TiO_2), has been proposed to compensate these shortcomings [123]. Nevertheless, the synthesis of nanostructured TiO_2 with N-doping normally require harsh conditions (NH_3 atmosphere, acids and bases, or organic solvents, etc.), which will degrade the material properties of Si [120]. Therefore, N-doping, morphology modification, and sensitization of TiO_2 with Si are not easy to achieve simultaneously, and the investigations in synergistic effects of them are limited. Hence, devising a process for preparing N-doped TiO_2 with controlled morphology under relatively mild conditions is desirable.

Inspired by natural mineralization mechanisms, biomimetic mineralization has been recognized to offer a environmental benign and energy efficient route for TiO_2 synthesis [124]. In this process, using peptides or its derivatives as catalytic molecules, micro- and nanostructured TiO_2 will be obtained under mild conditions [125, 126]. Additionally, the morphology of the product could be controlled by the use of different templates such as $CaCO_3$ microparticles [127], 3D diatom frustules [128], anodized aluminum oxide templates [129], silica spheres [130], N-doped carbon nanotube [131], silk fiber [132], peptide nanofibers [133], graphene nanosheets [134], and nickel foam [135]. Moreover, recently-developed layer by layer mineralization process provide a versatile method for the formation of multilayer peptide/TiO_2 hybrid materials on templates [127-130, 134, 135]; and some studies have demonstrated that N-doped TiO_2 could be synthesized easily by sintering of peptide/TiO_2 composites [133].

In this work, nanoporous Si nanopillar arrays fabricated by a combination of nanoimprint lithography and metal-assisted chemical etching are used as template [28], and alternatively immersed into aqueous protamine (PA) and titanium bis(ammonium lactato)-dihydroxide (Ti-BALDH) solution: positively charged protamine moleculars are adsorbed on the Si nanopillars through capillary effect and electrostatic attraction, and subsequently induce the hydrolysis and condensation of Ti-BALDH to form the negatively charged TiO_2, which enable layer by layer (LBL) deposition of protamine/TiO_2 hybrid materials on the surface of the Si nanopillars. After calcination, N-doped TiO_2/Si core/shell nanopillar arrays with nanoporous structure are obtained, which shows significantly improved solar absorption. Moreover, the thickness of the N-doped TiO_2 layer could be controlled by varying the cycles of deposition. The obtained TiO_2/Si core/shell nanopillars might have potential applications in photocatalysis, and this study may pave the way for the further controlled synthesis of TiO_2/Si nanocomposites through biomimetic mineralization.

6.2 Results and Discussions

The method of protamine-mediated layer by layer titania mineralization is based on previously reported works [127-130, 134, 135]. Protamine (PA) is a kind of cationic protein extracted from sperm nuclei, which can induce the formation of a titania/protamine nanocomposite from a water-stable titania precursor (Ti-BALDH) [127]. In the presented experiment, the nanoporous Si nanopillar arrays used as template have negatively charged surface due to the existence of Si-O-bearing (~ 1 nm) when it was exposed to air for several minutes [28]. This template is alternatively immersed into aqueous solutions of catalytic molecules (PA) and the titania precursor (Ti-BALDH) for the layer by layer fabrication of PA/TiO_2 coating (Scheme 6-1).

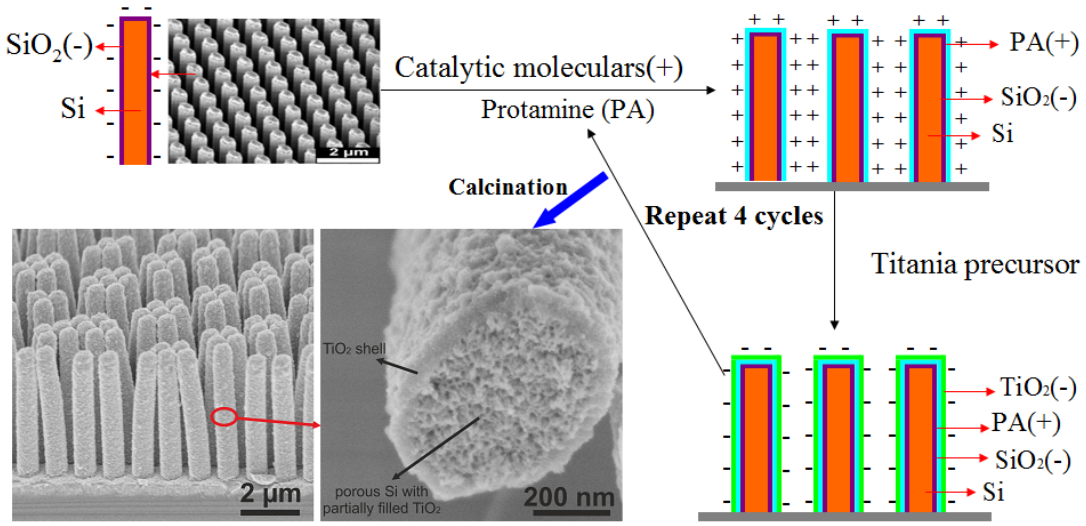

Scheme 6-1. Schematic illustration of the biomimetic layer-by-layer (LBL) TiO_2 mineralization on nanoporous Si nanopillar arrays.

The polycationic PA molecules bind to the negatively charged Si surface and induce the formation of TiO_2 layer from the Ti-BALDH precursor. This ability of PA to bind to the Si as well as to the TiO_2 surfaces, enabled the layer by layer (LBL) fabrication of PA/TiO_2 nanocomposite coating on the Si nanopillars. Zeta potential analysis was used to characterize the surface charge of Si nanopillars at every step during the first four cycles of this LBL TiO_2 deposition process; an oscillation for zeta potentials measurement after each alternative deposition of the PA and TiO_2 was observed (Figure 6-1),

which is consistent with the presence of positively charged PA molecules or of negatively charged TiO_2, respectively.

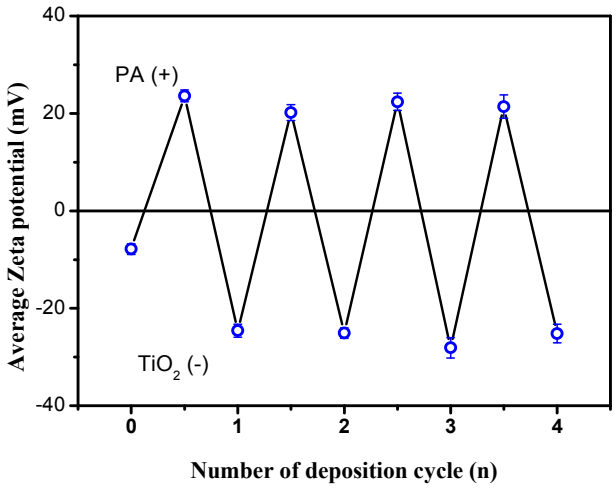

Figure 6-1. Zeta-potential measurements of nanoporous Si nanopillars after each deposition step. The first measurement (layer 0) is the surface potential of the starting nanoporous Si nanopillar templates. (PA (+): Protamine molecules with positive charge; TiO_2 (-):TiO_2 induced by protamine with negative charge.)

In order to remove the adsorbed water, to pyrolyze the organic molecules, and to crystallize the TiO_2, the PA/TiO_2 coated Si nanopillars are calcinated at 500 °C in Ar for 3 h. Figure 6-2 shows the XRD patterns of PA/TiO_2 coated Si nanopillars before and after calcination. The original TiO_2 on Si nanopillars displays an amorphous structure, no peaks are observed between 20-60°; while it shows four peaks at 2θ = 25.3°, 33.1°, 37.8°, and 48.1° after calcination, which demonstrate the formation of the anatase phase (JCPDS card no. 21−1272, black line). The calculated average crystallite sizes (using the Scherrer equation [40]) of TiO_2 in the (101) direction is 6 nm.

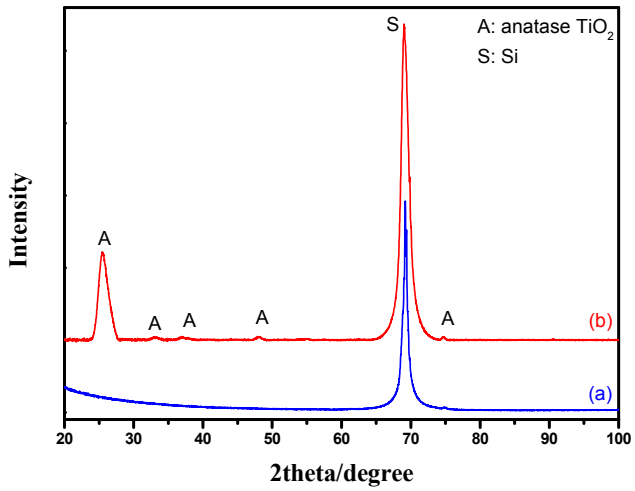

Figure 6-2. XRD patterns of the PA/TiO_2 coated Si nanopillars via exposure to 4 LBL deposition cycles before (a) and after calcination (b).

Figure 6-3a and b show an overview SEM image of the fabricated nanoporous Si nanopillars. The distance between two adjacent pillars (periodicity) is 1.0 μm, and the pillar height is about 5.2 μm; moreover, the pillars are elliptical with major and minor diameters of 613 nm and 385 nm, respectively. Figure 6-3c shows the magnified images of the cross-section of the pillars, which demonstrated the existence of a three dimensional porous structure, and its pore size is about 10 nm. Figure 6-3d and f show the TiO_2 coated Si nanopillars via exposure to 4 deposition cycles after calcination. A uniform TiO_2 coating with a thickness of 45 nm - 55 nm was observed on the surface of the Si pillars, which were comprised of numerous tiny nanoparticles (<10 nm). In addition, the pore size in the bulk of Si pillars was obviously decreased, due to the filling of TiO_2 (Figure 6-3f). Interestingly, more TiO_2 was filled close to the surface rather than in the center of the nanoporous pillars. An explanation for this might be that the initial deposition of TiO_2 at the surface hindered the further diffusion of PA and Ti-BALDH into the center of the pillars, leading to the lower deposition amount in the center. EDS element mapping of the TiO_2 coated Si nanopillars exhibits the presence of Ti, O, Si, N, and C species (Figure 6-4). The existence of N and C species is derived from the organic pyrolysis during calcination. The XPS N 1*s* spectrum of this sample showed two nitrogen features: the peak with a higher binding energy centered at 401.4 eV can be assigned to nitrogen in the form of a Ti–N–O linkage [136], and the

peak with a lower binding energy located at 397.4 eV can be attributed to the nitrogen atom replacing the oxygen atoms in the TiO_2 crystal lattice with the formation of an N–Ti–N bond (Figure 6-5) [137]. These results demonstrate that nitrogen atoms of the protamine are introduced into the TiO_2 structure as the doped element, and the decomposition of its molecular chains forms small amounts of amorphous carbon in the TiO_2 [133]. It should be noted that the distribution of Ti is wider than that of Si, indicating the structure of the Si core and TiO_2 shell. Figure 6-6 exhibits the EDS spectrum of this sample, and a quantitative calculation demonstrates that the atomic ratio of Ti/Si is close to 1 for both points and area analysis, indicating that the TiO_2 deposition through biomimetic LBL mineralization is uniform. However, the content of Ti slightly increases from position A to C (from bottom to top) for TiO_2 coated Si nanopillars. This result might be induced by the lower concentration of PA and Ti-BALDH in the bottom of the Si pillars, because the PA and Ti-BALDH molecules will be partially consumed by the adsorption or reaction in the diffusion process from the top to the bottom.

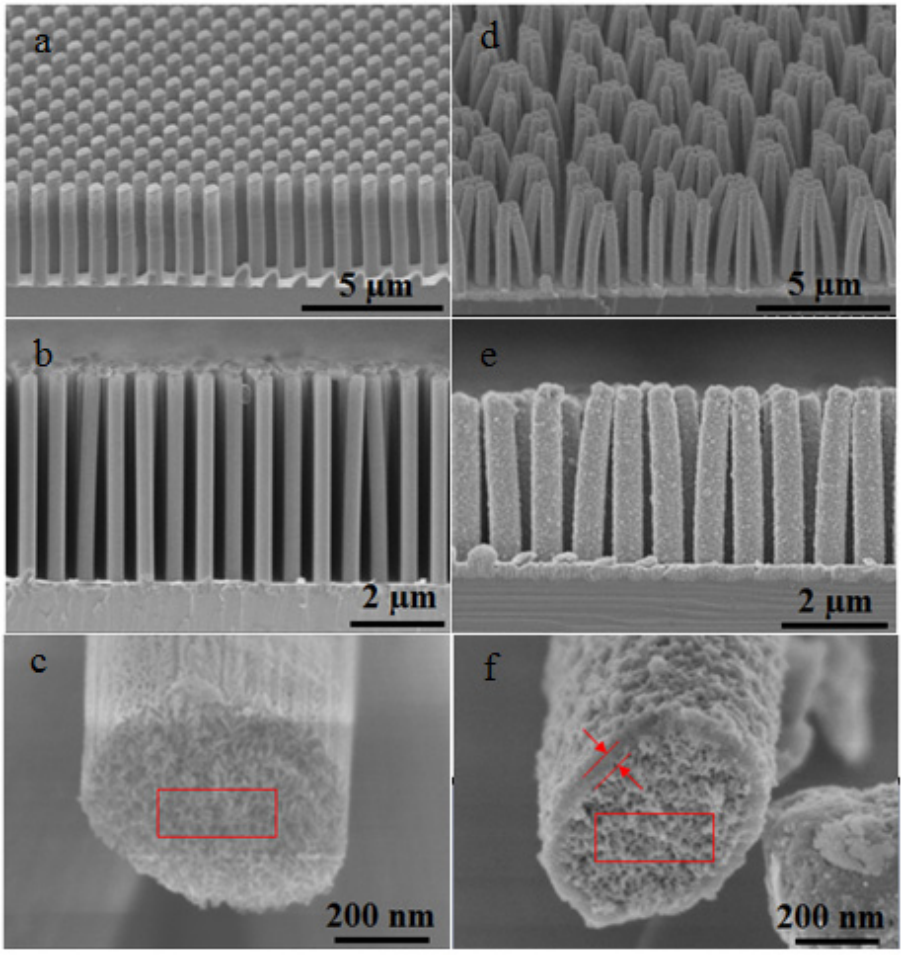

Figure 6-3. SEM images of the fabricated Si nanopillars template and the TiO_2 coated Si nanopillars via exposure to 4 LBL deposition cycles after calcination: (a) overview of Si nanopillars; (b) side wall of Si nanopillars; (c) cross-section of Si nanopillars; (d) overview of TiO_2 coated Si nanopillars; (e) side wall of TiO_2 coated Si nanopillars; (f) cross-section of TiO_2 coated Si nanopillars.

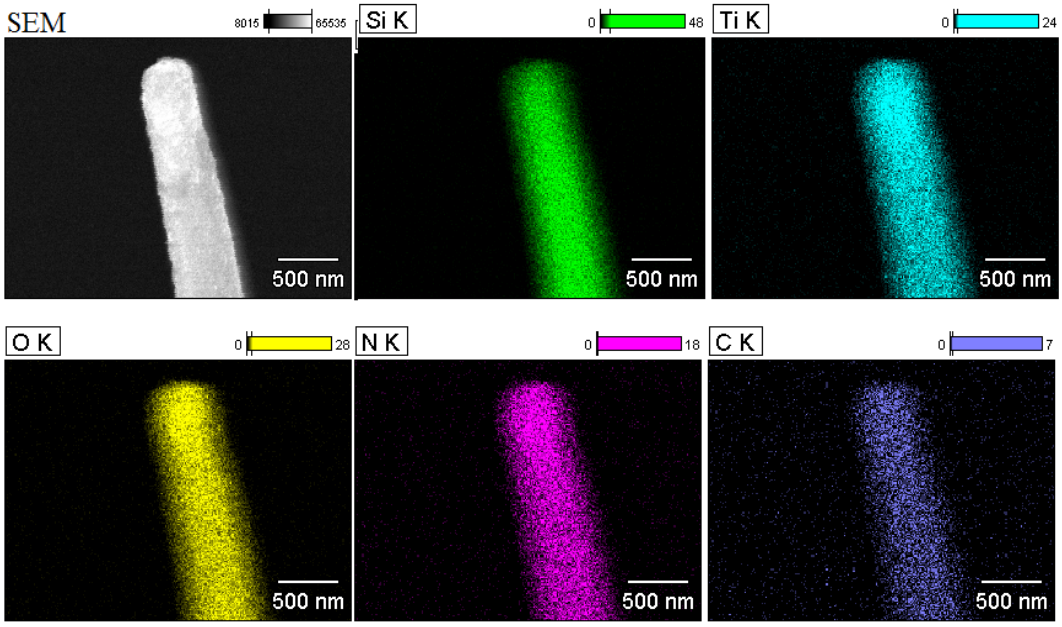

Figure 6-4. EDS element mapping images of the TiO_2 coated Si nanopillars via exposure to 4 LBL deposition cycles after calcination (as shown in Figure 6-3).

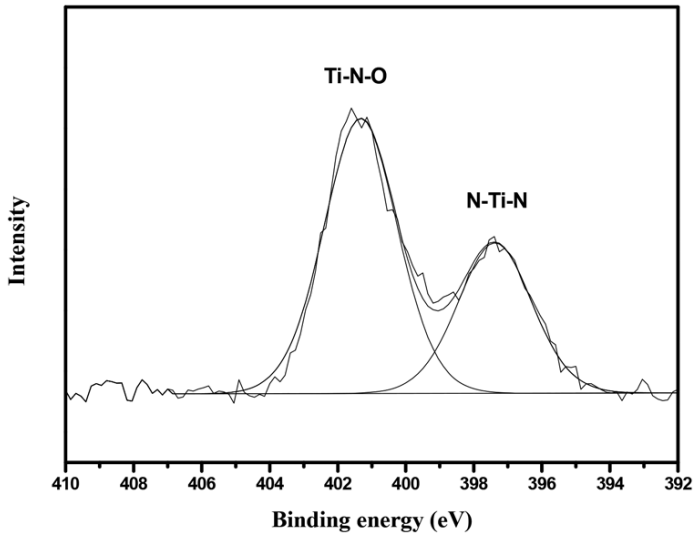

Figure 6-5. N 1*s* XPS spectra of the TiO_2 coated Si nanopillars via exposure to 4 LBL deposition cycles after calcination.

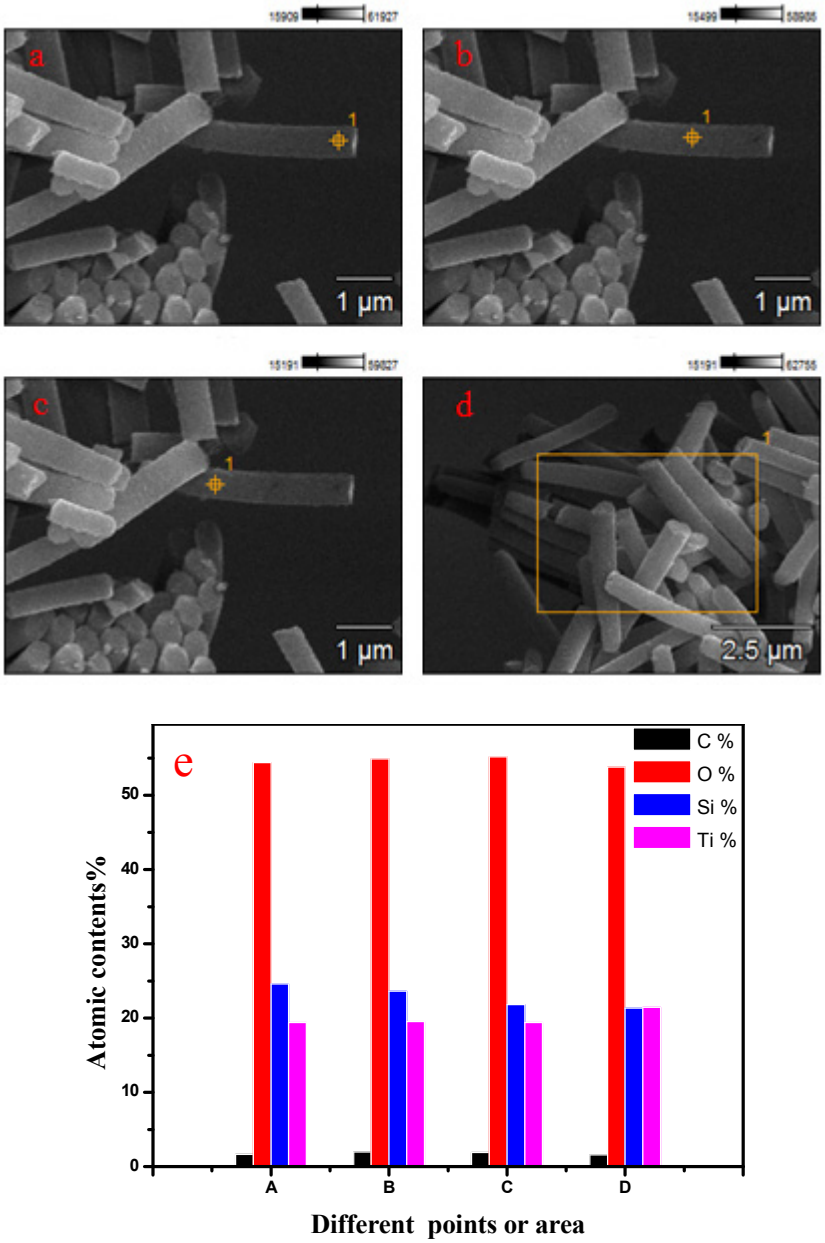

Figure 6-6. EDS analysis of TiO_2 coated Si nanopillars via exposure to 4 LBL deposition cycles after calcination: (a-c) SEM images of the positions of the EDS measurements in point A, B, and C; (d) EDS spectrum for area D; (e) atomic contents of the sample from different points or area analysis.

To allow a deeper understanding the formation of the TiO_2 coating, Si nanopillars coated with different cycles of deposition after calcination are characterized. After 1 cycle deposition, a TiO_2 shell with a thickness of 10-15 nm is formed, and the porous structure on the surface of the nanopillars still

remained. The filling of the porous pillar interiors is limited as the pore size in the cross-section is similar as initial (Figure 6-7a and d). After 4 cycles of deposition, the thickness of the TiO_2 shell is increased into 45-55 nm, and porous structure on the surface of the nanopillar was almost fully covered by TiO_2 layer. Moreover, the TiO_2 also clearly exist in the center of the nanopillars with the decreasing pore size in the cross-section (Figure 6-7b and e). The thickness of the TiO_2 shell is further increased into 70-80 nm after 8 cycles of deposition, and the surface of the nanopillars becomes very rough with the appearance of numerous TiO_2 nanoparticles, in addition, the interior of the pillars seems to be completely filled with TiO_2 (Figure 6-7c and f).

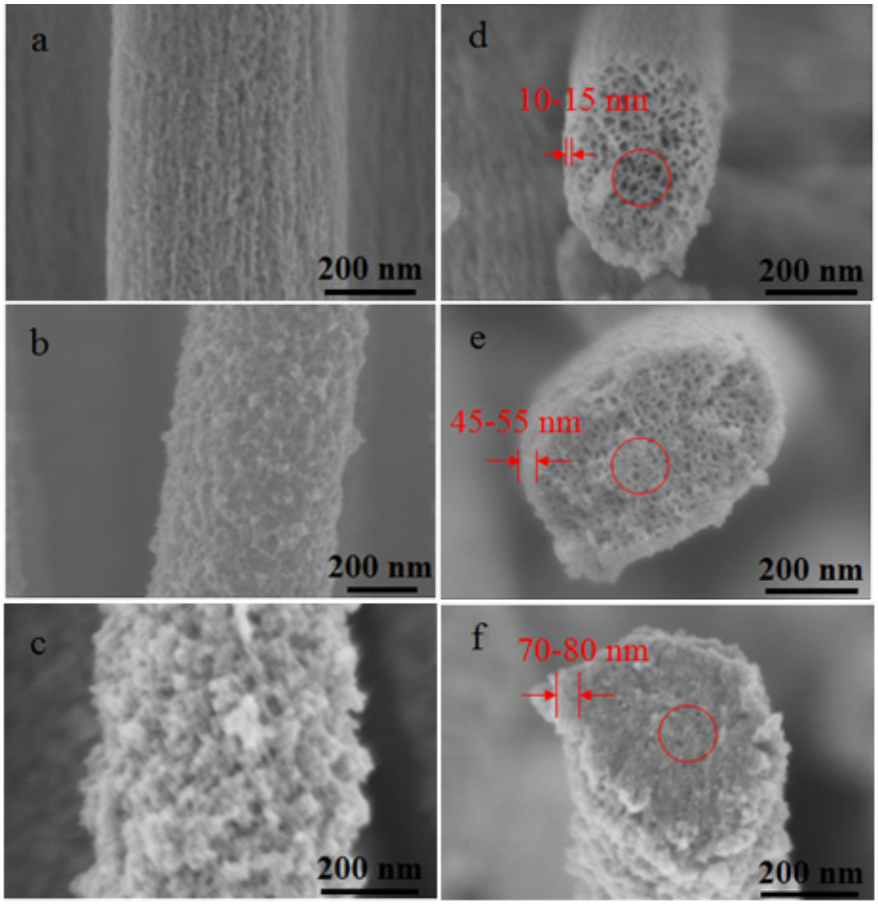

Figure 6-7. SEM images of TiO_2 coated Si nanopillars via exposure to different LBL deposition cycles after calcination: side wall of Si nanopillars with (a) 1 cycle of deposition; (b) 4 cycles of deposition; (c) 8 cycles of deposition; cross-section of Si nanopillars with (d) 1 cycle of deposition; (e) 4 cycles of deposition; (f) 8 cycles of deposition.

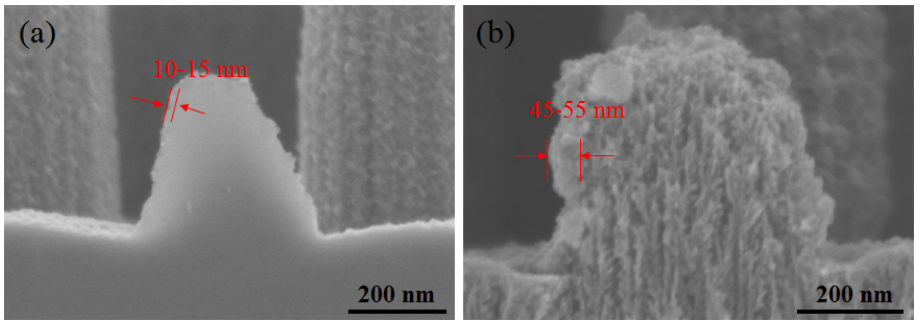

Figure 6-8. SEM images of TiO_2 coating on solid (a) and nanoporous (b) Si nanopillars via exposure to 4 LBL deposition cycles after calcination: (a) cross-section in the bottom of TiO_2 coated solid Si nanopillars; (b) cross-section in the bottom of TiO_2 coated nanoporous Si nanopillars.

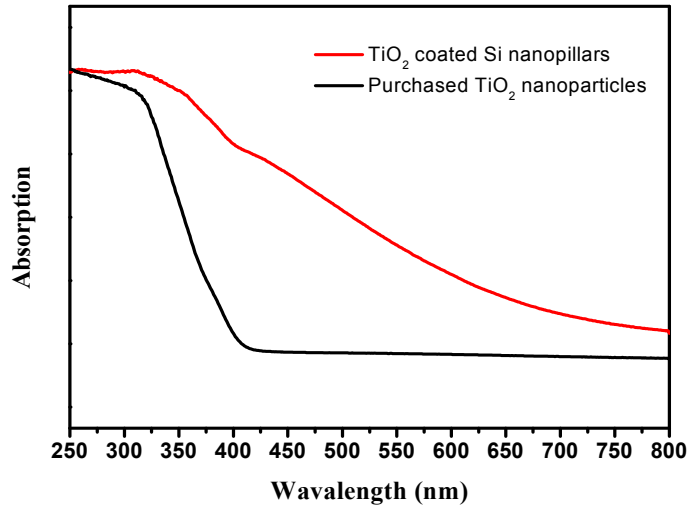

Figure 6-9. UV-vis absorption spectra of purchased TiO_2 nanoparticles (Degussa P25) and TiO_2 coated Si nanopillars via exposure to 4 LBL deposition cycles after calcination.

Compared with other reports, it is observed that biomimetic LBL TiO_2 deposition on nanoporous Si nanopillars is more efficient than that of other templates [135-137]. The ability of the catalytic molecules to bind to both the templates and the TiO_2 through electrostatic attraction are considered as the key factor for this process. The experimental results indicate that the porous structure of the used Si nanopillars also strongly affects the formation of the TiO_2 layer. For comparison, solid Si nanopillars (no pores) [28] are used in an identical TiO_2 deposition process. The thickness of the formed TiO_2 shell is only 10-15 nm after 4 cycles, which is much thinner than that of

nanoporous Si nanopillars (Figure 6-8). An explanation might be that the nanoporous structure can enhance the adsorption of PA and Ti-BALDH through the much higher surface area and capillary effects, which induces more TiO_2 formation in both surface and interiors of the Si nanopillars.

Figure 6-9 shows the UV-vis absorption spectra of purchased TiO_2 nanoparticles (Degussa P25) in comparison with the presented TiO_2 coated Si nanopillars (4 LBL deposition cycles after calcination). P25 shows a steep increase in absorption at wavelengths of 400 nm due to the intrinsic bandgap of crystalline anatase TiO_2. Compared with P25, the TiO_2 coated Si nanopillars show a significantly enhanced absorption in the region of visible light, which can be attributed to the synergistic effect between N doping and Si sensitization.

6.3 Conclusion

In summary, N-doped TiO_2/Si core/shell nanopillar arrays with a nanoporous structure are produced through a protamine-mediated layer-by-layer TiO_2 mineralization. The thickness of the N-doped TiO_2 layer can be controlled by varying the cycles of deposition, and the experimental results demonstrate that the nanoporous structure of the Si nanopillars strongly affects and enhances the formation of the TiO_2 layer. The obtained TiO_2/Si nanocomposites show significantly improved solar adsorption. As a consequence, the obtained TiO_2/Si core/shell nanopillars might have potential applications in photocatalysis. This study may pave the way for the further controlled synthesis of TiO_2/Si nanocomposites through biomimetic mineralization.

7. Summary and Perspective

Hydrogenated TiO_2 (H-TiO_2) with distinct physical and chemical properties are synthesized through hydrogen (H_2) plasma treatment, which exhibit excellent performance in the application for lithium ion batteries, photocatalysis, and photothermal conversion. Moreover, the microstructure of H-TiO_2, and their dependence on the application performance of H-TiO_2 are comprehensively investigated. It is believed that this research might provide new insights into synthesis, properties, and applications of H-TiO_2, which is highly favorable for the development of high-performance and versatile TiO_2 materials for energy storage and conversion devices.

(1) Hydrogenated anatase TiO_2 nanoparticles with significantly improved fast lithlium storage performance are synthesized through a high-temperature H_2 plasma treatment. Systematic electrochemical analysis revealed that the improved rate capability of H-TiO_2 results from the enhanced contribution of pseudocapacitive lithium storage on the particle surface. It is suggested the disordered surface layers and Ti^{3+} species of H-TiO_2 play an important role in the improvement of pseudocapacitive lithium storage. The result help to understand the fast lithium storage performance for H-TiO_2, and might pave the way for further studies of other hydrogenated metal oxide electrodes for high power LIBs.

(2) H-TiO_2 with different hydrogenation degrees are rapidly synthesized through high power H_2 plasma treatment in several minutes; and their photocatalytic activity are evaluated by methylene blue (MB) degradation and CO_2 reduction in aqueous and gaseous media, respectively. The slightly hydrogenated TiO_2 (s-H-TiO_2) with the original white color exhibit the enhanced photoactivity compared with the pristine TiO_2; while the grey or black H-TiO_2 with higher hydrogenation degrees (h-H-TiO_2) display much worse catalytic performances. Further investigations reveal that the higher ratio of trapped holes (O^- centers) and lower recombination rate induced by the increasing of surface defects might be the critical factors for the high

activity of s-H-TiO_2; on the contrary, h-H-TiO_2 possess high concentration of bulk defects, leading to the significantly decreased amount of O^- centers and enhanced nonradiative recombination, which strongly inhibit their photoactivity. These results might provide new insights into the photoactivity of H-TiO_2, and pave the way for further studies of other hydrogenated metal oxides for photocatalytic applications.

(3) Hydrogenated black TiO_2 with large infrared absorption is explored as photothermal agent for cancer photothermal therapy due to its dramatically enhanced nonradiative recombination. After PEG coating, H-TiO_2-PEG exhibite high photothermal conversion efficiency of 40.8%, and stable size distribution in serum solution. The therapy effect of H-TiO_2-PEG demonstrates that this material is low toxicity, and can effectively kill MCF07, 4T1 tumor cells (a kind of transplantable tumor cells from human breast cancer) under infrared irradiatation. The findings herein demonstrate that infrared-irradiated H-TiO_2-PEG NPs exhibit low toxicity, high efficiency as a photothermal agent for cancer therapy, and are promising for further biomedical applications.

(4) Si/N-doped TiO_2 core/shell nanopillar arrays with a nanoporous structure are fabricated through a simple protein-mediated TiO_2 deposition process, which can be considered as the advance reseach for prepration of H-TiO_2 on the sensitive templates with ultrafine nanostructure.

In the further research, it is expected that indepth understnding the microstructure and opening up the new application fields of H-TiO_2 is highly desirable for development of this materials.

Firstly, the concentration and distribution of oxygen vacanies and H doping in H-TiO_2 with different hydrogenation degrees should be characterized by electron paramagnetic resonance (EPR), nuclear magnetic resonance (NMR), and positron annihilation lifetime spectroscopy (PALS). More importantly, the coordination and valence state of Ti atom (Ti^{3+}, Ti-H, and Ti-OH) in the surface layer of H-TiO_2 will be analyzed through X-ray absorption (XAS). After theoretical calculations, the charge (lithium ions and electrons) transportation between oxygen vacanies-riched surface and crystallized bulk

of H-TiO_2 could be explained. These results might be useful and informative for both basic research and industrial production of H-TiO_2.

Secondly, several methods could be used to modify the microstructure of H-TiO_2 in order to extend its application fields and further improve its electrochemical and photocatalytic activity. (1) Controlled synthesis of H-TiO_2 with high concentration of bulk defects and surface Fe, Co, Ni, or Mn doping for oxygen reduction reaction (ORR). (2) Tuning the balance of the photo-oxidative and -reductive efficiency of H-TiO_2 for selective photocatalytic reactions (changing the type and concentration of defects on the surface through high pressure H_2/Ar annealing, Ar plasma etching, or nonmetal elements doping). (3) Fabrication of chemically bonded H-TiO_2/C hybrid nanostructures for lithium-ion battery and supercapacitor (formation of Ti^{3+}-C bonds during the photocatalytic reduction process). (4) Increasing the density of surface hydroxy (Ti-OH) toward pseudocapacitive effect for the fast lithium storage (H_2O_2/HCl treatment).

References

[1] M. Winter, J. O. Besenhard, M. E. Spahr, P. Novák, *Adv. Mater.* **1998**, *10*, 725.

[2] M. Ni, M. K. H. Leung, D. Y. C. Leung, K. Sumathy, *Renewable Sustainable Energy Rev.* **2007**, *11*, 401.

[3] M. Hu, J. Chen, Z.-Y. Li, L. Au, G. V. Hartland, X. Li, M. Marquez, Y. Xia, *Chem. Soc. Rev.* **2006**, *35*, 1084.

[4] P.-X. Gao, P. Shimpi, H. Gao, C. Liu, Y. Guo, W. Cai, K.-T. Liao, G. Wrobel, Z. Zhang, Z. Ren, H.-J. Lin, *Int. J. Mol. Sci.* **2012**, *13*, 7393.

[5] X. B. Chen and S. S. Mao, *Chem. Rev.,* **2007**, *107*, 2891.

[6] Z. Yang, D. Choi, S. Kerisit, K. M. Rosso, D. Wang, J. Zhang, G. Graff, J. Liu, *J. Power Sources* **2009**, *192*, 588.

[7] D. Deng, M. G. Kim, J. Y. Lee, J. Cho, *Energy Envir. Sci.* **2009**, *2*, 818.

[8] A. S. Arico, P. Bruce, B. Scrosati, J. M. Tarascon, W. van Schalkwijk, *Nat. Mater.* **2005**, *4*, 366.

[9] X. Chen, C. Burda, *J. Am. Chem. Soc.* **2008**, *130*, 5018.

[10] J. Hensel, G. M. Wang, Y. Li and J. Z. Zhang, *Nano Lett.*, **2010**, *10*, 478.

[11] F. Sauvage, F. Di Fonzo, A. Li Bassi, C. S. Casari, V. Russo, G. Divitini, C. Ducati, C. E. Bottani, P. Comte, M. Graetzel, *Nano Lett.* **2010**, *10*, 2562.

[12] A. Wang, H. Jing, *Dalton Trans.* **2014**, *43*, 1011.

[13] Z. Zheng, B. Huang, J. Lu, Z. Wang, X. Qin, X. Zhang, Y. Dai, M. H. Whangbo, *Chem. Commun.* **2012**, *48*, 5733.

[14] M. Kong, Y. Li, X. Chen, T. Tian, P. Fang, F. Zheng, X. Zhao, *J. Am. Chem. Soc.* **2011**, *133*, 16414.

[15] X. Han, Q. Kuang, M. Jin, Z. Xie, L. Zheng, *J. Am. Chem. Soc.* **2009**, *131*, 3152.

[16] X. Xin, X. F. Zhou, J. H. Wu, X. Y. Yao and Z. P. Liu, *ACS Nano*, **2012**, *6*, 11035.

[17] X. Chen, L. Liu, P. Y. Yu, S. S. Mao, *Science* **2011**, *331*, 746.

[18] X. Chen, L. Liu, Z. Liu, M. A. Marcus, W. C. Wang, N. A. Oyler, M. E. Grass, B. Mao, P. A. Glans, P. Y. Yu, J. Guo, S. S. Mao, *Sci. Rep.* **2013**, 3.

[19] J. Y. Shin, J. H. Joo, D. Samuelis, J. Maier, *Chem. Mater.* **2011**, *24*, 543.

[20] Z. Lu, C. T. Yip, L. Wang, H. Huang, L. Zhou, *ChemPlusChem* **2012**, *77*, 991.

[21] Y. H. Hu, *Angew. Chem. Int. Ed.* **2012**, *51*, 12410.

[22] T. Xia, W. Zhang, W. Li, N. A. Oyler, G. Liu, X. Chen, *Nano Energy* **2013**, *2*, 826.

[23] X. Lu, G. Wang, T. Zhai, M. Yu, J. Gan, Y. Tong, Y. Li, *Nano Lett.* **2012**, *12*, 1690.

[24] T. Xia, C. Zhang, N. A. Oyler, X. Chen, *Adv. Mater.* **2013**, *25*, 6905.

[25] Y. Liu, K. Ai, J. Liu, M. Deng, Y. He, L. Lu, *Adv. Mater.* **2013**, *25*, 1353.

[26] K.T. Thurn, H. Arora, T. Paunesku, A. Wu, E.M.B. Brown, C. Doty, J. Kremer, G. Woloschak, *Nanomedicine-Nanotechnol.* **2011**, *7*, 123.

[27] R. Ji, M. Hornung, M. A. Verschuuren, R. van de Laar, J. van Eekelen, U. Plachetka, M. Moeller, C. Moormann, *Microelectron. Eng.* **2010**, *87*, 963.

[28] D. Wang, R. Ji, S. Du, A. Albrecht, P. Schaaf, *Nanoscale Research Letters* **2013**, *8*, 42.

[29] D. Wang, S. Schönherr, R. Ji, A. Herz, C. Ronning, and P. Schaaf, *J. Micromech. Microeng.* **2013**, *23*, 074004.

[30] J. M. Tarascon, M. Armand, *Nature* **2001**, *414*, 359.

[31] F. F. Cao, X. L. Wu, S. Xin, Y. G. Guo, L. J. Wan, *J. Phys. Chem. C* **2010**, *114*, 10308.

[32] S. Yoon, B. H. Ka, C. Lee, M. Park, S. M. Oh, *Electrochem. Solid-State Lett.* **2009**, *12*, A28.

[33] G. Sudant, E. Baudrin, D. Larcher, J. M. Tarascon, *J. Mater.Chem.* **2005**, *15*, 1263.

[34] M. Wagemaker, W. J. H. Borghols, F. M. Mulder, *J. Am. Chem. Soc.* **2007**, *129*, 4323.

[35] W. Wang, M. Tian, A. Abdulagatov, S. M. George, Y. C. Lee, R. Yang, *Nano Lett.* **2012**, *12*, 655.

[36] K. S. Park, J. G. Kang, Y. J. Choi, S. Lee, D. W. Kim, J. G. Park, *Energy Environ. Sci.* **2011**, *4*, 1796.

[37] Y. G. Guo, Y. S. Hu, W. Sigle, J. Maier, *Adv. Mater.* **2007**, *19*, 2087.

[38] G. C. Li, Z. H. Zhang, H. R. Peng, K. Z. Chen, *RSC Advance* **2013**, *3*, 11507.

[39] S. T. Myung, M. Kikuchi, C. S. Yoon, H. Yashiro, S. J. Kim, B. Scrosati, *Energy Environ. Sci.* **2013**, *6*, 2609.

[40] A. L. Patterson, *Phys. Rev.* **1939**, *56*, 978.

[41] E. McCafferty, J. P. Wightman, *Surf. Interface Anal.* **1998**, *26*, 549.

[42] G. Iucci, M. Dettin, C. Battocchio, R. Gambaretto, C. Di Bello, G. Polzonetti, *Mater. Sci. Eng. C*, **2007**, *27*, 1201.

[43] A. Naldoni, M. Allieta, S. Santangelo, M. Marelli, F. Fabbri, S. Cappelli, C. L. Bianchi, R. Psaro, V. Dal Santo, *J. Am. Chem. Soc.* **2012**, *134*, 7600.

[44] J. Y. Shin, D. Samuelis, J. Maier, *Adv. Funct. Mater.* **2011**, *21*, 3464.

[45] C. Jiang, M. Wei, Z. Qi, T. Kudo, I. Honma, H. Zhou, *J. Power Sources* **2007**, *166*, 239.

[46] Y. G. Guo, Y. S. Hu, J. Maier, *Chem. Commun.* **2006**, 2783.

[47] K. Zhu, Q. Wang, J. H. Kim, A. A. Pesaran, A. J. Frank, *J. Phys. Chem. C* **2012**, *116*, 11895.

[48] H. Lindström, S. Södergren, A. Solbrand, H. Rensmo, J. Hjelm, A. Hagfeldt, S. E. Lindquist, *J. Phys. Chem. B* **1997**, *101*, 7717.

[49] Wang, J. Polleux, J. Lim, B. Dunn, *J. Phys. Chem. C* **2007**, *111*, 14925.

[50] B. Hao, Y. Yan, X. B. Wang, G. Chen, *Appl. Mater. Interfaces* **2013**, *5*, 6285.

[51] Y. Kuwahara, H. Yamashita, *J. Mater. Chem.* **2011**, *21*, 2407.

[52] S. C. Roy, O. K. Varghese, M. Paulose, C. A. Grimes, *ACS Nano* **2010**, *4*, 1259.

[53] A. Kudo, Y. Miseki, *Chem. Soc. Rev.* **2009**, *38*, 253.

[54] A. L. Linsebigler, G. Q. Lu, J. T. Yates, *Chem. Rev.* **1995**, *95,* 735.

[55] G. Tian, Y. Chen, W. Zhou, K. Pan, C. Tian, X. R. Huang, H. Fu, *CrystEngComm* **2011**, *13*, 2994.

[56] T. Xia, X. Chen, *J. Mater. Chem. A* **2013**, *1*, 2983.

[57] G. Wang, H. Wang, Y. Ling, Y. Tang, X. Yang, R. C. Fitzmorris, C. Wang, J. Z. Zhang, Y. Li, *Nano Lett.* **2011**, *11*, 3026.

[58] X. Jiang, Y. Zhang, J. Jiang, Y. Rong, Y. Wang, Y. Wu, C. Pan, *J. Phys. Chem. C* **2012**, *116*, 22619.

[59] Z. Wang, C. Yang, T. Lin, H. Yin, P. Chen, D. Wan, F. Xu, F. Huang, J. Lin, X. Xie, M. Jiang, *Adv. Funct. Mater.* **2013**, *23*, 5444.

[60] Z. Wang, C. Yang, T. Lin, H. Yin, P. Chen, D. Wan, F. Xu, F. Huang, J. Lin, X. Xie, M. Jiang, *Energy Environ. Sci.* **2013**, *6*, 3007.

[61] G. Zhu, T. Lin, X. Lu, W. Zhao, C. Yang, Z. Wang, H. Yin, Z. Liu, F. Huang, J. Lin, *J. Mater. Chem. A* **2013**, *1*, 9650.

[62] T. Lin, C. Yang, Z. Wang, H. Yin, X. Lu, F. Huang, J. Lin, X. Xie, M. Jiang, *Energy Environ. Sci.* **2014**, *7*, 967.

[63] Q. Kang, J. Cao, Y. Zhang, L. Liu, H. Xu, J. Ye, *J. Mater. Chem. A* **2013**, *1*, 5766.

[64] W. Wei, N. Yaru, L. Chunhua, X. Zhongzi, *RSC Adv.* **2012**, *2*, 8286.

[65] X. Pan, M. Q. Yang, X. Fu, N. Zhang, Y. J. Xu, *Nanoscale* **2013**, *5*, 3601.

[66] T. Leshuk, R. Parviz, P. Everett, H. Krishnakumar, R. A. Varin, F. Gu, *ACS Appl. Mater. Interfaces* **2013**, *5*, 1892.

[67] X. Yu, B. Kim, Y. K. Kim, *ACS Catal.* **2013**, *3*, 2479.

[68] G. Yang, Z. Jiang, H. Shi, T. Xiao, Z. Yan, *J. Mater. Chem.* **2010**, *20*, 5301.

[69] Y. Sun, Z. Sun, S. Gao, H. Cheng, Q. Liu, J. Piao, T. Yao, C. Wu, S. Hu, S. Wei, Y. Xie, *Nat. Commun.* **2012**, *3*, 1057.

[70] T. Xia, W. Zhang, J. B. Murowchick, G. Liu, X. Chen, *Adv. Energy Mater.* **2013**, *3*, 1516.

[71] T. Xia, W. Zhang, J. Murowchick, G. Liu, X. Chen, *Nano Lett.* **2013**, *13*, 5289.

[72] H. Liu, H. T. Ma, X. Z. Li, W. Z. Li, M. Wu, X. H. Bao, *Chemosphere* **2003**, *50*, 39.

[73] S. Hoang, S. P. Berglund, N. T. Hahn, A. J. Bard, C. B. Mullins, *J. Am. Chem. Soc.* **2012**, *134*, 3659.

[74] M. Chiesa, M. C. Paganini, S. Livraghi, E. Giamello, *Phys. Chem. Chem. Phys.* **2013**, *15*, 9435.

[75] L. B. Xiong, J. L. Li, B. Yang, Y. Yu, *J. Nanomater.* **2012**, *2012*, 13.

[76] S. J. DeCanio, J. B. Miller, J. B. Michel, C. Dybowski, *J. Phys. Chem.* 1**983**, *87*, 4619.

[77] N. Bityurin, L. Znaidi, A. Kanaev, *Chem. Phys. Lett.* **2003**, *374*, 95.

[78] N. O. Gopal, H. H. Lo, S. C. Sheu, S. C. Ke, *J. Am. Chem. Soc.* **2010**, *132*, 10982.

[79] W. Wang, C. Lu, Y. Ni, M. Su, Z. Xu, *Appl. Catal. B-Environ* **2012**, *127*, 28.

[80] M. Manzanares, C. Fàbrega, J. Oriol Ossó, L. F. Vega, T. Andreu, J. R. Morante, *Appl. Catal. B-Environ* **2014**, *150–151*, 57.

[81] M. Tahir, N. S. Amin, *Chem. Eng. J.* **2013**, *230*, 314.

[82] M. D'Arienzo, J. Carbajo, A. Bahamonde, M. Crippa, S. Polizzi, R. Scotti, L. Wahba, F. Morazzoni, *J. Am. Chem. Soc.* **2011**, *133*, 17652.

[83] N. M. Dimitrijevic, Z. V. Saponjic, B. M. Rabatic, O. G. Poluektov, T. Rajh, *J. Phys. Chem. C* **2007**, *111*, 14597.

[84] N. Serpone, D. Lawless, R. Khairutdinov, *J. Phys. Chem.* **1995**, *99*, 16646.

[85] F. J. Knorr, C. C. Mercado, J. L. McHale, *J. Phys. Chem. C* **2008**, *112*, 12786.

[86] M. V. Dozzi, C. D'Andrea, B. Ohtani, G. Valentini, E. Selli, *J. Phys. Chem. C* **2013**, *117*, 25586.

[87] C. Hamaguchi, Basic Semiconductor Physics, Springer, Heidelberg, Germany, **2009**.

[88] J. Liu, J. Li, A. Sedhain, J. Lin, H. Jiang, *J. Phys. Chem. C* **2008**, *112*, 17127.

[89] H. Shi, R. Magaye, V. Castranova, J. Zhao, *Particle and Fibre Toxicology* **2013**, *10*, 15.

[90] R. Cai, Y. Kubota, T. Shuin, H. Sakai, K. Hashimoto, A. Fujishima. *Cancer Res***. 1992**, *52*, 2346.

[91] M. Song, R. Zhang, Y. Dai, F. Gao, H. Chi, G. Lv, B. Chen, X. Wang, *Biomaterials* **2006**, *27*, 4230.

[92] J. Seo, H. Chung, M. Kim, J. Lee, I. Choi, J. Cheon, *Small* **2007**, *3*, 850.

[93] Q. Li, X. Wang, X. Lu, H. Tian, H. Jiang, G. Lv,; D. Guo, C. Wu, B. Chen, *Biomaterials* **2009**, *30*, 4708.

[94] E.A. Rozhkova, I. Ulasov, B. Lai, N.M. Dimitrijevic, M.S. Lesniak, T. Rajh, *Nano lett.* **2009**, *9*, 3337.

[95] T. Lopez, E. Ortiz, M. Alvarez, J. Navarrete, J. A. Odriozola, F. Martinez-Ortega, E. A. Páez-Mozo, P. Escobar, K. A. Espinoza, I. A. Rivero, *Nanomedicine-Nanotechnol.* **2010**, *6*, 777.

[96] K. T. Thurn, H. Arora, T. Paunesku, A. Wu, E. M. B. Brown, C. Doty, J. Kremer, G. Woloschak, *Nanomedicine-Nanotechnol.* **2011**, *7*, 123.

[97] I. Řehoř, V. Vilímová, P. Jendelová,; V. Kubíček, D. Jirák, V. Herynek, M. Kapcalová, J. Kotek, J. Černý, P. Hermann, *J. Med. Chem.* **2011**, *54*, 5185.

[98] Y. Yin, W. Zhu, L. Guo, R.Yang, X. Li, Y. Jiang, *J. Phys. Chem. B* **2013**, *117*, 125.

[99] L. Zeng, W. Ren, L. Xiang, J. Zheng, B. Chen, A. Wu,. *Nanoscale* **2013**, *5*, 2107.

[100] T. Paunesku, T. Rajh, G. Wiederrecht, J. Maser, S. Vogt, N. Stojićević, M. Protić, B. Lai, J. Oryhon, M. Thurnauer, *Nature Materials* **2003**, *2*, 343.

[101] G. Wang, Y. Ling Y. Li, *Nanoscale* **2012**, *4*, 6682.

[102] X. Ma, Y. Dai, L.Yu, B. Huang, *Sci. Rep.* **2014**, 4, 3986.

[103] Y. Yan, B. Hao, D. Wang, G. Chen, E. Markweg, *J. Mater. Chem. A,* **2013**, *1*, 14507.

[104] Y. Yan, M. Han, A. Konkin, T. Koppe, D. Wang, T. Andreu, G. Chen, U. Vetter, J. R. Morante, P. Schaaf, *J. Mater. Chem. A,* **2014**, *2*, 12708.

[105] Y. Huang, S. He, W. Cao, K. Cai, X. Liang, *Nanoscale* **2012**, *4*, 6135.

[106] E.C. Dreaden, A. M. Alkilany, X. Huang, C.J. Murphy, M. El-Sayed, *Chem. Soc. Rev.* **2012**, *41*, 2740.

[107] Y. Wang, K.C.L. Black, H. Luehmann, W. Li, Y. Zhang, X. Cai, D. Wan, S. Liu, M. Li, P. Kim, *ACS Nano* **2013**, *7*, 2068.

[108] J. He, X. Huang, Y. Li, Y. Liu, T. Babu, M.A. Aronova, S. Wang, Z. Lu, X. Chen, Z. Nie, *J. Am. Chem. Soc.* **2013**, *135*, 7974.

[109] S. Wang, K. Chen, T. Wu, H. Wang, W. Lin, M. Ohashi, P. Chiou, H.Tseng, *Angew. Chem. Int. Ed.* **2010**, *49*, 3777.

[110] Z. Jiang, B. Dong, B. Chen, J. Wang, L. Xu, S. Zhang, H. Song, *Small* **2013**, *9*, 604.

[111] X. Huang, S. Tang, X. Mu, Y. Dai, G. Chen, Z. Zhou,; F. Ruan, Z. Yang, N. Zheng, *Nat. Nanotechnol.* **2011**, *6*, 28.

[112] K. Yang, L. Feng, X. Shi, Z. Liu, *Chem. Soc. Rev.* **2013**, *42*, 530.

[113] X. Wang, C. Wang, L. Cheng, S. T. Lee, Z. Liu, *J. Am. Chem. Soc.* **2012**, *134*, 7414.

[114] K. Dong, Z. Liu, Z. Li, J. Ren, X. Qu, *Adv. Mater.* **2013**, *25*, 4452.

[115] Z. Chen, Q. Wang, H. Wang, L. Zhang, G. Song, L. Song, J. Hu, H. Wang, J. Liu, M. Zhu, *Adv. Mater.* **2013**, **25**, 2095.

[116] S. S.Chou, B. Kaehr, J. Kim, B. M. Foley, M. De, P. E. Hopkins, J. Huang, J. Brinker, V. P. Dravid, *Angew. Chem. Int. Ed.* **2013**, *52*, 4160.

[117] C. M. Hessel, V. P. Pattani, M. Rasch, M. G. Panthani, B. Koo, J. W. Tunnell, B. A. Korgel, *Nano Lett.* **2011**, *11*, 2560.

[118] J. Zhou, Z. Lu, X. Zhu, X. Wang, Y. Liao, Z. Ma, F. Li, *Biomaterials* **2013**, *34*, 9584.

[119] M. Chen, X. Fang, S. Tang, N. Zheng, *Chem. Commun.* **2012**, *48*, 8934.

[120] R. Asahi, T. Morikawa, T. Ohwaki, K. Aoki, Y. Taga, *Science* **2001**, *293*, 269.

[121] Y. L. Lee, C. F. Chi, S. Y. Liau, *Chem. Mater.* **2010**, *22*, 922.

[122] Y. J. Hwang, A. Boukai, P. D. Yang, *Nano Lett.,* **2009,** *9*, 410.

[123] Y. W. Chen, J. D. Prange, S. Dühnen, Y. Park, M. Gunji, C. E. Chidsey, P. C. McIntyre, *Nat. Mater.* **2011**, *10*, 539.

[124] J. L. Sumerel, W. Yang, D. Kisailus, J. C. Weaver, J. H. Choi, D. E. Morse, *Chem. Mater.* **2003**, *15*, 4804.

[125] G. P. Smith, K. J. Baustian, C. J. Ackerson, D. L. Feldheim, *J. Mater. Chem.* **2009**, *19*, 8299.

[126] S. L. Sewell, D. W. Wright, *Chem. Mater.* **2006**, *18*, 3108.

[127] Y. J. Jiang, D. Yang, L. Zhang, Q. Y. Sun, X. H. Sun, J. Li, Z. Y. Jiang, *Adv. Funct. Mater.* **2009**, *19*, 150.

[128] Y. N. Fang, Q. Z. Wu, M. B. Dickerson, Y. Cai, S. Shian, J. D. Berrigan, N. Poulsen, N. Kroger, K. H. Sandhage, *Chem. Mater.* **2009**, *21*, 5704.

[129] J. D. Berrigan, T. S. Kang, Y. Cai, J. R. Deneault, M. F. Durstock, K. H. Sandhage, *Adv. Funct. Mater.* **2011**, *21*, 1693.

[130] N. R. Haase, S. Shian, K. H. Sandhage, N. Kroger, *Adv. Funct. Mater.* **2011**, *21*, 4243.

[131] Lee, W. J.; Lee, J. M.; Kochuveedu, S. T.; Han, T. H.; Jeong, H. Y.; Park, M.; Yun, J. M.; Kwon, J.; No, K.; Kim, D. H.; Kim, S. O. *ACS Nano* **2012**, *6*, 935.

[132] M. B. Dickerson, C. L. Knight, M. K. Gupta, H.R. Luckarift, L. F. Drummy, M. L. Jespersen, G. R. Johnson, R.R. Naik, *Mater. Sci. Eng. C* **2011**, *31*, 1748.

[133] T. Nonoyama, T. Kinoshita, M. Higuchi, K. Nagata, M. Tanaka, K. Sato, K. Kato, *J. Am. Chem. Soc.* **2012**, *134*, 8841.

[134] B. Hao, Y. Yan, X. B. Wang, G. Chen, *ACS Appl. Mater. Interfaces* **2013**, *5*, 6285.

[135] X. B. Wang, Y. Yan, B. Hao, G. Chen, *ACS Appl. Mater. Interfaces* **2013**, *5*, 3631.

[136] J. Wang, W. Zhu, Y. Zhang and S. Liu, *J. Phys. Chem. C*, **2007**, *111*, 1010.

[137] G. Yang, Z. Jiang, H. Shi, T. Xiao, Z. Yan, *J. Mater. Chem.*, **2010**, *20*, 5301.

Own Publications

[1] Y. Yan, B. Hao, D. Wang, G. Chen, E. Markweg, A. Albrecht P. Schaaf, Understanding the fast lithium storage performance of hydrogenated TiO_2 nanoparticles, *J. Mater. Chem. A,* **2013**, *1*, 14507.

[2] Y. Yan, D. Wang, P. Schaaf, Fabrication of N-doped TiO_2 coatings on nanoporous Si nanopillar arrays through biomimetic layer by layer mineralization, *Dalton Trans.* **2014**, *43*, 8480.

[3] Y. Yan, M. Han, A. Konkin, T. Koppe, D. Wang, T. Andreu, G. Chen, U. Vetter, J. R. Morante, P. Schaaf, Slightly hydrogenated TiO_2 with enhanced photocatalytic performance, *J. Mater. Chem. A,* **2014**, *2*, 12708. (Front Cover)

[4] B. Hao, Y. Yan, X. B. Wang, G. Chen, Synthesis of anatase TiO_2 nanosheets with enhanced pseudocapacitive contribution for fast lithium storage, *ACS Appl. Mater. Interfaces* **2013**, *5*, 6285.

[5] X. B. Wang, Y. Yan, B. Hao, G. Chen, Protein-mediated layer-by-layer synthesis of TiO_2(B)/anatase/carbon coating on nickel foam as negative electrode material for lithium-ion battery *ACS Appl. Mater. Interfaces* **2013**, *5*, 3631.

[6] B. Hao, Y. Yan, X. B. Wang, G. Chen, Biomimetic layer-by-layer co-mineralization approach towards TiO_2/Au nanosheets with high rate performance for lithium ion batteries, *Nanoscale*, **2013**, *5*, 10472.

[7] X. B. Wang, Y. Yan, B. Hao, G. Chen, Biomimetic layer-by-layer deposition assisted synthesis of Cu, N co-doped TiO_2 nanosheets with enhanced visible light photocatalytic performance, *Dalton Trans.* **2014**, *43*, 14054.

[8] D. Wang, Y. Yan, P. Schaaf, T. Sharp, S. Schönherr, C. Ronning, R. Ji, ZnO/porous-Si and TiO_2/porous-Si nanocomposite nanopillars. *Journal of Vacuum Science & Technology A*, **2015**, *33*, 01A102.

[9] Y. Yan, D. Wang, and P. Schaaf, Fabrication of N-doped TiO_2 on mesoporous Si nanopillar arrays through biomimetic layer by layer mineralization for water splitting. Poster at *EMRS 2013 Spring Meeting*, Strasbourg, France.

[10] Y. Yan, D. Wang, and P. Schaaf, Controlled synthesis of N-doped TiO_2 by biomimetic mineralization pathway for green energy devices. Talk at *EUROMAT 2013*, Sevilla, Spain

[11] Y. Yan, D. Wang, and P. Schaaf, Facile synthesis of N-doped TiO_2/Si nanopillar arrays through biomimetic layer by layer mineralization. Poster at *1st International Conference & 3rd International MacroNano-Colloquium 2014*, Ilmenau, Germany.

[12] Y. Yan, D. Wang, and P. Schaaf, Plasma-assisted synthesis of hydrogenated TiO_2 for energy storage and conversion. Talk at *DPG 2015 Spring Meeting*, Berlin, Germany.

[13] Y. Yan, D. Wang, and P. Schaaf, Hydrogenated black TiO_2 for the fast lithium storage. Talk at *1st International Conference on Applied Surface Science (ICASS) 2015*, Shanghai, China.

[14] W. Ren,[#] Y. Yan,[#] L. Zeng, Z. Shi, A. Gong, P. Schaaf, D. Wang, J. Zhao, B. Zou, G. Chen, A. Wu, A near infrared light triggered hydrogenated black TiO_2 for cancer photothermal therapy, **2014**, submitted.(Co-first author)